Inference of transport phenomena in quantum devices

David L. Craig

Merton College

University of Oxford

A thesis submitted for the degree of

Doctor of Philosophy

Michaelmas 2023

Acknowledgements

This thesis is a product of the ideas and guidance of many people with whom I have been fortunate to work with and learn from. My foremost thanks to my supervisors Natalia Ares, Erik Gauger, and Andrew Briggs who have encouraged me throughout my research. Many thanks to Natalia for providing both excellent laboratory facilities and a cohesive team of people in Oxford, while also guiding my research for experimental applications. I would like to extend particular gratitude to Erik, who joined my supervision team late in my first year of study when theoretical aspects of my research became more significant. He has since been exceptionally generous with his time from afar at Heriot-Watt University, and been an incredible host on several visits to his group. I would also like to thank Andrew for his continued enthusiasm for my work and for stretching my perception of what research entails.

The work in this thesis has been supported not only by my supervisors, but by the people that I have had the pleasure of working with over the last four years. Hyungil Moon has been a source of inspiration in several aspects of my research with a particular impact on machine learning. Hyungil contributed significantly to the work presented in Chapter 5, and imparted knowledge that allowed me to elevate the standard of my work. Dino Sejdinovic and Dominic Lennon also provided useful discussions on work presented in Chapter 5, with Dominic also providing insight on the contents of Chapter 4. The experiments performed in Chapter 3 were inspired by fascinating discussions with collaborators Florian Meier, Paul Erker, and Marcus Huber at the Vienna University of Technology, along with Mark Mitchison at Trinity College Dublin.

One cannot manage a cryogenics laboratory alone and, under Natalia's direction, the entire group has helped develop and maintain lab facilities. Particular thanks to Florian Vigneau, Federico Fedele, Barnaby van Straaten, and Joseph Hickie for contributions to the lab which have directly facilitated experimental results presented in this thesis. Collaborators at the University of Basel, Dominik Zumbühl and Leon Camenzind, and at the Institute of Science and Technology Austria, Georgios Katsaros and Daniel Jirovec, have generously provided devices which have been used in this thesis.

The entire group in Oxford, past and present members included, have always provided a friendly working environment, interesting discussion (scientific

or otherwise), and many lunches around Oxford. Beyond those mentioned above, Yikai Yang, Vincent Michal, Anna Pearson, Brandon Severin, Sebastian Orbell, Kushagra Aggarwal, Jonas Schuff, Marek Rychetsky, Jonathan Dexter, and Pranav Vaidhyanathan have all helped make group activities enjoyable and enlightening.

I shall not forget my time and experiences at Merton College, during which I have made a great deal of friends, some of whom will hopefully remain so long after we leave Oxford. A mention to the entire team: Cesca, Antonia, Silvia, Lucas, Charlie, Lachlan, Tom, James, and Mathias. I have been part of many amazing extracurricular communities in Oxford, namely the Merton MCR, Merton and Mansfield RFC, Oxford University RFC, and Oxford University Touch Rugby Club. I have also had the good fortune to live with excellent people during my time in Oxford, with a particular mention to Jack, Wilf, Henry, Connie, and Charlotte.

Lastly, I would like to thank my family and friends in Northern Ireland who have supported me throughout my journey, perhaps more than they anticipated due to global forces outside of our control. James and Philip have always been available to catch up when I visit home, and Fergus has kindly made time in Edinburgh on my research visits. My grandparents have always taken a keen interest in my studies from an early age, and their encouragement has been invaluable. Lastly, I would like to thank my parents and siblings, who have always been supportive of my pursuits. None of this would have been possible without them.

Abstract

This thesis is concerned with charge transport in electrostatically defined quantum dot devices. Such devices display a wide range of transport phenomena in both open and closed configurations. The transport regime can be tuned experimentally by controlling the voltages applied to gate electrodes, but the precise electrostatic landscape which determines the transport regime is unknown. This uncertainty is given by variations in device fabrication, material defects, and sources of electrostatic disorder.

The research chapters of this thesis consider a range of transport regimes in quantum dot devices, and infer properties of the device using both experimental and theoretical techniques. The first research chapter considers the detection of single charge transport events through a double quantum dot. By fitting an open quantum systems model to the sub-attoampere currents measured, tunnel rates are inferred. The second results chapter considers an electrostatic simulation of a quantum dot device and how it can be accelerated using deep learning. This accelerated model is then used in the third results chapter, along with experimental measurements of the transport regime, to inform a Bayesian inference algorithm and produce a set of disorder potentials to narrow the gap between simulation and reality. The final results chapter develops a differentiable quantum master equation solver which is used for parameter estimation in a theoretical study of transport in single and double quantum dots.

Publications

The results presented in Chapter 3 are part on an ongoing collaboration, with future publications planned.

The results presented in Chapter 5, and parts of the results presented in Chapter 4, feature in the following publication:

D.L. Craig†, H. Moon†, F. Fedele, D.T. Lennon, B. van Straaten, F. Vigneau, L.C. Camenzind, D.M. Zumbühl, G.A.D. Briggs, M.A. Osborne, D. Seijdinovic, and N. Ares. *'Bridging the Reality Gap in Quantum Devices with Physics-Aware Machine Learning'.* Physical Review X 14 (1), 011001 (2024)

Author contributions: DLC developed the physical and machine learning models, performed the experiments, performed the data analysis, and wrote the manuscript with input from NA. HM developed reparameterisation and inference algorithms. FF, BVS, FV, contributed to experimental setup and assisted with measurements. DMZ and LCC fabricated the device. DS provided input on machine learning approaches. DLC, DTL, FF, BVS, FV, and NA labelled data. All authors commented on the manuscript. The study was conceived by HM and NA with input from DLC.

The results presented Chapter 6 feature in the manuscript:

D.L. Craig, N. Ares, and E.M. Gauger. *'Differentiable master equation solver for quantum device characterisation'.* arXiv preprint, arXiv:2403.04678 (2024)

Author contributions: DLC developed the model, performed the calculations, and wrote the manuscript with input from NA and EMG. The study was conceived by DLC with guidance from NA and EMG.

During my doctoral training, I have contributed to other publications which do not feature in this thesis:

D. Jirovec, P.M. Mutter, A. Hofmann, A. Crippa, M. Rychetsky, D.L. Craig, J. Kukucka, F. Martins, A. Bllabio N. Ares, D. Chrastina, G. Isella, G. Burkard, and G. Katsaros. *'Dynamics of Hole Singlet-Triplet Qubits with Large g-Factor Differences'.* Physical Review Letters 128, 126803 (2022)

V. Gebhart, R. Santagati, A.A. Gentile, E.M. Gauger, D.L. Craig, N. Ares, L. Banchi, F. Marquardt, L. Pezzè, and C. Bonato. *'Learning Quantum Systems'.* Nature Reviews Physics 5, 141–156 (2023)

J. Schuff, D.T. Lennon, S. Geyer, D.L. Craig, F. Fedele, F. Vigneau, L.C. Camenzind, A.V. Kuhlmann, G.A.D. Briggs, D.M. Zumbühl, D. Seijdinovic, and N. Ares. *'Identifying Pauli spin blockade using deep learning'.* Quantum 7, 1077 (2023)

J. Schuff, M.J. Carballido, M. Kotzagiannidis, J.C. Calvo, M. Caselli, J. Rawling, D.L. Craig, B. van Straaten, B. Severin, F. Fedele, S. Svab, P. Chevalier Kwon, R.S. Eggli, T. Patlatiuk, N. Korda, D.M. Zumbühl, and N. Ares. *'Fully autonomous tuning of a spin qubit'.* arXiv preprint arXiv:2402.03931 (2024)

† - joint first authorship.

Author Contributions

I wrote the text in this thesis and all following instances of 'the author' refer to myself. Unless otherwise stated, I obtained all experimental data, performed all simulations, and created all figures presented in this thesis. The boxes below indicate my contributions to each chapter, and each box appears at the beginning of the relevant chapter. I wrote the conclusion and appendices, but detailed contributions are not included due to their nature of being supplementary to the technical results of this thesis.

Chapter 1

> The author reviewed the literature to curate a discussion of the themes relevant to this thesis. All presented experimental data was obtained by the author using an existing setup.

Chapter 2

> This chapter presents standard derivations pertaining to the theory of open quantum systems, along with existing models of quantum dots. The author adapted and expanded on material from various sources to develop a narrative relevant to this thesis. All presented simulations were performed by the author.

Chapter 3

> All measurements presented in this chapter where carried out by the author using an existing experimental setup. The author performed all analysis of the experimental data, including the fitting of theoretical models.

Chapter 4

The electrostatic model of the device presented in this chapter was developed by the author using methods from the literature. The author worked jointly with Hyungil Moon to determine the transport path and number of quantum dots. The author performed all aspects of deep learning acceleration, including designing model architectures, generating training data, and training models.

Chapter 5

The author worked jointly with Hyungil Moon to develop the inference algorithm presented in this chapter. Hyungil Moon developed the reparameterisation of the disorder potential. The author obtained the experimental data, with some assistance from Barnaby van Straaten and Federico Fedele. The author implemented all instances of the inference algorithm, and performed analysis of the resulting data.

Chapter 6

The differentiable master equation solver presented in this chapter was developed solely by the author. Application of the solver to each of the discussed models, including the parameter optimisation and data analysis, was performed by the author.

Acronyms and Abbreviations

1D, 2D, 3D . . One-, two-, or three-dimensional

2DEG . . . . . Two-dimensional electron gas

2DHG . . . . . Two-dimensional hole gas

ANN . . . . . Artificial neural network

CNN . . . . . Convolutional neural network

CPU . . . . . Central processing unit

DAC . . . . . Digital to analogue converter

DC . . . . . Direct current

FPR . . . . . False positive rate

GP . . . . . Gaussian process

GPU . . . . . Graphics processing unit

HMC . . . . . Hamiltonian Monte Carlo

ODE . . . . . Ordinary differential equation

MAE . . . . . Mean absolute error

MAP . . . . . Maximum a posteriori

MAPE . . . . Mean absolute percentage error

MCMC . . . . Markov chain Monte Carlo

MLE . . . . . Maximum likelihood estimation

MST . . . . . Minimum spanning tree

RNN . . . . . Recurrent neural network

ROC . . . . . Receiver operating characteristic

TPR . . . . . True positive rate

Contents

1 Introduction

The author reviewed the literature to curate a discussion of the themes relevant to this thesis. All presented experimental data was obtained by the author using an existing setup.

1.1 Motivation and Outline

Transport of charge in semiconductors is key to digital technology. The first semiconductor transistor was developed in 1947 [1], and just a decade later a semiconductor integrated circuit was demonstrated [2]. Rapid miniaturisation of this technology to current 3 nm processes has led to modern computers and advanced semiconductor fabrication technology. Reaching such small length scales means that fabrication limitations and atomic diameters are becoming problematic for controlling transport in semiconductor transistor technology [3].

It has more recently become possible to probe quantum effects when measuring transport through nanoscale devices. In fact, semiconductor devices have been proposed as a candidate for scalable quantum computing by controlling spins of charges confined in quantum dots [4], and have seen remarkable development in the last two decades with recent demonstrations of universal control in six qubits [5] and fidelities above the fault-tolerant threshold [6]. While spin is typically the quantity

which defines qubits in such devices, controlling the transport of single charges is required to accurately determine the qubit state. Quantum dot devices feature as the experimental platform in this thesis, specifically considering electrostatically defined quantum dots due to their flexible tuning.

The tunable nature of electrostatically defined quantum dots allows a wide range of physical phenomena to be investigated in the same device. Probing transport effects to investigate electron-phonon interactions [7, 8], thermodynamics [9], and Kondo physics [10–12] have also found a platform with such devices. There are several types of quantum dots which differ in fabrication and operation to those discussed in this thesis; the closest relations being molecular junctions in which charge transport is often probed [13, 14] and self-assembled quantum dots which are optically active [15]. As considered in this thesis, the transfer of charge from one quantum dot to another can be enhanced by interactions with an external environment (e.g. vibrational modes). Notable examples of such environment-assisted transport processes outside the field of quantum dots include energy transport in biophysical systems [16], trapped ions [17], and superconducting qubits [18].

This thesis combines experimental measurements, theoretical models, and inference methods to better understand characteristics of quantum dot devices with a focus on transport phenomena. The primary motivation is to integrate theoretical models in functional algorithms to enhance our capability to probe features of quantum devices, where standard approaches may be limited in scope or practicality. Examples of such features considered in this thesis include the statistics of single-charge tunnelling events through a double quantum dot, and examining the disorder landscape of a device for which there is no direct experimental probe.

The remainder of this chapter outlines details of electrostatically defined quantum dot devices, followed by a brief review of relevant machine learning methods with emphasis on their applications to quantum devices. Chapter 2 discusses the details of modelling open quantum systems using quantum master equations which are used in various parts of this thesis to explain transport phenomena. In Chapter 3 a double quantum dot is tuned to the slow tunnel rate regime such that single-charge

tunnel events can be resolved, with the goal of investigating the interaction of charges with phonons. Counting these tunnel events facilitates an estimate of current through the double quantum dot, and a quantum master equation is used to characterise the system. We then turn to a more broad characterisation of quantum devices using a deep learning accelerated electrostatic model which is presented in Chapter 4. This model is used in Chapter 5, where transport measurements inform a physics-aware inference algorithm to determine characteristics of hidden electrostatic disorder potentials. Chapter 6 presents a differentiable quantum master equation solver with applications to understanding transport in single and double quantum dot devices using optimisation and Bayesian techniques in a theoretical setting. This thesis concludes with a brief discussion of the impact of the results presented and possible future research directions in Chapter 7.

1.2 Electrostatically Defined Quantum Dots

A quantum dot is a potential well which confines charge in three dimensions, and is often referred to as an artificial atom. Electrostatically defined quantum dots are the focus of this thesis, whereby quantum dots are formed in semiconductors by applying voltages to metallic gates to manipulate the band structure such that charge carriers are suitably confined. Due to the localisation of charge on a quantum dot there is a large charging energy $E_C = e^2/2C_\Sigma$ associated with adding another charge to the dot, where e is the electronic charge and C_Σ is the total capacitance of the dot. This results in discrete charge transitions as the confinement potential of the dot is varied and the number of charges on the dot changes. The length scale of the confinement potential also results in orbital excited states which typically have a smaller energy separation than the charging energy. Treating the quantum dot as a particle in a box gives $E_{\text{orb}} \approx \hbar^2/m^* a^2$ where $\hbar$ is the reduced Planck's constant, m_* is the effective mass of a charge, and a is the dot radius [19].

The transport regime of a device is critical to the formation of quantum dots. Measuring current across the device provides information about whether the transport channel is open or closed, as well as signatures of quantum dot formation

in the closed channel regime. The signature of quantum dot formation is the observation of transitions associated with adding or removing a single charge from the dot, and can be observed by measuring current through the dot. A schematic of the electrostatic potential energy induced by voltages on gate electrodes and the resulting transport regimes is shown in Figure 1.1. We show a 1D transport channel for the purpose of visualisation; the same principles apply to quantum dots formed in a 2D plane with a schematic of such a device shown in Figure 1.5(a).

Charge transport across a quantum dot relies on tunnel coupling to source and drain leads and, when operated at low temperature ($k_{\mathrm{B}}T \ll E_C$, where k_{B} is the Boltzmann constant) and small bias voltage ($eV_{\mathrm{bias}} < E_C$), charges tunnel sequentially across the dot when the energy associated with adding another charge (the electrochemical potential of the dot) lies within the bias window[1]. This results in periodic peaks in current when the confinement potential is varied to change the number of charges on the dot. When the dot electrochemical potential is outside the bias window, the quantum dot is said to be in Coulomb blockade and no charge transport may occur. A schematic of this behaviour is shown in Figure 1.2(a).

When considering a double quantum dot (i.e. two quantum dots in series with a tunnel coupling between them), transport from source to drain is also conditioned on the alignment of the electrochemical potentials of each dot. Transport occurring when both of the dot electrochemical potentials are aligned and between the bias window is known as resonant, or elastic, transport. When the dot electrochemical potentials are not aligned, inelastic processes (e.g. interaction with a phonon bath) must be present to facilitate off-resonant transport. There also exists a capacitive coupling between the dots, whereby the presence of a charge on one dot impacts the electrochemical potential of the neighbouring dot [20]. Without this capacitive coupling, the double quantum dot charge transitions as a function of two gate voltages would simply be a cross-hatch of two intersecting sets of parallel lines (equivalent to independent single quantum dots). The inter-dot capacitive coupling

[1] In the sequential tunnelling regime, the current I through a quantum dot and its characteristic tunnel rate Γ are related via number of charges transferred per unit time such that I [A] $\sim 10^{-19}$ Γ [Hz]. Some useful conversions for this thesis: 1 aA $\sim$ 10 Hz, 1 pA $\sim$ 10 MHz.

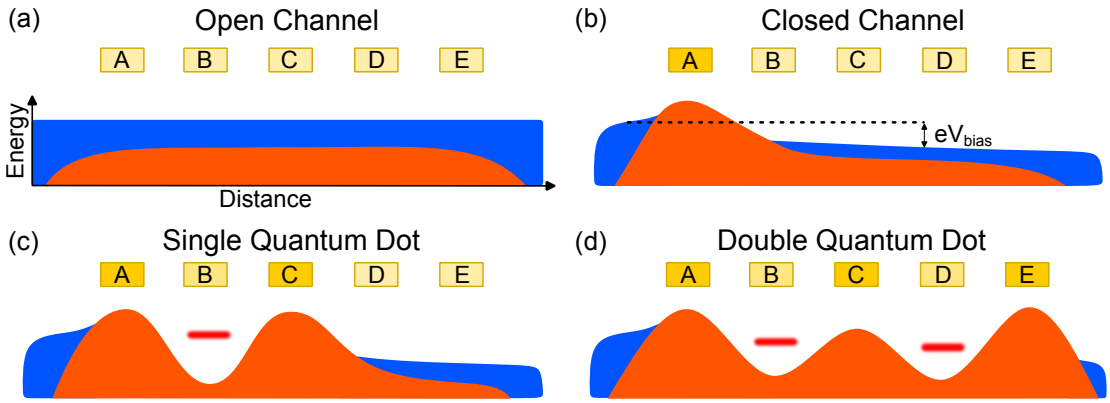

Figure 1.1: Different transport regimes of a transport channel. Continuous charge density in indicated in blue, electrostatic potential energy is indicated in orange, and discrete quantum dot electrochemical potentials are indicated in red. Gate electrodes A-E are shown above the transport channel with the colour saturation indicating the strength of the gate voltage. The open channel regime (a) means current freely flows from source to drain across the device, while the closed channel regime (b) means current is suppressed by a potential barrier. The closed channel regime can be reached by increasing the voltage on one of the gates, which in our case is gate A. In the closed channel regime, single (c) and double (d) quantum dots can be formed by manipulating the gate voltages to control the confinement potential.

introduces an additional charge transition between a charge being on one dot or the other which results in a region of constant charge being a hexagon, where three charge states become degenerate at each vertex which is known as a triple point. At finite bias voltage the triple points expand into triangular regions known as bias triangles which, with suitable tunnel rates, can be observed in current measurements. The base of the triangle is the line along which resonant transport occurs. A schematic of a double quantum dot charge stability diagram with a positive applied bias is shown in Figure 1.2(b).

1.3 Constant Interaction Model

The charge stability schematics shown in Figure 1.2 can be quantified using the constant interaction model, which is a popular method of describing a system of quantum dots using classical physics [20]. As the name suggests, it is an electrostatic model which assumes a constant capacitance between between elements of a network where dots act as metallic conductors. The schematics of a single and double

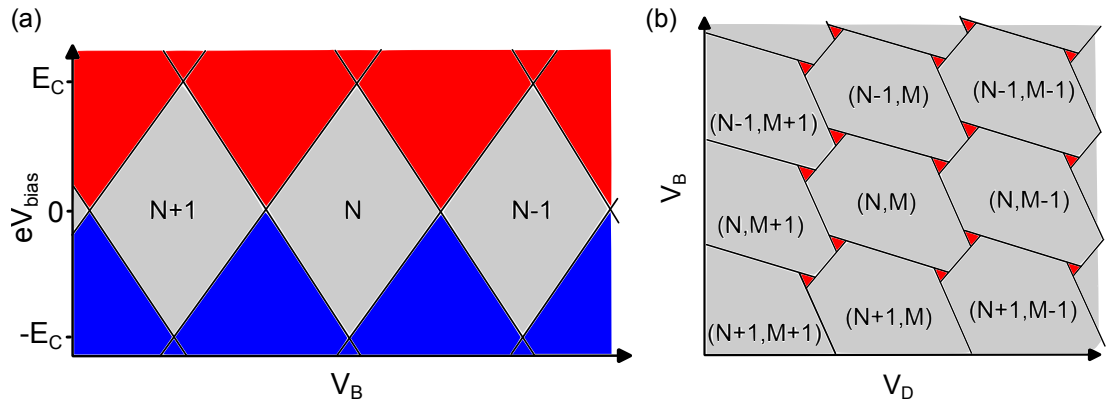

Figure 1.2: Schematics of the charge transitions in (a) a single quantum dot and (b) a double quantum dot. Gate voltage labels follow the convention displayed in Figure 1.1. Regions of grey indicate Coulomb blockade, red indicates positive current, and blue indicates negative current. In each case, as the magnitude of the gate voltage increases, the number of charges on the dot decreases. The schematic does not consider the effects of orbital energies associated with spin filling rules. The double dot schematic in (b) indicates a positive bias with the presence of bias triangles. For a negative bias the triangles would have negative current and point in the opposite diagonal direction, and at zero bias there would be no triangles and three transition lines meet at a single vertex known as a triple point.

quantum dot capacitance model are shown in Figure 1.3. For a system of N conductors, a capacitance can be defined between each pair of conductors with a capacitor storing charge q_{ij} with capacitance c_{ij} between conductor i and conductor j, each of which stores a charge. The total charge on each conductor is then

$$Q_j = \sum_{k=0}^{N} q_{jk} = \sum_{k=0}^{N} c_{jk}(V_j - V_k), \tag{1.1}$$

where V_j is the potential on the j^{th} conductor. We set the ground potential to $V_0 = 0$. This can be more compactly represented as a matrix operation, $\mathbf{Q} = C\mathbf{V}$, where C is the capacitance matrix of the system. The total electrostatic energy of the system can then be calculated as,

$$U = \frac{1}{2}\mathbf{V}^T C\mathbf{V} = \frac{1}{2}\mathbf{Q}^T\mathbf{V} = \frac{1}{2}\mathbf{Q}^T C^{-1}\mathbf{Q}. \tag{1.2}$$

The voltage from gate electrodes can be included in the capacitance model by assuming a large capacitance to ground with a large charge stored such that $V = \frac{Q}{C}$. To simplify the problem of inverting the capacitance matrix with such

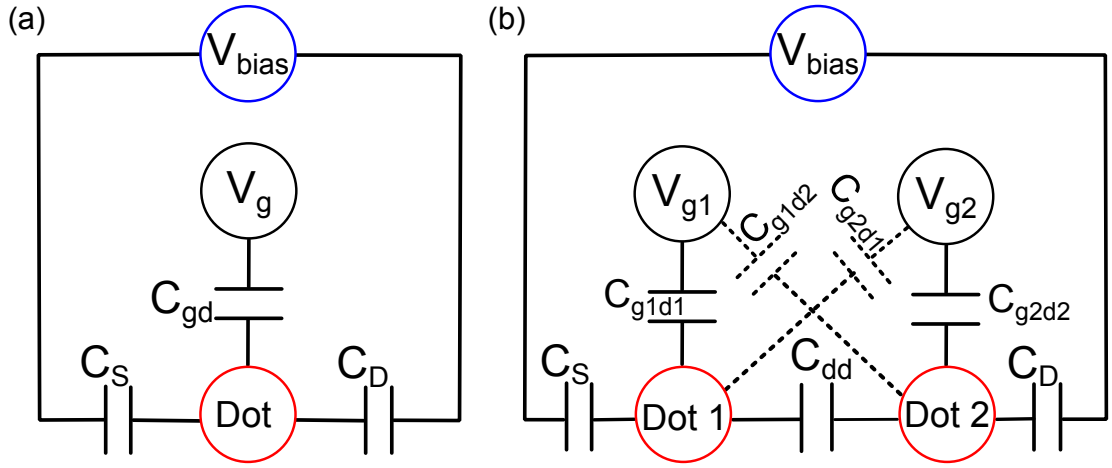

Figure 1.3: Circuit schematics of a capacitive model of (a) a single quantum dot and (b) a double quantum dot. Each dot system is considered as a network of conductors with capacitive coupling between elements. The mechanism of cross-talk can be seen in (b) where the gate above each dot has a capacitive coupling to the other dot.

large elements, we can split it into blocks

$$\begin{pmatrix} \mathbf{Q}_d \\ \mathbf{Q}_g \end{pmatrix} = \begin{pmatrix} C_{dd} & C_{dg} \\ C_{gd} & C_{gg} \end{pmatrix} \begin{pmatrix} \mathbf{V}_d \\ \mathbf{V}_g \end{pmatrix}, \tag{1.3}$$

where subscript d represents dots and subscript g represents gate electrodes. The potentials on the dots are then

$$\mathbf{V}_d = C_{dd}^{-1}(\mathbf{Q}_d - C_{dg}\mathbf{V}_g), \tag{1.4}$$

which allows the electrostatic energy to be calculated as $U = \frac{1}{2}\mathbf{V}^T C\mathbf{V}$ without requiring inversion of the entire capacitance matrix. The equilibrium charge state of a system of quantum dots is the vector of integer values $\mathbf{Q}_d = e\mathbf{N}$ which minimises U for a given $\mathbf{V}_g$. When these equilibrium integer charge values change as a function of gate voltages, a charge transition line will be observed in a measurement which detects quantum dot occupation. For the example of a double quantum dot, these transitions are the lines enclosing each hexagon as shown in Figure 1.2(b).

Defining $\boldsymbol{\delta}_j$ to be a unit vector with a single non-zero element at position j the electrochemical potential of a dot is $\mu_j(\mathbf{N}) = U(\mathbf{N}) - U(\mathbf{N} - \boldsymbol{\delta}_j)$. In the limit of infinitesimal bias, elastic transport is allowed between a source and drain reservoir when $\mu_i = 0$, $\forall\ i \in [1, \ldots, N]$. Different charge transport processes

occur depending on the conditions of the electrochemical potential. The voltages at which all $\mu_i(\mathbf{N}) = 0$ results in charge transport and the voltages at which $\mu_i(\mathbf{N} + \boldsymbol{\delta}_j) = 0$ results in anti-charge[2] transport in the opposite direction such that the observed current has the same directionality. Under an applied bias, the condition for elastic transport is relaxed to require all electrochemical potentials to be resonant and within the bias window, i.e. $\mu_i = \mu \ \forall \ i \in [1, \ldots, N]$ and $eV_{\text{drain}} < \mu < eV_{\text{source}}$. Inelastic transport occurs when this condition is relaxed further to only require the electrochemical potentials to be within the bias window, without the condition of resonance. Considering the example of a double quantum dot as shown in Figure 1.2(b), these regions of transport can be seen under an applied bias at the intersection of each set of three transition lines where both dot electrochemical potentials are within the bias window. The bias triangle at the intersection of the charge states (N, M), $(N + 1, M)$, and $(N, M + 1)$ hosts charge transport, and the bias triangle at the intersection of $(N+1, M)$, $(N, M+1)$, and $(N + 1, M + 1)$ hosts anti-charge transport.

1.4 Materials for Electrostatically Defined Quantum Dot Devices

Electrostatically defined quantum dots can be created in a range of semiconductors, most notably GaAs, SiGe, Si, Ge, and InAs. This thesis presents experimental data from laterally defined quantum dots in AlGaAs/GaAs and Ge/SiGe heterostructure devices with a schematic of each shown in Figure 1.4. A driving force for the development of electrostatically defined quantum dot devices is their potential to be a platform for scalable quantum computing, whereby the spins of electrons (or holes) confined in dots encode qubits [4, 21, 22]. We do not focus on spin qubits, but a brief discussion of material development motivated by their operation is fundamental context for the devices used in this thesis. The material platform of a particular electrostatically defined quantum dot device defines several properties of the system;

[2]For an electron-based device, a charge refers to an electron and an anti-charge refers to a hole, and vice-versa for a hole-based device.

such as the type of charge (electrons, holes, or both), whether the charges are depleted or accumulated by applied gate voltages, the presence or absence of a nuclear spin bath, the characteristics of electrostatic disorder and charge noise, the phonon coupling mechanism, and spin-orbit interaction.

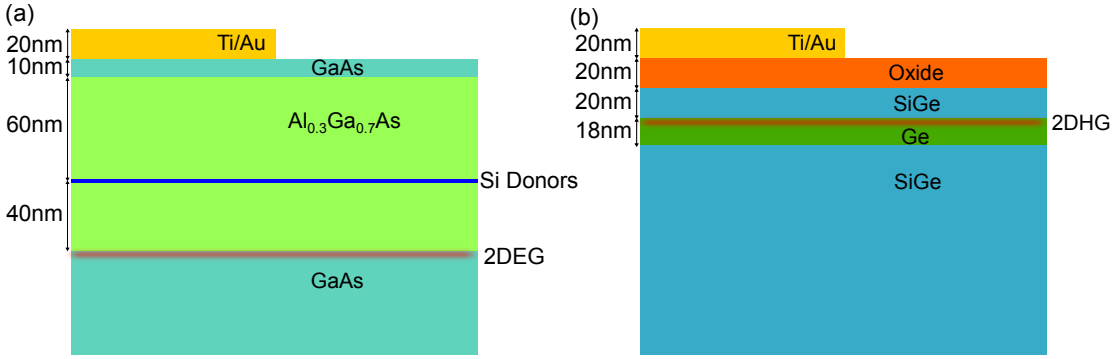

Figure 1.4: Heterostructure schematic of the devices used for experimental results in this thesis. Nominal position of a Ti/Au surface gate is shown on both. (a) A GaAs based device which hosts a 2DEG approximately 110nm beneath the surface gates and is operated in depletion mode by applying negative voltages. (b) A Ge/SiGe based device which hosts a 2DHG approximately 40nm beneath the surface gates and is operated in depletion mode by applying positive voltages.

Laterally defined quantum dot devices, where the dots are defined in a horizontal plane, were first established in AlGaAs/GaAs [23]. Fabrication of electrostatically defined quantum dots in GaAs involves molecular beam epitaxy to create a heterostructure of GaAs and AlGaAs, and doping the AlGaAs with Si introduces free electrons which form a two-dimensional electron gas (2DEG) at the interface which is typically 50-100 nm below the surface [24]. Patterned gates are introduced at the sample surface by electron-beam lithography and metal evaporation, negative voltages can then applied to these gates to produce an electrostatic field in the 2DEG (or 2DHG) to confine charge in quantum dots.

As previously discussed, electrostatically defined quantum dots are a platform for spin qubits such as the Loss-DiVincenzo [4, 25] or the singlet-triplet qubit [21]. A readout mechanism for spin qubits is spin-to-charge conversion. The first demonstration of spin-to-charge readout was in 2004 for a single quantum dot coupled to a reservoir where the Fermi level lies between the Zeeman splitting of the spin up and spin down states on the dot [26]. Under an applied magnetic field, the

spin state determines whether the charge can tunnel from the dot to the reservoir. This mechanism is known as Elzerman readout. When dealing with spin states in double quantum dots, Pauli spin blockade is an important phenomena; depending on the spin state, current either flows through the double dot or it is blocked. This blockade provides a direct method for readout of the qubit state and it was first demonstrated in laterally defined quantum dots in 2005 [27, 28]. The energies of singlet and triplet states of a two-spin system in the presence of a magnetic field are integral to this readout as well as for qubit initialisation and control.

Since spin states are sensitive to magnetic fields, the non-zero nuclear spin of GaAs poses a problem for constructing qubits with long coherence times. Each electron spin is coupled to a bath of randomly oriented nuclear spins through the hyperfine interaction which causes decoherence. Since the electrons exist in different orbital wavefunctions, and can be spatially separated during qubit operation, they each experience a different magnetic field. The effect of this random magnetic field was first investigated in lateral quantum dots by Koppens et al. where they observe leakage current due to singlet-triplet mixing [25]. The non-zero nuclear spin of GaAs provided motivation to move to silicon devices which have a dominant isotope with zero nuclear spin. Removing the spin-$\frac{1}{2}$ nuclei of Si^{29} to produce isotopically enriched silicon allows for spin coherence times exceeding seconds as shown in Ref. [29]. The existing silicon industry could also accelerate fabrication of large scale devices [30, 31]. A quantum well is created in SiGe devices by using a SiGe-Si-SiGe sandwich [32], and Si devices use the metal-oxide-semiconductor (MOS) interface of Si and SiO_2 [33, 34]. Spin qubits based on donor impurities in silicon have also developed material design [22, 35, 36].

A recent development in electrostatic quantum dot material design has been to use a germanium well [37]; a layer of Ge sandwiched between layers of SiGe [38, 39], a Ge-Si core-shell nanowire [40–42], or a Ge nanowire grown on Si [43, 44]. As a Group-IV element, germanium retains the advantage of having a dominant isotope with zero nuclear spin, and the low effective mass of holes allows for less stringent fabrication requirements as larger dots can be operated as qubits. The p-orbital

nature of holes results in weak hyperfine interaction with nuclear spins, and induces strong spin-orbit interaction which allows for fast manipulation of spins [37].

Outside of the heterostructure designs discussed above, electrostatic quantum dots have been formed in InAs nanowires [45], carbon nanotubes [46–48], and graphene [49–51]. This highlights the breadth of utility in studying quantum dots in nanoscience.

1.5 Measuring and Tuning Quantum Dots

In order to tune the gate voltages of a quantum dot device into the quantum dot regime, there must be a means of measuring the state of the device. The most direct way of measuring a device is to apply a bias across source and drain Ohmic contacts and measure the current flowing between them. We focus on the discussion of depletion mode devices which are used in this thesis. In the case of a depletion mode device, when the gate electrode voltages are set to zero there will be a 2DEG (or 2DHG) present in the heterostructure which allows current to flow freely. Once sufficiently high gate voltages have been applied to necessary gates electrodes, an electrostatic potential barrier will form between source and drain, such as in Figure 1.1(b), and current will quickly decrease to zero. At this stage of tuning, the device behaves as a transistor as shown in Figure 1.5(b).

When a quantum dot is tuned, there will be periodic signals in current known as Coulomb peaks when sweeping gate voltages controlling the confinement potential of the dot [52]. These peaks arise as a result of a classical effect known as Coulomb blockade where a large energy required to add an extra charge to the dot due to electrostatic repulsion (known as the charging energy, E_C) [53, 54]. When the chemical potential of the dot is in the bias window between source and drain chemical potentials, charges may pass through the dot from source to drain and current flows. Once the chemical potential of the dot leaves the bias window the dot has a fixed charge occupation and is said to be in Coulomb blockade where no current may flow. The charge occupation of a dot changes by one when moving across a Coulomb peak from one region of Coulomb blockade to another as shown

in Figure 1.2(a). Evidence of a quantum dot can be seen in the periodic signals at the corner of open channel current in Figure 1.5(c). This quantum dot would be considered coarsely tuned as the charge transitions are not particularly well defined, and do not extend far in voltage space beyond the region of open channel transport.

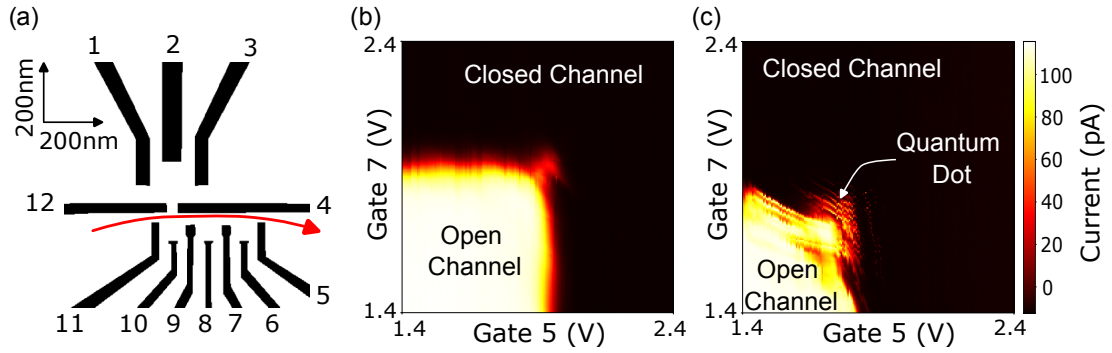

Figure 1.5: Example data from a Ge/SiGe device with heterostructure as shown in Figure 1.4(b). (a) A schematic of the gate electrode design, with gates labelled 1-12 and the direction of current considered in panels (b) and (c) is indicated by a red arrow. The upper portion of the device can be operated as a separate transport channel. (b) A scan over two gate voltages with regions of open and closed channel labelled. (c) The same scan as in (b) but with a plunger gate voltage (Gate 6) increased between the two barrier gates being swept. Periodic signals in current are evidence that a quantum dot has formed (further tuning would be required for optimal operation). The boundary between open and closed channel moves to lower voltages in (c) when compared to (b), this is an example of cross-talk from the increased plunger voltage affecting the behaviour of the device with respect to other voltages. (b) and (c) share the colour bar.

For double quantum dots, a similar consideration is made for the electrochemical potential of each dot. With well defined barriers, current may only flow through a double dot in series when the electrochemical potential of each dot is within the bias window, with an example shown in Figure 1.6(b). As previously discussed, this leads to the formation of bias triangles in current measurements [20] with current prohibited by Coulomb blockade when the electrochemical potential of either dot is outside the bias window. With more open barriers (i.e. faster tunnel rates), current can flow when only one dot electrochemical potential is within the bias window, a phenomenon known as co-tunnelling.

When tuning a device to the single electron (or hole) regime for qubit operation, many devices need to be depleted to the extent that tunnel barriers prevent measurable current. This is a consequence of gate design not facilitating small

dots with sufficiently fast tunnel barriers. The charge state of the quantum dots under investigation (referred to as the device dots) can be sensed by capacitive coupling to another quantum dot (referred to as the sensor dot) with its own source and drain electrodes. A schematic of a device with a sensor dot used in this thesis is shown in Figure 1.6(a). The sensor dot is tuned such that it is at the point of maximum gradient on a Coulomb peak, where the current through the sensor dot is most sensitive to changes in electrostatic potential. As the sensor dot is capacitively coupled to the device dots, a change in charge occupation on the device dots will shift the electrochemical potential of the sensor dot, thus changing the current through it. Detecting the change in current of a sensor dot induced by a change in charge state of a device dot is known as charge sensing, with an example shown in Figure 1.6(c). The sensor dot can detect charge transitions which are not visible in transport measurements due to the tunnel rates becoming too slow at higher gate voltage. Figure 1.6(c) also shows that the charge sensing contrast is not uniform. This is a result of cross-capacitance between the measurement gate voltages and the electrochemical potential of the sensor dot, but this effect has recently been automatically compensated to maintain contrast between charge states across a large range of gate voltages [55]. A similar mode of charge sensing is to use a quantum point contact (QPC) instead of a sensor dot [56], but these typically have lower sensitivity to device dot transitions when compared to sensor dots and are no longer widely used.

Another popular means of charge sensing is to use a radio-frequency reflectometry setup [57], though we do not use such a setup in this thesis. In such measurements, a radio-frequency signal is sent to either a gate electrode or an Ohmic contact in the device and the reflected signal depends on the impedance and capacitance of the device. The reflected signal is amplified and demodulated into quadrature components to extract information about the device. Measuring using radio-frequency reflectometry is much faster than current measurements as a much lower integration time can be used. The impedance matching conditions necessary for a good reflected signal limits the measurement bandwidth, but even with this

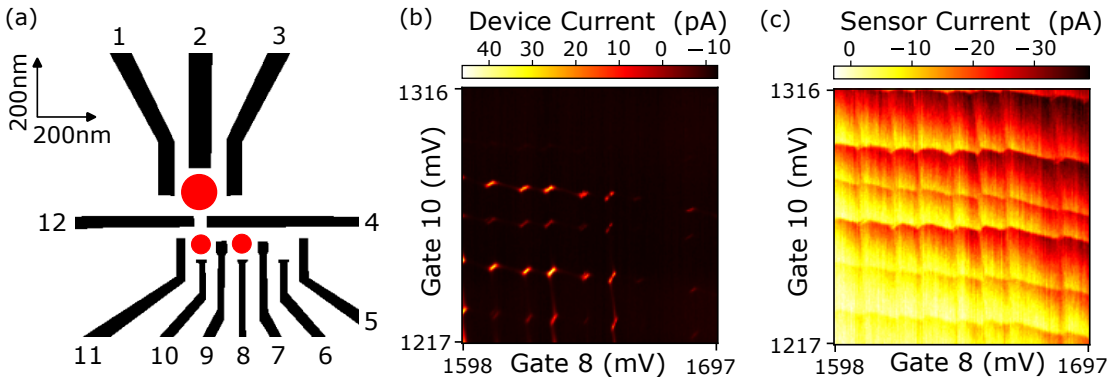

Figure 1.6: Example data from a Ge/SiGe device with gate electrode design detailed in (a) and heterostructure as shown in Figure 1.4(b). Gate electrodes are labelled in (a) and nominal locations of quantum dots are indicated in red, with the topmost dot being operated as a sensor dot. (b) Transport data through a double quantum dot device as the plunger of each dot is swept. Current flows when both quantum dot electrochemical potentials are within the bias window. (c) Sensor dot current measured simultaneously with the data in (b). A honeycomb of transition lines is clearly visible throughout the entire scan. Device current is pinched off by slow tunnel barriers at high plunger voltages, but the sensor dot can still detect charge transitions.

limitation it has recently been demonstrated that it is possible to tune double dots using only reflectometry measurements [58].

Details of the tuning process for quantum dots varies depending on the device design and often requires device specific knowledge from an experimentalist. Such a hands-on approach typically does not scale well beyond a double quantum dot, and recent efforts have focused on automating the tuning of quantum dot devices [58–65]. One of the primary challenges to scalable tuning is the cross-capacitance (or cross-talk) between gates. This cross-talk refers to the action of changing one gate electrode having an influence on a region of the device that is primarily controlled by another gate. This stems from the electrostatic potential induced by the gate electrode not being well localised. Virtual gates can be created by measuring the cross-talk of each gate and creating a linear combination of gates to act on one area of the device (e.g. a dot electrochemical potential, or a barrier between dots) [66]. The advantage of using virtual gates has been demonstrated in tuning and controlling linear arrays of quantum dots [67–69].

1.6 Machine Learning

In the last decade there has been an ever increasing influence of machine learning on science, technology, and academic research more broadly. Large parts of this thesis combine experiment, theory, and machine learning to better understand quantum dot devices and it is therefore necessary to discuss the background of the methods used, along with some relevant applications to quantum devices.

1.6.1 Deep Learning

Artificial neural networks (ANNs) are possibly the most widely known facet of machine learning, in which parameterised models inspired by neuroscience are trained to produce a desired output for a given input. Modern applications of ANNs typically fall into the category of deep learning models, so named because their structure typically has many layers of abstraction between the input and output. There are several types of deep learning model, each with a different inductive bias (i.e. a different way of connecting the information). The simplest of these is the multi-layer perceptron (MLP) which propagates an input vector through connected layers of nodes, each node producing a non-linear function of its input, and produces an output vector. Of relevance to this thesis, MLPs have been applied to predict transport features of a multi-terminal silicon device [70].

While MLPs are widely used as machine learning models in their own right, they often form components of other, more complex architectures. One of the most popular is the convolutional neural network (CNN) for image recognition. They function by passing convolutional filters over an image to extract properties and an MLP is attached at the end to produce an output. When considering quantum dots, 2D current maps or stability diagrams are a suitable experimental domain for CNN application [59, 71, 72].

Deep recurrent neural networks (RNNs) have been successful in learning from time dependent data. RNNs function by allowing the output to influence the state of the network for the next input. While we are not aware of any experimental

application to quantum dot spin qubits, RNNs have been used to learn the dynamics of a superconducting qubit [73].

Reinforcement learning allows an agent to explore an environment according to a policy and every action the agent takes returns a reward with the goal of maximising the reward function. Traditional reinforcement learning struggles to deal with complex environments but deep reinforcement learning circumvents this issue by making decisions using neural networks. Reinforcement learning has been applied to the identification of bias triangles in a double quantum dot charge stability diagram [74].

Deep learning requires large, structured, and labeled data sets which is not possible in all situations, particularly when dealing with experimental physics. The number of parameters in deep learning models is often in the millions which means that the model is incredibly complex, and a consequence of this is that it is easy to fool a trained model via adversarial attacks whereby inputs are specifically designed with imperceptible noise to produce erroneous outputs [75–77].

1.6.2 Bayesian Statistics

In the regime where a large quantity of data is not available, Bayesian methods become much more powerful than deep learning. Bayesian methods rely more heavily on traditional statistics than the black-box nature of deep neural networks with many thousands of parameters, and are often more interpretable as a result. The key feature of a Bayesian algorithm is the use of Bayes' rule

$$P(A|B) = \frac{P(B|A)P(A)}{P(B)}, \tag{1.5}$$

which states that the posterior probability of an event A given event B, $P(A|B)$, is the prior probability of A, $P(A)$, multiplied by the likelihood of B given A, $P(B|A)$, and normalised by the evidence, $P(B)$. In most practical settings the evidence is intractable and methods such as Markov-chain Monte Carlo (MCMC) [78] or variational inference [79] are often used to approximate the posterior probability distribution. In a setting where the parameters $\boldsymbol{\theta}$ of a model are

being estimated with respect to some data y, the (unnormalised) Bayes' rule would read $P(\boldsymbol{\theta}|y) \propto P(y|\boldsymbol{\theta})P(\boldsymbol{\theta})$.

Bayesian statistics allows for prior knowledge to be incorporated into a probabilistic model, and repeated experiments mean that the posterior of one experiment can be used as the prior in the next to progressively narrow the probability distribution about some variable of interest. Adaptive methods following this approach have been used in spin qubits in GaAs [80], NV centres [81–83] and impurities in silicon [84].

1.6.3 Gaussian Processes

Training a deep learning model, or simply fitting a function to some data are parametric approaches to machine learning. A Gaussian Process (GP) is a non-parametric model which generates functions as a random sample from a multivariate Gaussian distribution and is completely described by functions for the mean and covariance of this distribution. The mathematical statement of generating a function $f(x)$ from a GP is

$$f(x) \sim \mathrm{GP}(m(x), K(x, x')), \tag{1.6}$$

where $m(x)$ and $K(x, x')$ are the mean and covariance functions of the GP. The hyperparameters defining the mean and covariance functions can be determined by simple inspection of the type of functions being targeted, or more rigorously inferred from data by optimising the maximum a posteriori (MAP) estimate using a prior over hyperparameter values.

A popular application of Gaussian processes is in Bayesian optimisation algorithms, where a function is optimised by performing sequential evaluations at the most informative parameter values [85, 86]. In these algorithms, a GP is used to efficiently sample the target function using previous evaluations as a condition on the multivariate Gaussian distribution. The GP samples provides an estimate of the mean and uncertainty in the target function in the full parameter space, facilitating a decision on the next set of parameters at which the target function is evaluated. This type of efficient sampling using a GP has been applied to the tuning

of electrostatic quantum dots to optimise score functions for charge sensing readout [55], and build models of the surface which separates the region of quantum dot features (e.g. Coulomb peaks or bias triangles) and the region of zero signal [58, 61].

1.7 Discussion

We have introduced the concepts of electrostatically defined quantum dots necessary to understand the results of this thesis. This thesis integrates theory, experiment, and machine learning in different ways to infer transport characteristics of electrostatically defined quantum dots. We shall primarily consider measurements or simulations of a double quantum dot system, however the transport regime of a device is more broadly discussed in Chapters 4 and 5, and simulation of a single quantum dot with an orbital excited state features in Chapter 6. Machine learning methods also feature throughout this thesis, with Chapter 3 employing simple model fitting, Chapter 4 developing deep learning accelerated simulations, Chapter 5 reparameterising an electrostatic disorder potential with a 2D Gaussian process and performing Bayesian inference, and Chapter 6 considering optimisation and Bayesian inference using a differentiable model.

2

Open Quantum Systems

This chapter presents standard derivations pertaining to the theory of open quantum systems, along with existing models of quantum dots. The author adapted and expanded on material from various sources to develop a narrative relevant to this thesis. All presented simulations were performed by the author.

In the context of quantum dots, many phenomena are explained by the system (quantum dots) interacting with an external environment (such as fermionic leads, or a bosonic bath). In these circumstances, it is necessary to adopt an open quantum systems approach to model the system dynamics. To do so, we must introduce the concept of a density matrix and the equations which govern their evolution. While this thesis is primarily concerned with the transport of charge through quantum dots, it is important to note that system-environment interactions are vital to understanding qubit dynamics, such as quantum dot spin qubits discussed in the previous chapter [4, 87].

There are various levels of detail in which open quantum system dynamics can be modelled [88–91], but in this chapter we consider Born-Markov master equations in the weak-coupling regime as they provide sufficient detail for the systems under consideration. We will outline the derivation of a general weak-coupling master equation, and consider a single quantum dot coupled to two fermionic leads (left

and right) as an instructive and relevant example. We then consider the details of a double quantum dot system interacting with a phonon bath present in the semiconductor crystal in which the dots are defined.

2.1 Density Operator

A closed quantum system is completely described by a state vector $|\psi\rangle$ that evolves in time according to the Schrödinger equation

$$i\hbar\frac{d}{dt}|\psi(t)\rangle = \hat{H}|\psi(t)\rangle, \tag{2.1}$$

where $\hat{H}$ is the Hamiltonian of the system under consideration. The solution of this equation is unitary evolution, and for time-independent $\hat{H}$, $|\psi(t)\rangle = e^{-i\hat{H}t/\hbar}|\psi(0)\rangle$.

In contrast, an open quantum system interacts with an environment and only the total system-environment wavefunction can be treated as a closed system evolving according to the Schrödinger equation. Open quantum systems modelling allows the dynamics of the system to be investigated with the system-environment interaction accounted for, while neglecting the computationally expensive evolution of the (generally very many) environment degrees of freedom. By discarding information about the complete state of the environment, (classical) uncertainties are introduced to the state of the system. This means that a state vector approach is insufficient to describe the system and we must introduce the density operator, $\hat{\rho}$, which represents an ensemble of pure states that the system may be in. This ensemble is

$$\hat{\rho} = \sum_i p_i|\psi_i\rangle\langle\psi_i|, \tag{2.2}$$

where p_i represents the probability that the system occupies the quantum state $|\psi_i\rangle$. The set of states $\{|\psi_i\rangle\}$ can be any orthonormal basis spanning the Hilbert space of the system, $\mathcal{H}_\mathcal{S}$. The density operator must be positive, Hermitian, and have unit trace. The diagonal elements of the density operator are the occupation of the basis states from which the unit trace condition arises, and if $\hat{\rho}$ represents a pure state (i.e. $p_i = \delta_{ij}$) then $\mathrm{tr}(\hat{\rho}^2) = 1$.

The expectation of an operator on a state represented by a density operator is,

$$\langle \hat{A} \rangle = \sum_i p_i \langle \psi_i | \hat{A} | \psi_i \rangle = \mathrm{tr}(\hat{A}\hat{\rho}). \tag{2.3}$$

If a density operator represents the state of a closed quantum system, the Schrödinger equation in Eq. (2.1) becomes the Liouville-von Neumann equation

$$i\hbar \frac{d\hat{\rho}(t)}{dt} = [H_S, \hat{\rho}(t)], \tag{2.4}$$

which has a unitary evolution solution $\hat{\rho}(t) = \hat{U}\hat{\rho}(0)\hat{U}^\dagger$ where $\hat{U} = e^{-i\hat{H}t/\hbar}$ for time-independent $\hat{H}$. For brevity of notation, we henceforth use natural units such that $\hbar = 1$.

2.2 Quantum Master Equations

In this section we derive a second order quantum master equation following standard derivations found in texts such as Refs. [88, 92]. We consider a system and environment described by the total Hamiltonian

$$\hat{H} = \hat{H}_S + \hat{H}_I + \hat{H}_E, \tag{2.5}$$

where $\hat{H}_S$ and $\hat{H}_E$ are the Hamiltonians of the isolated system and environment respectively, and $\hat{H}_I$ describes the system-environment interactions. Assuming the system and environment Hamiltonians have no explicit time dependence, we transform into the interaction representation. An operator in the Schrödinger representation, $\hat{O}$, is transformed to the interaction representation, $\tilde{O}$, by applying the unitary transformation, $U(t) = e^{-i(\hat{H}_S + \hat{H}_E)t}$. This transformation allows us to consider the dynamics of the system and environment density operator, $\tilde{\sigma}(t)$ using the Liouville-von Neumann equation

$$\frac{d\tilde{\sigma}(t)}{dt} = -i[\tilde{H}_I(t), \tilde{\sigma}(t)], \tag{2.6}$$

with the general solution, $\tilde{\sigma}(t) = \tilde{\sigma}(0) - i\int_0^t d\tau [\tilde{H}_I(\tau), \tilde{\sigma}(\tau)]$ which can be substituted back into Eq. (2.6) to give,

$$\frac{d\tilde{\sigma}(t)}{dt} = -i[H_I, \tilde{\sigma}(0)] - \int_0^t d\tau [\tilde{H}_I(t)[\tilde{H}_I(\tau), \tilde{\sigma}(\tau)]]. \tag{2.7}$$

We then trace out the environment degrees of freedom as the goal is to describe the dynamics of the system density operator $\tilde{\rho}(t) = \mathrm{tr}_E(\tilde{\sigma}(t))$. The evolution of the system then follows

$$\frac{d\tilde{\rho}(t)}{dt} = -\int_0^t d\tau \ \mathrm{tr}_E\Big([\tilde{H}_I(t)[\tilde{H}_I(\tau), \tilde{\sigma}(\tau)]]\Big), \tag{2.8}$$

where we set $[H_I, \tilde{\rho}(0)] = 0$ (which is always possible by choosing a suitable partition of the total Hamiltonian $\hat{H}$ [88]). This solution is still exact and remains as difficult to solve as the original Liouville-von Neumann equation. We now make a series of approximations to make the problem more tractable.

The first assumption, also known as the Born approximation, is that for weak system-environment coupling and an initially separable state $\tilde{\sigma}(0) \approx \tilde{\rho}(0) \otimes \tilde{\rho}_E(0)$, the total density operator remains approximately separable at all times such that $\tilde{\sigma}(t) \approx \tilde{\rho}(t) \otimes \tilde{\rho}_E(0)$, where $\tilde{\rho}_E(0)$ is the initial environment density operator. This remains true in the Schrödinger representation as the transformation is unitary. We can then write

$$\frac{d\tilde{\rho}(t)}{dt} = -\int_0^t d\tau \ \mathrm{tr}_E\Big([\tilde{H}_I(t)[\tilde{H}_I(\tau), \tilde{\rho}(\tau) \otimes \tilde{\rho}_E(0)]]\Big). \tag{2.9}$$

The above equation is simpler than Eq. (2.8) but remains non-local in time as the time evolution of the density matrix depends on its history. We move to a time local solution by making the Markov approximation which states the evolution of the system only depends on its current state, and replace $\tilde{\rho}(\tau)$ with $\tilde{\rho}(t)$. This assumption is again valid for weak system-environment coupling and with environment correlations which decay much faster than the system evolution timescale (the environment has no memory of previous system states). Following this approximation, we change variables from $\tau \to t-\tau$ and extend the integral in time to infinity to arrive at the general form of the time-local Born-Markov master equation,

$$\frac{d\tilde{\rho}(t)}{dt} = -\int_0^\infty d\tau \ \mathrm{tr}_E\Big([\tilde{H}_I(t)[\tilde{H}_I(t-\tau), \tilde{\rho}(t) \otimes \tilde{\rho}_E(0)]]\Big). \tag{2.10}$$

We now consider the system-environment interaction Hamiltonian, which can in general be expressed in terms of operators $\hat{A}_\alpha$ acting solely on the system and $\hat{B}_\alpha$

acting on the environment in the Schrödinger representation as,

$$\hat{H}_I = \sum_\alpha \hat{A}_\alpha \otimes \hat{B}_\alpha. \tag{2.11}$$

Transforming to the energy eigenbasis of the system Hamiltonian allows the interaction operators to be expressed in terms of the environment-mediated system energy changes, ω, that they induce

$$\hat{A}_\alpha(\omega) = \sum_{\epsilon-\epsilon'=\omega} \hat{\Pi}(\epsilon)\hat{A}_\alpha\hat{\Pi}(\epsilon'), \tag{2.12}$$

where the operator $\hat{\Pi}(\epsilon) = |\epsilon\rangle\langle\epsilon|$ is the projection operator onto the system eigenstate with energy ϵ. These operators have the following form in the interaction representation,

$$\tilde{A}_\alpha(\omega) = e^{i\hat{H}_s t}\hat{A}_\alpha(\omega)e^{-i\hat{H}_s t} = e^{-i\omega t}\hat{A}_\alpha(\omega), \tag{2.13}$$

$$\tilde{A}^\dagger_\alpha(\omega) = e^{i\hat{H}_s t}\hat{A}^\dagger_\alpha(\omega)e^{-i\hat{H}_s t} = e^{+i\omega t}\hat{A}_\alpha(\omega). \tag{2.14}$$

The full system interaction operator is recovered by summing over all possible energy changes, $\hat{A}_\alpha = \sum_\omega \hat{A}_\alpha(\omega)$, which gives rise to the following form of the interaction Hamiltonian for the Schrödinger representation,

$$\hat{H}_I = \sum_{\alpha,\omega} \hat{A}_\alpha(\omega) \otimes \hat{B}_\alpha. \tag{2.15}$$

This in turn leads to a convenient form of the interaction Hamiltonian in the interaction representation,

$$\tilde{H}_I(t) = \sum_{\alpha,\omega} e^{-i\omega t}\hat{A}_\alpha(\omega) \otimes \tilde{B}_\alpha(t). \tag{2.16}$$

where $\tilde{B}_\alpha(t) = e^{i\hat{H}_E t}\hat{B}e^{-i\hat{H}_E t}$. Inserting this equation back into the Born-Markov master equation in Eq. (2.10) gives

$$\begin{aligned}\frac{d\tilde{\rho}(t)}{dt} &= \int_0^\infty d\tau\ \mathrm{tr}_E\Big(\tilde{H}_I(t)\tilde{\rho}(t)\otimes\tilde{\rho}_E\tilde{H}_I(t-\tau) - \tilde{H}_I(t)\tilde{H}_I(t-\tau)\tilde{\rho}(t)\otimes\tilde{\rho}_E\Big) + \text{H.c.} \\ &= \sum_{\omega,\omega'}\sum_{\alpha,\beta} e^{i(\omega-\omega')t}\Gamma_{\alpha\beta}(\omega)\Big(\hat{A}_\alpha(\omega)\tilde{\rho}(t)\hat{A}^\dagger_\beta(\omega') - \hat{A}^\dagger_\beta(\omega')\hat{A}_\alpha(\omega)\tilde{\rho}(t)\Big) + \text{H.c.},\end{aligned} \tag{2.17}$$

where H.c. denotes the Hermitian conjugate. We have also introduced the terms,

$$\Gamma_{\alpha\beta}(\omega) = \int_0^\infty d\tau e^{i\omega\tau} \mathrm{tr}_E\Big(\tilde{B}_\alpha^\dagger(t)\tilde{B}_\beta(t-\tau)\rho_E\Big) = \int_0^\infty d\tau e^{i\omega\tau}\langle \tilde{B}_\alpha^\dagger(t)\tilde{B}_\beta(t-\tau)\rangle, \quad (2.18)$$

which absorb the dependence on ρ_E and $t-\tau$ and in the limit of the environment being in a stationary state, we have time independent correlation functions

$$\Gamma_{\alpha\beta}(\omega) = \int_0^\infty d\tau e^{i\omega\tau}\langle \tilde{B}_\alpha^\dagger(\tau)\tilde{B}_\beta(0)\rangle. \quad (2.19)$$

A further simplification can be made to Eq. (2.17) using the secular approximation which neglects terms where $\omega \neq \omega'$ and acts as a rotating wave approximation (RWA) by assuming that fast oscillating terms will average out and not influence system dynamics. This is the case when the system dynamics occur on a timescale that is much shorter than the environment-induced transitions, i.e. $\tau_S \ll \tau_E$. The relevant system dynamics are characterised by the inverse frequency differences, $\tau_S = |\omega - \omega'|^{-1}$, so this approximation is valid for large environment-induced changes in system energy. We then arrive at the following Markovian master equation in the Schrödinger representation,

$$\frac{d\rho(t)}{dt} = -i[H_I, \rho(t)] + \sum_\omega \sum_{\alpha,\beta} \Gamma_{\alpha\beta}(\omega)\Big(\hat{A}_\alpha(\omega)\rho(t)\hat{A}_\beta^\dagger(\omega) - \hat{A}_\beta^\dagger(\omega)\hat{A}_\alpha(\omega)\rho(t)\Big) + \text{H.c.}. \quad (2.20)$$

This equation can be cast into a more insightful form by decomposing the Fourier transforms of bath correlation functions into real and imaginary parts as

$$\Gamma_{\alpha\beta}(\omega) = J_{\alpha\beta}(\omega) + iS_{\alpha\beta}(\omega), \quad (2.21)$$

where $J_{\alpha\beta}(\omega)$ is the power spectrum of the environment and $S_{\alpha\beta}(\omega)$ leads to an energy shift in the system Hamiltonian which is often neglected as a small correction. This energy shift term commutes with system Hamiltonian due to the definition of the $\hat{A}_\alpha$ in Eq. (2.12). The Markovian master equation in Eq. (2.20) can then be recast as

$$\frac{d\rho(t)}{dt} = -i[\hat{H}_I, \rho(t)] + \mathcal{D}\rho(t), \quad (2.22)$$

where

$$\mathcal{D}\rho \equiv \sum_\omega \sum_{\alpha,\beta} J_{\alpha\beta}(\omega)\Big(\hat{A}_\alpha(\omega)\rho(t)\hat{A}_\beta^\dagger(\omega) - \frac{1}{2}\{\hat{A}_\beta^\dagger(\omega)\hat{A}_\alpha(\omega), \rho(t)\}\Big) \quad (2.23)$$

is the dissipator of the master equation describing the non-unitary evolution of the system. In general, this Markovian master equation can be cast in Lindblad form by diagonalising the matrix $J_{\alpha\beta}$ such that,

$$\frac{d\rho(t)}{dt} = -i[\hat{H}_I, \rho(t)] + \sum_{\omega}\sum_{i} \tilde{J}_{ii}(\omega)\mathcal{D}[\hat{A}_i(\omega)]\rho(t), \tag{2.24}$$

where $\tilde{J}_{ii}$ is the diagonalised power spectrum matrix and $\mathcal{D}[\hat{A}]\rho = \hat{A}\rho\hat{A}^\dagger - 1/2\{\hat{A}^\dagger\hat{A}, \rho\}$ is the action of Lindblad operator on the density matrix. From this point onward we neglect the $\hat{O}$ notation and assume that operators are in the Schrödinger representation unless indicated by $\tilde{O}$.

2.3 Single Quantum Dot Coupled to Fermionic Reservoirs

We now apply the theory presented in the previous section to the example of a single quantum dot coupled to two fermionic reservoirs (left and right leads). Considering the basis states $|0\rangle$ for N charge carriers on the dot, and $|1\rangle$ for $N+1$ charge carriers on the dot, the total Hamiltonian is

$$H = H_0 + H_l + H_{el}, \tag{2.25}$$

$$H_0 = \epsilon|1\rangle\langle 1|, \tag{2.26}$$

$$H_l = \sum_k (\epsilon_k - \mu_l) d_{kl}^\dagger d_{kl} + (\epsilon_k - \mu_r) d_{kr}^\dagger d_{kr}, \tag{2.27}$$

$$H_{el} = \sum_k \sum_{i=l,r} t_i (d_{ki}^\dagger c + d_{ki} c^\dagger), \tag{2.28}$$

where ϵ is the chemical potential of the dot, $d_{kl(r)}^\dagger$ and $d_{kl(r)}$ are the creation and annihilation operators for the k^{th} mode in the left(right) lead. The operators $c = |0\rangle\langle 1|$ and $c^\dagger = |1\rangle\langle 0|$ act on the quantum dot occupation. From the interaction Hamiltonian H_{el} and diagonal H_0 we can identify the system and environment operators as $\hat{A} \in \{c, c^\dagger\}$ and $\hat{B} \in \{d_{kl}, d_{kl}^\dagger, d_{kr}, d_{kr}^\dagger\}$. The reservoir correlation functions are calculated by assuming that each lead is in a thermal state at temperature T such that

$$\rho_{Ei} = \frac{1}{\mathcal{Z}_p} e^{-\beta H_{li}} = \frac{1}{\mathcal{Z}_p} \sum_k e^{-\beta\epsilon_{ki}} |\epsilon_{ki}\rangle\langle\epsilon_{ki}|, \tag{2.29}$$

where $\beta = (k_B T)^{-1}$ is the thermal energy of the bath, $\mathcal{Z}_p = \mathrm{tr}(e^{-\beta H_{li}})$ is the partition function of the i^{th} lead, and $|\epsilon_{ki}\rangle$ is the state corresponding to the mode of energy ϵ_{ki} in the i^{th} lead. The correlation functions for the i^{th} lead are then

$$\langle d_{ki}^\dagger d_{ki}\rangle = f(\epsilon_{ki}), \tag{2.30}$$

$$\langle d_{ki} d_{ki}^\dagger\rangle = 1 - f(\epsilon_{ki}), \tag{2.31}$$

$$\langle d_{ki} d_{kj}\rangle = \langle d_{ki} d_{kj}\rangle = 0, \tag{2.32}$$

where $f(\epsilon_k) = [1 + e^{\beta(\epsilon_{ki}-\mu_i)}]^{-1}$ and $\beta = (k_B T)^{-1}$. From this we see that the $\Gamma_{\alpha\beta}$ matrix is diagonal, and thus we can directly use the Lindblad form of the quantum master equation in Eq. (2.24). We first require the interaction representation of the system and environment interaction operators, $\tilde{A}(t) \in \{ce^{-i\epsilon t}, c^\dagger e^{i\epsilon t}\}$ and $\tilde{B}(t) \in \{\sum_{ki} t_{ki} d_{ki} e^{-i\epsilon_{ki} t}, \sum_{ki} t_{ki} d_{ki}^\dagger e^{i\epsilon_{ki} t}\}$ for $i \in \{l, r\}$. We can then write the dissipator for the leads in the form of Eq. (2.20) as

$$\mathcal{L}_{\text{leads}} = \sum_{i=\text{L,R}} \Gamma_i(cc^\dagger\rho - c^\dagger\rho c) + \overline{\Gamma}_i(c^\dagger c\rho - c\rho c^\dagger) + \Gamma_i^*(\rho cc^\dagger - c^\dagger\rho c) + \overline{\Gamma}_i^*(\rho c^\dagger c - c\rho c^\dagger), \tag{2.33}$$

where the rates are

$$\Gamma_i = \sum_k \int_0^\infty d\tau e^{i(\epsilon_{ki}-\epsilon)\tau} |t_i|^2 f_i(\epsilon_{ki}), \tag{2.34}$$

$$\overline{\Gamma}_i = \sum_k \int_0^\infty d\tau e^{-i(\epsilon_{ki}-\epsilon)\tau} |t_i|^2 [1 - f_i(\epsilon_{ki})]. \tag{2.35}$$

Extending the sum over reservoir modes to an integral over the density of states g_i in the wide-band approximation[1], $\sum_k \to \int_{-\infty}^{+\infty} d\epsilon_{ki} g_i$ and using the Cauchy relation, $\int_0^\infty ds e^{\pm i\epsilon_0 s} = \pi\epsilon_0 \pm i\frac{\mathcal{P}}{\epsilon_0}$ where $\mathcal{P}$ is the principal value, allows us to write the rates in terms of real and imaginary components

$$\Gamma_i = \pi g_i |t_i|^2 f_i(\epsilon) + i\mathcal{P}\int_{-\infty}^{+\infty} \epsilon_{ki} g_i |t_i|^2 \frac{f_i(\epsilon_{ki})}{\epsilon_{ki} - \epsilon}, \tag{2.36}$$

$$\overline{\Gamma}_i = \pi g_i |t_i|^2 [1 - f_i(\epsilon)] + i\mathcal{P}\int_{-\infty}^{+\infty} \epsilon_{ki} g_i |t_i|^2 \frac{1 - f_i(\epsilon_{ki})}{\epsilon_{ki} - \epsilon}. \tag{2.37}$$

[1]The wide-band approximation assumes that detailed structure of the density of states in the leads does not influence charge transport on the energy scale of the dot system [93].

The imaginary parts leads to a renormalisation of the system Hamiltonian as discussed in the previous section, and the real parts determine the dissipator rates in Lindblad form,

$$\mathcal{L}_{\text{leads}}\rho = -\Big(W_{\text{L}}\mathcal{D}[c^\dagger]\rho + \overline{W}_{\text{L}}\mathcal{D}[c]\rho + W_{\text{R}}\mathcal{D}[c^\dagger]\rho + \overline{W}_{\text{R}}\mathcal{D}[c]\rho\Big), \tag{2.38}$$

where $W_i = \Gamma_i f_i(\epsilon)$, $\overline{W}_i = \Gamma_i[1 - f_i(\epsilon)]$, and $\Gamma_i = \pi g_i |t_i|^2$. This dissipator describes an electron entering the dot with rate W_{L} from the left lead and W_{R} from the right lead, and leaving the dot with rate $\overline{W}_{\text{L}}$ to the left lead and $\overline{W}_{\text{R}}$ to the right lead. Schematics of a single quantum dot coupled to left and right leads are shown in Figure 2.1 for positive and negative bias.[2]

The current through the dot can be computed using the steady state solution of the weak-coupling master equation by considering the dot occupation and rates into and out of the dot at one barrier. With e denoting the electronic charge and ρ_{ss} the steady state solution of the Lindblad master equation with dissipator given in Eq. (2.38), the steady state current flowing though the SQD[3] at the barrier with the right lead is

$$I = e\Big[\overline{W}_{\text{R}}\text{Tr}(\rho_{\text{ss}}|1\rangle\langle 1|) - W_{\text{R}}\text{Tr}(\rho_{\text{ss}}|0\rangle\langle 0|)\Big]. \tag{2.39}$$

An equivalent expression holds for the barrier with the left lead which, due to conservation of charge, yields the same result. An example of the steady state current computed using this approach[4] is shown in Figure 2.1(b). We consider positive charge carriers (i.e. holes) as a relevant example for the experiments in Chapter 3. Transient current can be computed by replacing ρ_{ss} with $\rho(t)$ as the density matrix evolves in time.

Extending lead coupling to a double quantum dot involves expressing the system operators in the system eigenbasis. The rates relating to the dissipators for these operators are thus weighted by the support of each eigenstate on the relevant dot

[2]We choose the convention that $eV_{\text{bias}} = \mu_l - \mu_r$ to match experimental results in this thesis where the bias voltage is applied to the left lead.

[3]We define positive current to consist of positive charge flowing from left to right.

[4]Simulations presented in this chapter use the differentiable solver outlined in Chapter 6. Typical computation times and a comparisons with a standard solver are shown in Figure 6.2.

(depending on which lead the rate relates to). The steady state current is similarly obtained by considering the barrier with a lead and its neighbouring dot.

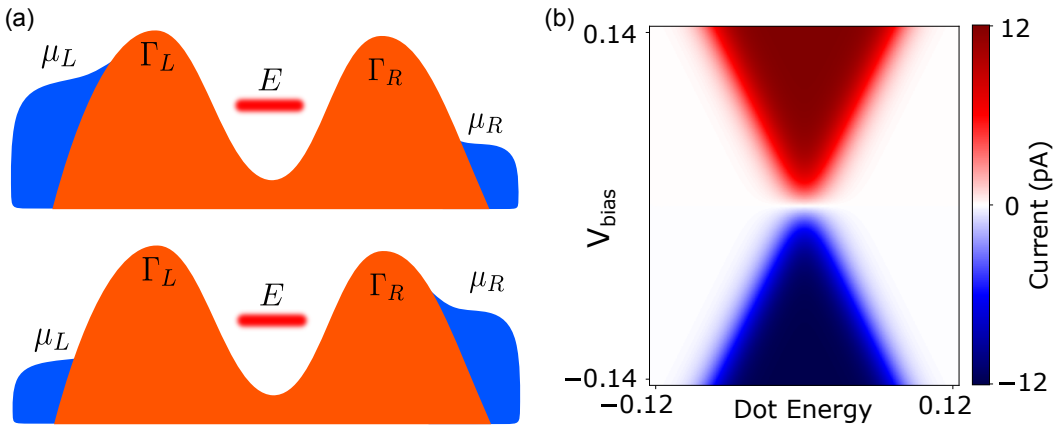

Figure 2.1: (a) Schematics of a single quantum dot at positive bias (upper) and negative bias (lower). (b) Example of current computed by numerically solving a weak-coupling master equation with dissipators given by Eq. (2.38). Parameter values used are, $\Gamma_{\mathrm{L}} = \Gamma_{\mathrm{R}} = 150\mathrm{MHz}$ and $T = 100\mathrm{mK}$.

2.4 Electron-Phonon Interaction

In this section we shall discuss the interaction of electrons and phonons in a solid state environment such as a semiconductor crystal. We present a brief discussion of the general theory of electron-phonon interactions, paying specific attention to acoustic phonons and the two dominant coupling mechanisms; deformation potential and piezoelectric. We then discuss the spectral density of a phonon bath as experienced by a double quantum dot in varying dimensions. The analysis in this section is framed in the context of electrons, but the same theory is valid for holes [94].

2.4.1 General Electron-Phonon Interaction

In a system of ions and electrons, the interaction between an electron located at $\mathbf{r}_i$ and an ion located at $\mathbf{R}_j$ can be assumed to only depend on the distance between them. Summing over all electrons and ions gives the interaction Hamiltonian,

$$H_{ei} = \sum_{ij} V_{ei}(\mathbf{r}_i - \mathbf{R}_j). \tag{2.40}$$

We decompose the vector $\mathbf{R}_j$ into an ionic equilibrium position $\mathbf{R}_j^0$ and a displacement $\mathbf{Q}_j$ such that $\mathbf{R}_j = \mathbf{R}_j^0 + \mathbf{Q}_j$. As the displacements are usually small, we may Taylor expand the interaction potential,

$$\sum_j V_{ei}(\mathbf{r}_i - \mathbf{R}_j^0 - \mathbf{Q}_j) = \sum_j \Big[V_{ei}(\mathbf{r}_i - \mathbf{R}_j^0) - \mathbf{Q}_j \cdot \nabla V_{ei}(\mathbf{r}_i - \mathbf{R}_j^0) + O(Q^2)\Big]. \quad (2.41)$$

The constant term $\sum_j V_{ei}(\mathbf{r}_i - \mathbf{R}_j^0)$ is the potential experienced by electrons when the ions are unperturbed, forming a periodic potential for which Bloch functions are the solution. The term linear in $\mathbf{Q}_j$ constitutes the electron-phonon interaction, and we neglect terms of higher order. The Born-Oppenheimer approximation is what follows from assuming small ion displacements and a known equilibrium solution.

We then have the electron-phonon interaction potential

$$V_{ep}(\mathbf{r}) = -\sum_j \mathbf{Q}_j \cdot \nabla V_{ei}(\mathbf{r}_i - \mathbf{R}_j^0), \quad (2.42)$$

and by considering its Fourier transform $V_{ep}(\mathbf{r}) = N^{-1}\sum_{\mathbf{q}} \tilde{V}_{ep}(\mathbf{q}) e^{i\mathbf{q}\cdot\mathbf{r}}$ we find $V_{ep}(\mathbf{r})$ in terms of wavevectors,

$$V_{ep}(\mathbf{r}) = -\frac{i}{N}\sum_{\mathbf{q}} \mathbf{q}\tilde{V}_{ei}(\mathbf{q}) e^{i\mathbf{q}\cdot\mathbf{r}} \cdot \left(\sum_j \mathbf{Q}_j e^{-\mathbf{q}\cdot\mathbf{R_j^0}}\right). \quad (2.43)$$

Using $\mathbf{Q_q} = \frac{i}{N}\sum_j \mathbf{Q}_j e^{-\mathbf{q}\cdot\mathbf{R_j^0}}$, we can express the displacement operator in terms of phonon creation and annihilation operators [95] as

$$\mathbf{Q_q} = \boldsymbol{\xi}_{\mathbf{q}} \left(\frac{\hbar}{2MN\omega_{\mathbf{k}}}\right)^{-\frac{1}{2}} (a_{\mathbf{q}} + a_{\mathbf{q}}^\dagger), \quad (2.44)$$

where M is the ion mass and $\boldsymbol{\xi}_{\mathbf{q}}$ is the polarization vector of the mode $\mathbf{q}$. Phonon wavevectors, $\mathbf{k}$, are only defined in the first Brillouin zone, but the vectors $\mathbf{q}$ are defined everywhere in momentum-space. The two vectors can be related by the reciprocal lattice vector $\mathbf{G}$. We may also use the mass density μ and lattice volume v to write $NM = \mu v$ to arrive at

$$V_{ep}(\mathbf{r}) = -\sum_{\mathbf{kG}} e^{i\mathbf{r}\cdot(\mathbf{k}+\mathbf{G})} V_{ei}(\mathbf{k}+\mathbf{G})(\mathbf{k}+\mathbf{G}) \cdot \boldsymbol{\xi}_{\mathbf{k}} \left(\frac{\hbar}{2\mu v\omega_{\mathbf{k}}}\right)^{-\frac{1}{2}} (a_{\mathbf{k}} + a_{\mathbf{k}}^\dagger). \quad (2.45)$$

Integrating this potential over the charge density of the solid, $\rho(\mathbf{r})$, gives the electron-phonon interaction,

$$\begin{aligned} H_{ep} &= \int d\mathbf{r}\rho(\mathbf{r})V_{ep}(\mathbf{r}) \\ &= -\sum_{\mathbf{kG}} \tilde{\rho}(\mathbf{k}+\mathbf{G})V_{ei}(\mathbf{k}+\mathbf{G})(\mathbf{k}+\mathbf{G})\cdot\boldsymbol{\xi}_{\mathbf{k}}\left(\frac{\hbar}{2\mu v\omega_{\mathbf{k}}}\right)^{-\frac{1}{2}}(a_{\mathbf{k}}+a_{\mathbf{k}}^{\dagger}), \end{aligned} \tag{2.46}$$

where $\tilde{\rho}(\mathbf{k}+\mathbf{G}) = \int d\mathbf{r}\rho(\mathbf{r})e^{i(\mathbf{k}+\mathbf{G})\cdot\mathbf{r}}$. This expression can be abbreviated to

$$H_{ep} = \sum_{\mathbf{kG}} M_{\mathbf{k}+\mathbf{G}}\tilde{\rho}(\mathbf{k}+\mathbf{G})(a_{\mathbf{k}}+a_{\mathbf{k}}^{\dagger}), \tag{2.47}$$

where

$$M_{\mathbf{k}+\mathbf{G}} = -V_{ei}(\mathbf{k}+\mathbf{G})(\mathbf{k}+\mathbf{G})\cdot\boldsymbol{\xi}_{\mathbf{k}}\left(\frac{\hbar}{2\mu v\omega_{\mathbf{k}}}\right)^{-\frac{1}{2}}. \tag{2.48}$$

2.4.2 Acoustic Phonons

Deformation Potential Interaction

Deformation potential coupling to acoustic phonons is the long-wavelength limit of Eq. (2.47) where only $\mathbf{G} = 0$ is retained. We assume the electron-ion interaction potential is a constant $V_{ei}(\mathbf{k}) \to D$ as $\mathbf{k} \to 0$ where D is the deformation constant. For long-wavelength acoustic phonons $\boldsymbol{\xi} \to \hat{\mathbf{k}}$, so we have

$$H_{ep}^{D} = D\sum_{\mathbf{k}}\left(\frac{\hbar}{2\mu v\omega_{\mathbf{k}}}\right)^{-\frac{1}{2}}|\mathbf{k}|\tilde{\rho}(\mathbf{k})(a_{\mathbf{k}}+a_{\mathbf{k}}^{\dagger}). \tag{2.49}$$

Deformation constants are obtained by measuring how energy bands shift when pressure is applied on the solid.

Piezoelectric Interaction

A piezoelectric crystal will generate an electric field when squeezed. Many semiconductors are piezoelectric; III-V semiconductors are weakly piezoelectric and II-VI semiconductors are extremely piezoelectric. In contrast, group IV semiconductors are not piezoelectric as their crystal structures have an inversion centre. The following is a heuristic derivation of the piezoelectric electron-phonon coupling potential.

The electric field is proportional to the stress S_{lm} on the crystal such that

$$E_n = \sum_{lm} M_{lmn}S_{lm}, \tag{2.50}$$

where the matrix element M_{lmn} is a constant determining the proportionality. Stress is defined as the symmetric derivative of the displacement field,

$$S_{lm} = \frac{1}{2}\left(\frac{\partial Q_l}{\partial x_m} + \frac{\partial Q_m}{\partial x_l}\right). \tag{2.51}$$

Using the displacement operator defined in terms of phonon creation and annihilation operators we find

$$S_{lm} = \frac{1}{2}\sum_{\mathbf{k}}\left(\frac{\hbar}{2\mu v\omega_{\mathbf{k}}}\right)^{-\frac{1}{2}}(\xi_l k_m + \xi_m k_l)(a_{\mathbf{k}} + a_{\mathbf{k}}^\dagger)e^{i\mathbf{k}\cdot\mathbf{r}}. \tag{2.52}$$

It can be shown that the electric field is longitudinal and points in the direction $\hat{\mathbf{k}}$ of the phonon mode [95]. Writing the electric field in terms of a potential we find

$$E_n \propto -\frac{\partial}{\partial x_n}\phi(\mathbf{r}) = -\frac{1}{\sqrt{v}}\sum_{\mathbf{k}} ik_n\phi_{\mathbf{k}}e^{i\mathbf{r}\cdot\mathbf{k}}. \tag{2.53}$$

Using these results we can observe that the potential is proportional to the displacement such that

$$\phi(\mathbf{r}) = i\sum_{\mathbf{k}}\left(\frac{\hbar}{2\mu v\omega_{\mathbf{k}}}\right)^{-\frac{1}{2}} M_\lambda(\hat{\mathbf{k}})(a_{\mathbf{k}} + a_{\mathbf{k}}^\dagger)e^{i\mathbf{k}\cdot\mathbf{r}}, \tag{2.54}$$

where λ indicates the polarisation of the mode. Treating $\phi(\mathbf{r})$ as $V_{ep}(\mathbf{r})$ from previous discussion, the electron-phonon interaction is then

$$H_{ep}^P = i\sum_{\mathbf{k}}\left(\frac{\hbar}{2\mu v\omega_{\mathbf{k}}}\right)^{-\frac{1}{2}} M_\lambda(\hat{\mathbf{k}})\rho(\mathbf{k})(a_{\mathbf{k}} + a_{\mathbf{k}}^\dagger). \tag{2.55}$$

The matrix element $M_\lambda(\hat{\mathbf{k}})$ only depends on the direction of the wavevector and not its magnitude, and depends on the polarisation of the acoustic phonon mode. It also has the property $M_\lambda(-\hat{\mathbf{k}}) = -M_\lambda(\hat{\mathbf{k}})$ to ensure H_{ep} is Hermitian. The piezoelectric interaction is in general quite anisotropic, but often a constant value obtained from angular averaging is used such that $M_\lambda(\hat{\mathbf{k}}) = P$.

Combined Effect

The same acoustic phonon may interact with an electron via deformation potential and piezoelectric coupling. The total interaction can be written as

$$H_{ep}^P = i\sum_{\mathbf{k}}\left(\frac{\hbar}{2\mu v\omega_{\mathbf{k}}}\right)^{-\frac{1}{2}} \bar{M}(\mathbf{k})\rho(\mathbf{k})(a_{\mathbf{k}} + a_{\mathbf{k}}^\dagger), \tag{2.56}$$

where

$$\bar{M}(\mathbf{k}) = D|\mathbf{k}| + iP. \tag{2.57}$$

As the deformation potential and piezoelectric interactions are out of phase, we have

$$|\bar{M}|^2 = D^2k^2 + P^2, \tag{2.58}$$

and therefore they can be treated separately in any second order treatment of electron-phonon interactions.

2.4.3 Spectral Densities

Spin-Boson Model

The standard spin-boson Hamiltonian is given by

$$H = \frac{1}{2}(\epsilon\sigma_z + \Delta\sigma_x) + \sum_{\mathbf{k}} \omega_{\mathbf{k}} a^\dagger_{\mathbf{k}} a_{\mathbf{k}} + \sigma_z \sum_{\mathbf{k}} \lambda_{\mathbf{k}}(a_{\mathbf{k}} + a^\dagger_{\mathbf{k}}), \tag{2.59}$$

where ϵ is the detuning of the two-level system energies, Δ is a tunneling rate between the system states, $\omega_{\mathbf{k}}$ is the angular frequency of the bosonic mode with wavevector $\mathbf{k}$, $\lambda_{\mathbf{k}}$ is the coupling strength of the system to the mode with frequency $\omega_{\mathbf{k}}$, and $a^\dagger_{\mathbf{k}}(a_{\mathbf{k}})$ are the creation(annihilation) operators associated with a mode with frequency $\omega_{\mathbf{k}}$. Assuming the bosonic environment is in thermal equilibrium, the influence of the environment on the system is completely described by a spectral density function, $J(\omega)$, defined as

$$J(\omega) \equiv \sum_{\mathbf{k}} |\lambda_{\mathbf{k}}|^2 \delta(\omega - \omega_{\mathbf{k}}). \tag{2.60}$$

Double Quantum Dot

A system of interest for electron-phonon interactions is a double quantum dot as these interactions are necessary to explain off-resonant transport features, and dephasing effects in qubits. We assume a single excess electron in the system and define a basis of $\{|L\rangle, |R\rangle\}$ corresponding to the electron occupying the left and right dot respectively. This is a two-level system which can be mapped to the spin-boson Hamiltonian.

As discussed in Appendix B the angular form factor $F(\omega)$ of the spectral density for the electron-phonon interaction with a double quantum dot in 3-dimensions is

$$F(\omega) = \frac{v}{\pi^2 c d^2}\left(\frac{\omega}{\omega_d}\right)^2\left(1 - \operatorname{sinc}\frac{\omega}{\omega_d}\right)e^{-\frac{\omega^2}{2\omega_a^2}}, \tag{2.61}$$

where $\omega_d = \frac{2\pi c}{d}$ and $\omega_a = \frac{2\pi c}{a}$, with d the centre-to-centre separation of the dots, a the length scale of the dots, and c the speed of sound in the crystal. Following Appendix B, the form of $M_{\mathbf{k}}$ are also found to be

$$M_{\mathbf{k}} = D\left(\frac{\hbar}{2\mu v \omega_{\mathbf{k}}}\right)^{-\frac{1}{2}}|\mathbf{k}| \tag{2.62}$$

for deformation potential coupling, and

$$M_{\mathbf{k}} = iP\left(\frac{\hbar}{2\mu v \omega_{\mathbf{k}}}\right)^{-\frac{1}{2}} \tag{2.63}$$

for piezoelectric coupling. The results lead to different ω dependence of the phonon spectral densities when coupling via deformation potential or piezoelectric interactions to the double quantum dot [96]:

$$J_{3D}^{D}(\omega) = \frac{D^2\hbar}{2\pi^2\mu c^2 d^3}\left(\frac{\omega}{\omega_d}\right)^3\left(1 - \operatorname{sinc}\frac{\omega}{\omega_d}\right)e^{-\frac{\omega^2}{2\omega_a^2}}, \tag{2.64a}$$

$$J_{3D}^{P}(\omega) = \frac{P^2\hbar}{2\pi^2\mu c^2 d}\,\frac{\omega}{\omega_d}\left(1 - \operatorname{sinc}\frac{\omega}{\omega_d}\right)e^{-\frac{\omega^2}{2\omega_a^2}}. \tag{2.64b}$$

Varying Dimensions

Thus far, we have assumed that the phonons exist in a 3D bulk crystal. As this may not always be the case in the system of interest, we shall derive the respective spectral densities in 2D and 1D crystals. This is straightforward, as we only need to omit angular parts of the 3D integral previously performed. The crystal volume and mass density notation shall remain as v and μ, but they represent relevant quantities in the dimensionality under consideration. For 2D spectral densities, the polar integral is not required so the angular form factor is,

$$F_{2D}(\omega) = \frac{v}{2\pi^2 c d}\,\frac{\omega}{\omega_d}\left[1 - J_0\left(\frac{\omega}{\omega_d}\right)\right]e^{-\frac{\omega^2}{2\omega_a^2}}. \tag{2.65}$$

In a 1D system, we note that the phase difference term becomes $1 - e^{ik_z d}$ (where we assume the dots lie along the z-axis). This results in a form factor of

$$F_{1D}(\omega) = \frac{v}{4\pi^3}\left(1 - \cos\frac{\omega}{\omega_d}\right)e^{-\frac{\omega^2}{2\omega_a^2}}. \tag{2.66}$$

The spectral densities acquired in different dimensions are summarised in Table 2.1 and their ω dependence is shown in Figure 2.2. Without considering the material specific prefactors, it can be observed that the piezoelectric interaction is weaker, but more consistent in magnitude across dimensions, than the deformation potential interaction. For the remainder of this thesis, we neglect the details of the constant prefactors of each spectral density and instead use the amplitude J_0 to set the energy scale of the spectral densities, and therefore the electron-phonon interaction strength.

	Phonon Spectral Density: $J(\omega)$	
Dimension	Deformation Potential	Piezoelectric
3D	$\frac{D^2\hbar}{2\pi^2\mu c^2 d^3}\left(\frac{\omega}{\omega_d}\right)^3\left(1-\text{sinc}\,\frac{\omega}{\omega_d}\right)e^{-\frac{\omega^2}{2\omega_a^2}}$	$\frac{P^2\hbar}{2\pi^2\mu c^2 d}\frac{\omega}{\omega_d}\left(1-\text{sinc}\,\frac{\omega}{\omega_d}\right)e^{-\frac{\omega^2}{2\omega_a^2}}$
2D	$\frac{D^2\hbar}{4\pi^2\mu c^2 d^2}\left(\frac{\omega}{\omega_d}\right)^2\left[1-J_0\left(\frac{\omega}{\omega_d}\right)\right]e^{-\frac{\omega^2}{2\omega_a^2}}$	$\frac{P^2\hbar}{4\pi^2\mu c^2}\left[1-J_0\left(\frac{\omega}{\omega_d}\right)\right]e^{-\frac{\omega^2}{2\omega_a^2}}$
1D	$\frac{D^2\hbar}{8\pi^3\mu c^2 d}\frac{\omega}{\omega_d}\left(1-\cos\frac{\omega}{\omega_d}\right)e^{-\frac{\omega^2}{2\omega_a^2}}$	$\frac{P^2\hbar d}{8\pi^3\mu c^2}\frac{\omega_d}{\omega}\left(1-\cos\frac{\omega}{\omega_d}\right)e^{-\frac{\omega^2}{2\omega_a^2}}$

Table 2.1: A summary of the phonon spectral density functions for deformation potential and piezoelectric interactions with a double quantum dot in varying crystal dimensions. A similar table of spectral densities can be found in Ref. [96].

2.5 Double Quantum Dot Coupled to a Phonon Bath

Combining the discussion of the previous two sections, we derive a quantum master equation for a double quantum dot coupled to a phonon bath. The basis states of a double quantum dot system are typically $|L\rangle$ for an excess charge on the left

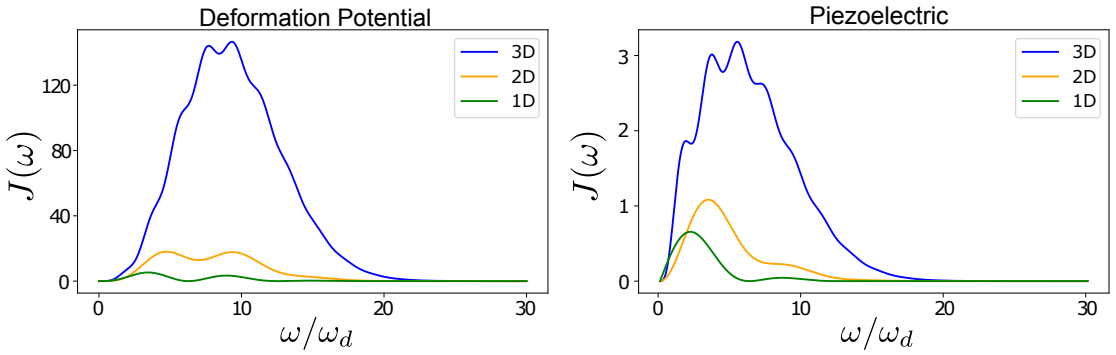

Figure 2.2: The form of the phonon spectral density, $J(\omega)$, for deformation potential (left) and piezoelectric (right) electron-phonon interaction for a double quantum dot system. The prefactor terms in Table 2.1 are set equal to unity for a more clear comparison of the ω/ω_d dependence. Parameters are set to $c = 3000$ ms^{-1}, $d = 100$ nm, and $a = 20$ nm such that $\omega_d = 30$ GHz and $\omega_a = 150$ GHz.

dot, $|R\rangle$ for an excess charge on the right dot, and $|0\rangle$ for no excess charges in the double quantum dot. These states are motivated by the large Coulomb repulsion energy experienced by adding additional charges, leading to a maximum of one excess charge in the double quantum dot. The phonon bath couples to charge density in the double quantum dot which is relevant to the $|L\rangle$ and $|R\rangle$ states; a detailed derivation of the coupling via these states is outlined in Appendix B. The $|0\rangle$ state is required when considering coupling to fermionic leads, particularly for sequential tunnelling of a charge through the dots, but not coupling to a phonon bath. In this analysis, we again consider positive charge carriers as a relevant example for the experiments in Chapter 3. We begin by stating the Hamiltonian of the system, environment, and their interaction as

$$H = H_0 + H_p + H_{ep}, \tag{2.67}$$

$$H_0 = \frac{\epsilon}{2}\sigma_z + t_c\sigma_x, \tag{2.68}$$

$$H_p = \sum_{\mathbf{k}} \omega_{\mathbf{k}} a^\dagger_{\mathbf{k}} a_{\mathbf{k}}, \tag{2.69}$$

$$H_{ep} = \sigma_z \sum_{\mathbf{k}} \lambda_{\mathbf{k}} (a^\dagger_{\mathbf{k}} + a_{\mathbf{k}}), \tag{2.70}$$

were σ_μ are the Pauli operators in the subspace $|L\rangle$ and $|R\rangle$, $\epsilon = \epsilon_l - \epsilon_r$ is the detuning between the dot energy levels, and t_c is the interdot tunnel rate. The phonon bath is described by H_p where $a^\dagger_{\mathbf{k}}(a_{\mathbf{k}})$ are the creation(annihilation) operators

for the phonon mode of angular frequency $\omega_{\mathbf{k}}$. The electron-phonon interaction is described by H_{ep} where $\lambda_{\mathbf{k}}$ is the coupling constant between the dots and the phonons. A schematic of a double quantum dot coupled to a phonon bath and fermionic leads is shown in Figure 2.3(a).

The phonon dissipator is most conveniently expressed in terms of the eigenstates of H_0, which for positive detuning are

$$|+\rangle = \cos(\theta/2)|L\rangle - \sin(\theta/2)|R\rangle \tag{2.71}$$

$$|-\rangle = \sin(\theta/2)|L\rangle + \cos(\theta/2)|R\rangle, \tag{2.72}$$

with energy $\omega_{\pm} = \pm\sqrt{\epsilon^2/4 + t_c^2}$. For negative detuning, the states $|L\rangle$ and $|R\rangle$ are swapped in the above definition of the eigenstates. The energy splitting between the excited and ground states is $\omega_p = (\omega_+ - \omega_-)$, and $\theta = \arctan(2t_c/\epsilon)$. The interaction Hamiltonian H_{ep} can then be recast in this basis and in the interaction representation as

$$\tilde{H}_{ep}(t) = \sum_{\nu,\mathbf{k}} \Big(A(\nu)e^{-i\nu t} + A^\dagger(\nu)e^{i\nu t}\Big)\lambda_{\mathbf{k}}\Big(a_{\mathbf{k}}e^{-i\omega_{\mathbf{k}}t} + a_{\mathbf{k}}^\dagger e^{i\omega_{\mathbf{k}}t}\Big), \tag{2.73}$$

where $\nu \in \{0, \omega_p\}$, $A(0) = (\cos^2(\theta/2) - \sin^2(\theta/2))|+\rangle\langle+| + (\sin^2(\theta/2) - \cos^2(\theta/2))|-\rangle\langle-|$ and $A(\omega_p) = \sin(\theta)|-\rangle\langle+|$. Identifying the system and bath operators as used in Eq. (2.16) and Eq. (2.19) we calculate the bath correlation functions by assuming that the bath is in a thermal state at temperature T such that

$$\rho_E = \frac{1}{\mathcal{Z}_p}e^{-\beta H_p} = \frac{1}{\mathcal{Z}_p}\sum_{\mathbf{k}} e^{-\beta\omega_{\mathbf{k}}}|\mathbf{k}\rangle\langle\mathbf{k}|, \tag{2.74}$$

where $\beta = (k_B T)^{-1}$ is the thermal energy of the bath, $\mathcal{Z}_p = \mathrm{tr}(e^{-\beta H_p})$ is the phonon bath partition function, and $|\mathbf{k}\rangle$ is the state corresponding to the phonon mode of energy $\omega_{\mathbf{k}}$. We then have

$$\langle b_i b_j\rangle = \langle b_i^\dagger b_j^\dagger\rangle = 0, \tag{2.75}$$

$$\langle b_i b_j^\dagger\rangle = \delta_{ij}[n(\omega_i) + 1], \tag{2.76}$$

$$\langle b_i^\dagger b_j\rangle = \delta_{ij}n(\omega_i), \tag{2.77}$$

where $n(\omega) = [e^{-\beta\omega} - 1]^{-1}$ is the Bose-Einstein occupation of the bath. From this we can see that the $\Gamma_{\alpha\beta}$ matrix is diagonal and therefore we can use the Lindblad form of Eq. (2.24) to arrive at

$$\frac{d\rho(t)}{dt} = \gamma(\omega_p)\Big([n(\omega_p)+1]\mathcal{D}[|-\rangle\langle+|]\rho(t) + n(\omega_p)\mathcal{D}[|+\rangle\langle-|]\rho(t)\Big), \tag{2.78}$$

where $\gamma(\omega_p) = \sin^2\theta J(\omega_p)$ is the rate at which the phonon bath induces interdot charge transitions in the DQD, dictated by the phonon spectral density, $J(\nu)$. The functional form of $J(\nu)$ follows the discussion in the previous section with a summary in Table 2.1. The Bose-Einstein occupation of the phonon bath produces a temperature dependence on the phonon emission and absorption processes described by $\mathcal{D}[|-\rangle\langle+|]$ and $\mathcal{D}[|+\rangle\langle-|]$, respectively. As the DQD systems considered in this thesis are at low temperature ($T \approx 100$mK and $k_B T \ll \omega_p$), phonon emission processes dominate. We do not consider the dissipation associated with the eigenbasis operator $A(0)$ as $J(0) = 0$.

Example results of computing steady state current through a double quantum dot are shown in Figure 2.3 (b-d) where the effect of phonon assisted transport can clearly be seen when comparing (c) and (d) with (b) in which the phonon coupling rate is zero. The bias triangles formed by phonon assisted transport change direction at opposite bias. We have included coupling to leads and and computed the steady state current as discussed in Section 2.3.

2.6 Alternative Open Quantum Systems Methods

Having discussed the theory of weak-coupling quantum master equations in detail, we now briefly overview some alternative methods for modelling transport in open quantum systems.

Transport properties of quantum systems can be computed using transmission coefficients in a scattering formalism. In this framework, leads are considered as wave guides for plane waves into and out of a quantum system. The energy dependent transmission coefficient $\mathcal{T}(\epsilon)$ of these waves can be computed using Green's functions [97] or wavefunctions [98]. Tight-binding models are widely used when calculating

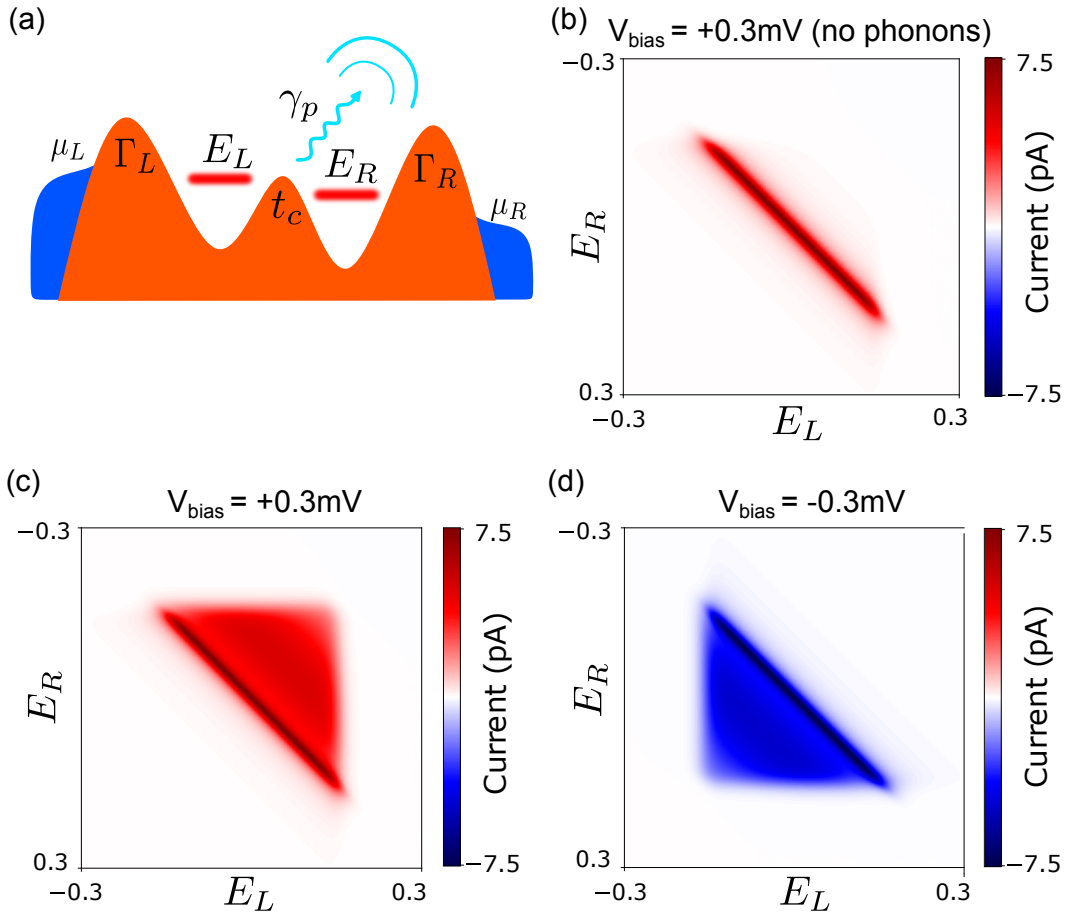

Figure 2.3: (a) Schematic of a double quantum dot at positive detuning and positive bias. (b) Example of current computed by numerically solving a weak coupling master equation with only dissipators associated with leads. Current computed over the same range while also including phonon dissipators at (c) positive bias and (d) negative bias. Parameter values used are, $\Gamma_{\mathrm{L}} = \Gamma_{\mathrm{R}} = 300\mathrm{MHz}$, $t_c = 2\mathrm{GHz}$ and $T = 100\mathrm{mK}$. The phonon coupling follows a 3D piezoelectric spectral density with $c_s = 3000\mathrm{ms}^{-1}$, $a = 20\mathrm{nm}$, and $d = 100\mathrm{nm}$, and $J_0 = 1\mathrm{GHz}$.

wavefunctions and conductance of quantum systems for a given potential landscape and crystal structure [98]. The well-known Landauer equation uses the transmission coefficient to determine the current through the quantum system as

$$I = \frac{e}{h}\int_{-\infty}^{\infty} \mathcal{T}(\epsilon)[f_{\mathrm{L}}(\epsilon) - f_{\mathrm{R}}(\epsilon)], \tag{2.79}$$

where $f_{\mathrm{L(R)}}$ is the Fermi occupations of the left(right) lead at energy ϵ. Scattering methods are most applicable when modelling resonant transport through a quantum system. Environmental effects such as phonon assisted transport are not easily captured by this approach, often requiring non-equilibrium Green's functions [99–

101]. Scattering theory and generalised quantum master equations have been shown to be equivalent in the limit of coherent transport [102].

In systems where single-charge tunnel events are important, such as in quantum dots, rate equations can be used to describe the population of each dot according to tunnel rates on and off the dots [97]. Such equations are the classical counterpart to the quantum master equations discussed in this chapter. Quantum master equations provide a more complete description of the system by considering the possibility of superpositions of basis states. This is most apparent when considering the interaction with phonons, as discussed in Section 2.5 for a double quantum dot.

Systems with strong coupling to phonon modes, such as molecular systems [102, 103], require a more detailed description of the environment interaction than provided by the weak-coupling regime considered in this thesis. Approaches such as the polaron frame [103], variational master equations [89], or even numerically exact methods using tensor networks [90, 91] may be used to describe a wide range of system-environment coupling strengths and mechanisms. While electron-phonon interactions are the focus of several aspects of this thesis, similar open quantum systems approaches can be employed to model the interaction of quantum dots with photons [96, 104]. Such interactions with photons are not considered in this thesis as the experimental systems do not involve electrically driving the quantum dots to induce transport [105, 106] or coupling to a cavity for readout [8].

The weak-coupling master equations discussed in this chapter are a suitable choice for modelling electrostatic quantum dot systems as the system environment coupling is typically weak for both fermionic leads and phonon baths in a bulk crystal at low temperature. Such models have limitations as they do not effectively describe cotunneling or lifetime broadening. Cotunneling is a higher order process involving the cooperative tunneling of multiple charges, but is not typically observed in transport measurements of suitably confined quantum dots tuned to the few charge regime. Lifetime broadening relates to the tunnel rates to leads being sufficiently fast that the dot levels experience a broadening of fermionic modes and therefore the resonant transport peak is wider. Lifetime broadening is not a

dominant effect for most device regimes, and the slow tunnel rates discussed in the following chapter mean that a model does not require lifetime broadening in order to be effective. Moving beyond the weak-coupling regime allows lifetime broadening to be well captured by a similar quantum master equation [102].

2.7 Discussion

We have derived the weak-coupling quantum master equations necessary to describe the quantum dot systems considered in this thesis. Weak-coupling master equations employ a series of approximations but remain powerful for describing a range of open quantum systems. A brief discussion of alternative approaches to open quantum systems highlights the breadth of the field, while also justifying our choice of model for the quantum dot systems under consideration. We model transport in quantum dot systems weakly coupled to leads, with a double quantum dot with an orbital excited state in Chapter 3, and consider models of a single quantum dot with an orbital excited state and a double quantum dot coupled to a phonon bath in Chapter 6. The discussion of electron-phonon interaction is particularly relevant to Chapter 6, but also provides insight into results in Chapter 3. In Chapter 6 we also develop a differentiable numerical solver for Lindblad master equations which can be applied more generally than the quantum dot models considered.

3

A Double Quantum Dot in the Sub-Attoampere Regime

All measurements presented in this chapter where carried out by the author using an existing experimental setup. The author performed all analysis of the experimental data, including the fitting of theoretical models.

This chapter considers an experimental study of a double quantum dot in a Ge/SiGe heterostructure device and the transport of charge through it. We focus on the case of slow tunnel rates, which allows for single-charge tunnel events to be observed using a charge sensor dot. Working in the slow tunnel rate regime means that lifetime broadening does not impact the transport through the dot and therefore the weak-coupling quantum master equations discussed in the previous chapter provide a relevant theoretical fit. We characterise tunnel rates using experimental and theoretical tools, before investigating phonon assisted transport through the double quantum dot.

We begin with analysis of charge state readout and discuss a method of counting individual charge transport events from source to drain leads through the double quantum dot. We estimate sub-attoampere currents through the double quantum dot at a range of biases by applying this method to time-trace measurements of

charge sensing data. We estimate the interdot tunnel rate using transition lifetimes in the same time-trace data, and fit the lead tunnel rates to the estimated current values using a quantum master equation model. Finally, we investigate the transition events which lead to inelastic transport of electrons mediated by the interaction with phonons in the semiconductor crystal, which is the first investigation of its kind in a Ge/SiGe device.

3.1 Tuning the Device

The double quantum dot is tuned in a Ge/SiGe heterostructure as outlined in Figure 1.4(b) with the gate electrode design shown in Figure 3.1(a). The horizontal gate voltages (4 and 12) are set to split the device into an upper and lower transport channel with the charge sensor on the upper channel controlled by gates 1-3 and a double quantum dot on the lower channel controlled by gates 7-11. Gates 8 and 10 predominantly act as plunger gates for the DQD electrochemical potentials, and 7, 9, and 11 predominantly act as barrier gates for the DQD. Gates 5 and 6 facilitate the formation of a third quantum dot in the lower segment, but we choose not to use these gates for the DQD to ensure maximum coupling to the charge sensor.

The DQD voltages are set such that the tunnel rates are very slow and therefore current through the DQD cannot be detected using our current amplifier. The charge state of the DQD is instead observed using a charge sensor dot, which is tuned to the edge of a Coulomb peak for maximum sensitivity. As the tunnel rates are slow, the edges of the stability diagram transitions appear noisy since the charge transfer events are on the order of the measurement timescales and the sensor detects the stochastic events near the transition line as shown in Figure 3.1(b) and (c).

3.2 Calibrating the Charge Sensor

In order to detect single-charge tunnelling events, we must first consider the calibration of charge-state readout using a charge senor dot. As shown in Figure 3.1(c) we can achieve good contrast in charge sensor current, I_{CS}, between the three

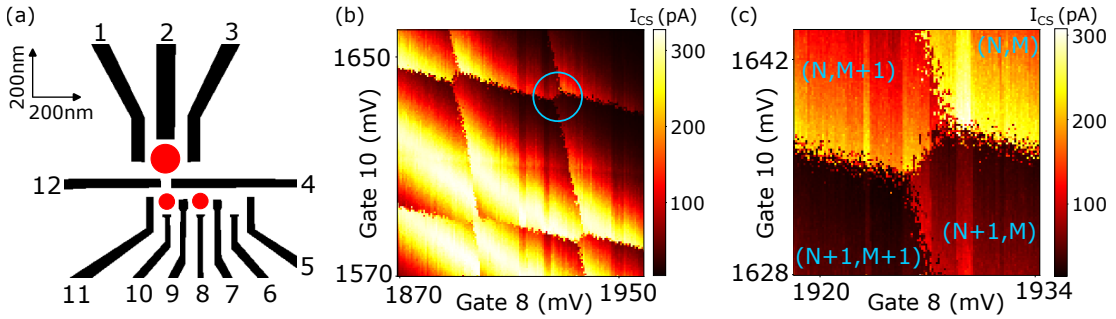

Figure 3.1: (a) Gate electrode design with gate numbers and nominal locations of quantum dots indicated in red. The larger upper dot acts as the charge sensor dot. (b) Charge sensing current I_{CS}, for a double quantum dot at zero bias tuned to the slow tunnel rate regime displaying a unit cell of the DQD stability diagram. (c) A zoomed scan of vertices of the stability diagram at zero bias (indicated on (b) with a blue circle) with charge states of each region labelled. The transitions appear noisy as a result of the individual charge transport events being detected during the integration time of the charge sensing measurement.

regions defined by a triple point. With sufficient signal to noise ratio, a classifier can be used to discriminate between the three regions based on a measurement of I_{CS} for a suitably short integration time (in our case, 5 ms). This is known as single-shot readout.

We calibrate the readout classifier by taking a time-trace measurement at the triple point of a DQD with zero bias across the DQD. We choose zero bias as it is easiest to determine a point in voltage space where all three charge state are equally occupied during a time-trace. By creating a histogram of I_{CS} values from the time-trace data, we find three distinct peaks as shown in Figure 3.2. The fidelity of these peaks is dependent on the readout point with respect to the DQD plunger voltages (being too far from one charge state region will result in only two peaks), and the charge sensor plunger voltage (being too far off a Coulomb peak will cause poor contrast between charge states). The integration time of each point measurement also plays a role; if the integration time is too short, the signal to noise ratio will decrease, but if the integration time is too long there may be transitions occurring during a single-shot measurement.

A model consisting of three Gaussian functions $\{\mathcal{N}(I_{CS}; \mu_i, \sigma_i)\}_{i=0}^{2}$ with means μ_i and standard deviations σ_i is fitted to these peaks from which we form a

classifier. Given a charge sensor current value I_{CS}, we classify the state according to $S(I_{\mathrm{CS}}) = \mathrm{argmax}_i\{\mathcal{N}(I_{\mathrm{CS}}; \mu_i^*, \sigma_i^*)\}_{i=0}^2$ where μ_i^* and σ_i^* are the fitted values. An example of this classifier fit to a histogram of I_{CS} values is shown in Figure 3.2. The three peaks correspond to three charge states, which depend on the triple point under consideration. One triple-point will host the $(N, M), (N+1, M), (N, M+1)$ charge states and the other will host $(N+1, M), (N, M+1), (N+1, M+1)$ charge states.

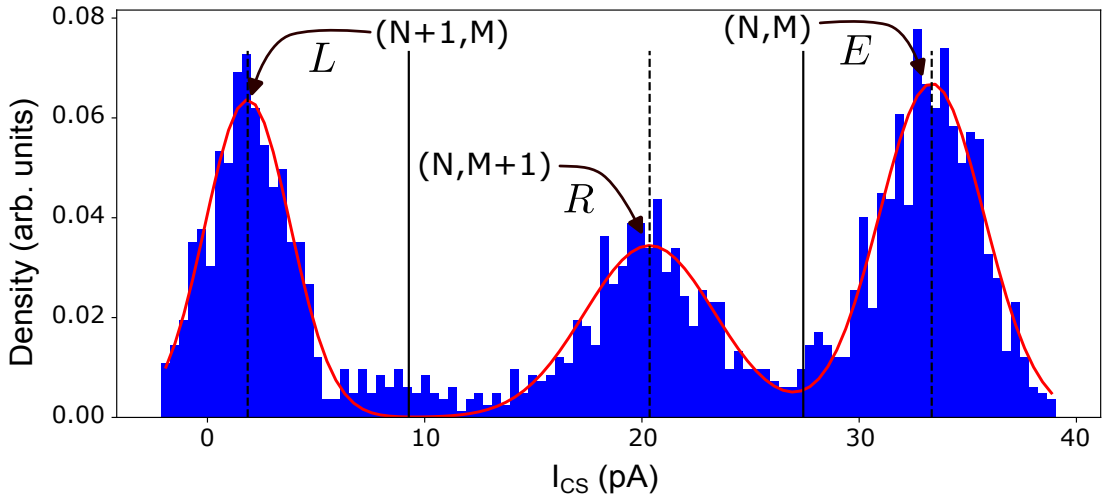

Figure 3.2: Typical calibration data for the triple point readout classifier. The Gaussian function fit is displayed over the histogram of charge sensor readout values from a time-trace of duration ≈ 1 minute with integration time 5ms. The dashed vertical lines indicate the location of the optimised means of the three Gaussian functions used for the fit, and the solid vertical lines indicate the decision boundaries determined by $S(I_{\mathrm{CS}})$. The DQD charge state and classifier state label are indicated for each peak. The state labels map as $L \equiv (N+1, M)$, $R \equiv (N, M+1)$, and $E \equiv (N, M)$. Small additional peaks (e.g. around 9 pA) are not explored further and are considered results of charge switches in the device during the readout trace.

3.3 Counting Charge Transitions

By observing transitions between sequential charge states surrounding a triple point, we can infer that a charge has moved through the double quantum dot from the left to the right lead (or vice-versa). For a charge to travel from the left lead to the right lead it must follow the sequence: $(N, M) \to (N+1, M) \to (N, M+1) \to (N, M)$ which constitutes a charge (hole) being loaded onto the left dot from the left lead, tunnelling to the right dot, and then onto the right lead. The same sequence in

reverse means a charge has moved from the right lead to the left. At the other triple point, the sequence $(N+1, M+1) \rightarrow (N+1, M) \rightarrow (N, M+1) \rightarrow (N+1, M+1)$ corresponds to transport of an anti-charge (electron) from the right reservoir to the left lead, which has the same effect on observed current as a charge travelling from left to right. These sequences are key to being able to easily determine the directionality of charge transfer, which is only achievable with a single quantum dot using more involved protocols [107, 108].

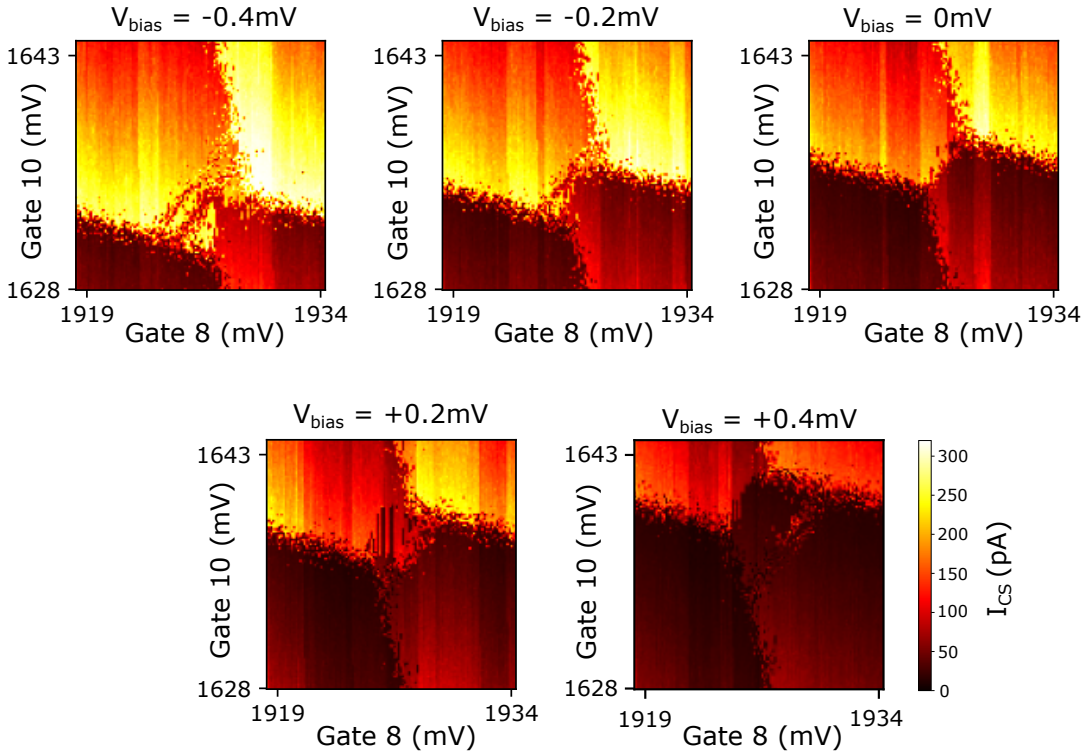

Figure 3.3: Double quantum dot transitions at a range of biases, measured using a charge sensor dot. All plots share the same axes and colour-scale. An applied bias opens a triangular area in which transport through the dot may occur. Elastic transport through the DQD occurs along the lines parallel to the base of the triangle. Elastic transport via an excited state can be observed in the data at negative bias voltages where there are multiple lines parallel to the base of the triangle. The bias voltage is applied to the left lead while the right is grounded, causing transition lines to shift along the Gate 10 axis and not the Gate 8 axis.

To detect current through the double quantum dot, we take a long time-trace measurement ($\approx$ 5 minutes) of charge sensing data and use our classifier to determine the charge state of the double quantum dot at each point in the measurement. We

can then define a sequence of charge states to search for in the time-trace and count the occurrences of that sequence. Based on the charge states labelled in Figure 3.2, we can define a sequence such as $[E, L, R, E]$ to represent the transit of a charge from left to right, and $[E, R, L, E]$ from right to left. Each time the sequence associated with charge transit in a particular direction occurs, we count a charge moving from one lead to the other through the dots. Equivalent sequences starting in a different charge state are equally valid, as the states must be occupied cyclically to constitute charge transit. Generating pulses to modulate gate voltages such that the DQD moves repeatedly through these sequences is known as shuttling which is useful for long-range entanglement of spins in quantum dot arrays [109, 110]. Pulsing with suitable frequencies can induce currents of sufficient magnitude to detect by typical current amplification equipment [69].

The $[E, L, R, E]$ and $[E, R, L, E]$ sequences only consider direct charge transfer events (i.e. the charge always moves sequentially in one direction), but we also wish to include indirect charge transfer events. For example, a charge may move backwards from one dot to the previous before continuing to move through the DQD as a result of stochastic quantum jumps between the charge eigenstates of the DQD. Sequences such as $[E, L, R, L, R, E]$ or $[E, R, L, R, L, E]$ describe first order indirect paths of a charge from left to right and right to left respectively, where the order of an indirect path is the number of backwards steps between the cyclic states. The net sum of charges travelling in each direction across the dot (denoted $n_{l\to r}$ and $n_{r\to l}$) in a period of time Δt gives a current value of

$$I_{\mathrm{DQD}} = |e|\frac{(n_{l\to r} - n_{r\to l})}{\Delta t}, \tag{3.1}$$

where e is the electronic charge, and we choose left to right to represent positive current due to transfer of a positive charge.

To investigate the behaviour of the double quantum dot we perform the long current trace at a point of elastic transport for a range of biases. We perform the trace at the upper triple point in the case of zero bias, or along the baseline of the associated triangle for an applied bias to ensure elastic transport, and therefore

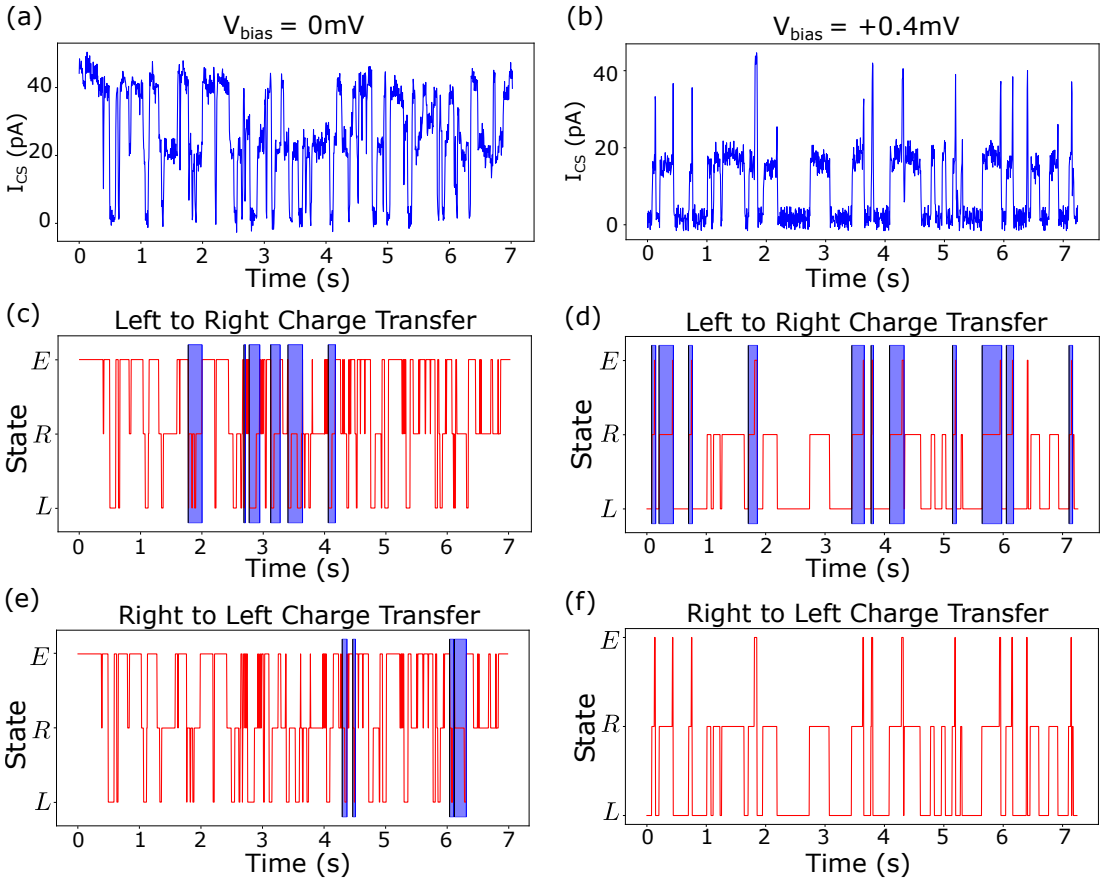

Figure 3.4: Charge sensing time-trace data of charge transitions in a double quantum dot. (a) and (b) show raw charge sensing data for $V_{\text{bias}} = 0$ mV and $V_{\text{bias}} = 0.4$ mV respectively. Each point is measured for an integration time of 5ms. (c)-(f) show the DQD states as a function of time as determine by the Gaussian fit classifier. In this case state, charge state labels map as $L \equiv (N+1, M)$, $R \equiv (N, M+1)$, and $E \equiv (N, M)$. Highlighted regions indicate a sequence of charge states corresponding to (c,d) a charge moving from the left lead to the right lead through the DQD and (e,f) a charge moving from the right lead to the left lead through the DQD.

maximum current. The charge transition in Figure 3.1(b) is at zero bias and a full range of biases is shown in Figure 3.3. The bias triangles observed in charge sensing give information about the energy level structure of the quantum dots and will be discussed later in this chapter.

Example segments of the time-trace data are shown in Figure 3.4. In panel (a) the trace is performed at a triple point with zero applied bias. This trace exhibits random directionality of charge transport, shown by similar numbers of right to left, and left to right charge transfer sequences in (c) and (e). In panel (b) the trace is performed on an elastic transition line of a bias triangle with an applied bias

of $V_{\text{bias}} = 0.4$ mV. In this case there is a preferred sequence of right to left charge transfer events which indicates that the applied bias is driving a current through the dot as expected under typical operation of a DQD device.

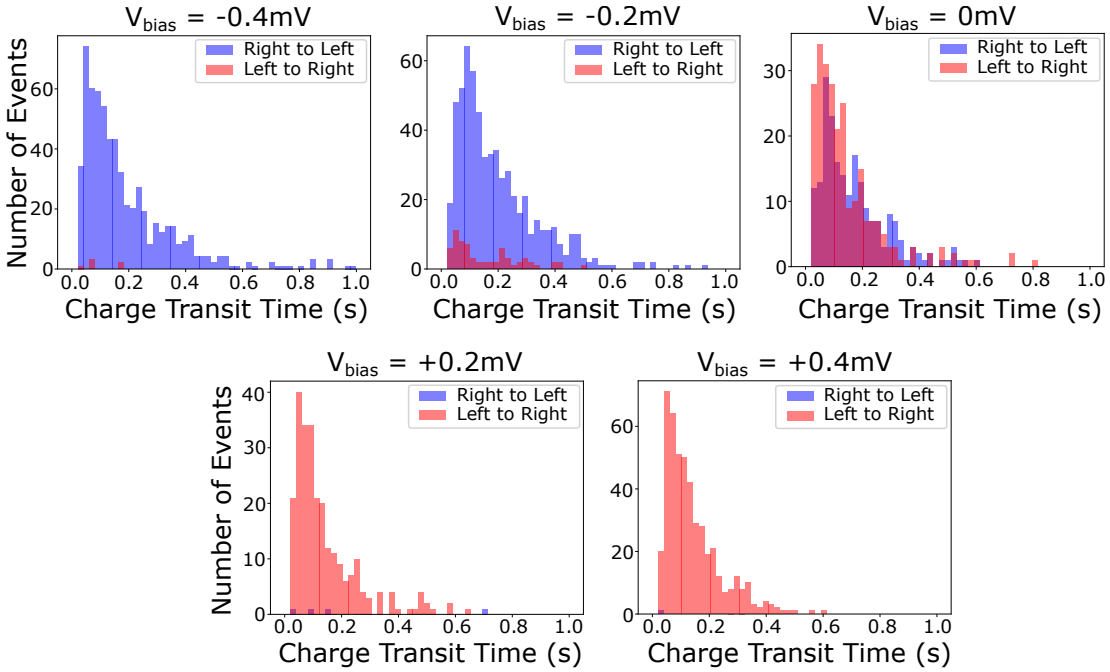

Figure 3.5: Time binned data of the transit time of a charge through the double quantum dot from the left lead to right lead (red) and right lead to left (blue). At negative V_{bias} more charge moves from right to left, and at positive V_{bias} more charge moves from left to right.

As the device is hole based, we expect a positive current as defined in Eq. (3.1) for positive V_{bias} applied to the left lead. We consider the charge transport triple point, so for positive V_{bias} applied to the left lead we expect more charge transfer events to occur from left to right than right to left. This effect can be seen in the time-trace data in Figure 3.4 and the time binned charge transit time data in Figure 3.5. The distributions are approximately equal for $V_{\text{bias}} = 0$ mV, and fitting an exponential function gives a mean transit time of 0.12s from left to right and 0.14s from right to left.

To estimate the current flowing through the double quantum dot, we segment our ≈ 5 minute time-traces into 20 independent time-traces and determine the net transfer of charge based on counting right to left and left to right transitions using our readout classifier for each segment. The mean and standard deviation error of

these values is used to compute the current at the bias under consideration. The estimated current values for $V_{\text{bias}} \in \{-0.4, -0.4, 0.0, +0.2, +0.4\}$ mV are shown in Figure 3.6. The direction of current changes as the bias moves from negative to positive voltages as expected, with values in the sub-attoampere range.

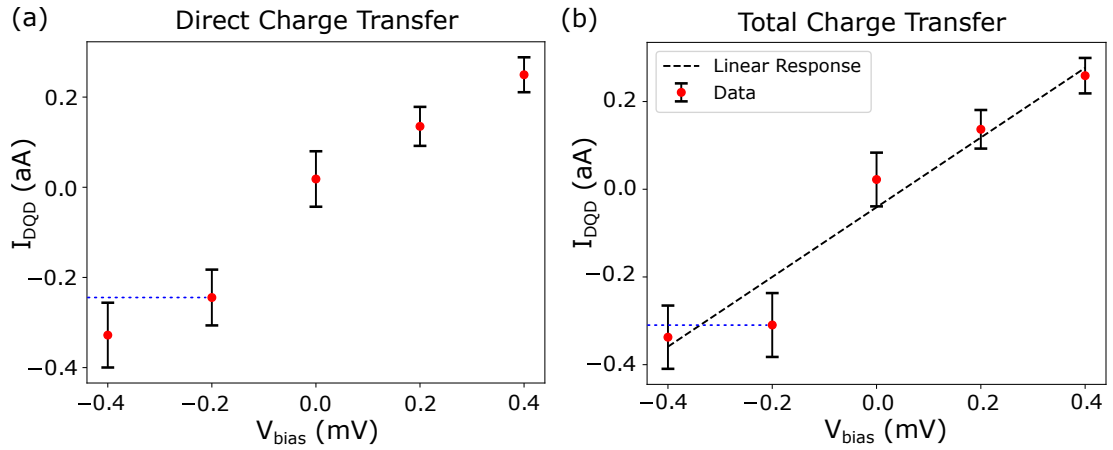

Figure 3.6: Current values with standard deviation uncertainties determined by counting charge transitions through a double quantum dot for a range of applied biases. Each point is the mean of 20 independent estimate from sensor current time-traces of approximately 15s in duration, with a standard deviation error bar. (a) Only direct charge transfer events are considered, and in (b) indirect transport is also included in the counting process (see text for details). A linear response fit is shown in (b), with an estimated resistance of 1.3 ± 0.3PΩ. The blue dashed horizontal line in each plot serves to highlight the primary difference between the two counting processes at $V_{\text{bias}} = -0.2$ mV, where counting indirect charge transitions has the largest effect on the estimated current.

Also shown in Figure 3.6 is a comparison between the case of only considering direct charge transfer events (i.e. the charge always moves sequentially in one direction) and also including indirect charge transfer events (i.e. the charge may move backwards from one dot to the previous before continuing to move through the DQD) up to fourth order. The effect of including these transitions is most notable at a bias of $V_{\text{bias}} = -0.2$ mV, but otherwise results in minor differences in the estimated current. We also perform a linear response fit to estimate the resistance of the double quantum dot. We find a value of $R = 1.3 \pm 0.3$ PΩ, which is a useful metric for the system [57]. In the sequential tunnelling regime, we expect the current to saturate at a value related to the characteristic tunnel rates of the system[1], which will be demonstrated in theoretical analysis of the data in Section 3.5.

[1]Recall the sequential tunnel regime relation: I [A] $\sim 10^{-19}$ Γ [Hz].

3.4 Probing Tunnel Rates by Counting Charge Transitions

Further to detecting current by counting the sequential transitions leading to transport of a charge across the DQD, we can use the same data to estimate tunnel rates. We focus on the interdot tunnel rate t_c, as it is independent of dot electrochemical potentials, unlike tunnelling to and from the leads. Estimating the lead coupling requires sweeping the electrochemical potential of the dots which was not performed during our current detection experiment [108]. In a sequence of transitions where a charge moves from one state to another before returning to the original state, the lifetime in the interim state is related to the tunnel rate between the two charge states by $\lambda = \langle \delta t \rangle^{-1}$. In our case, $[R, L, R]$ means a charge moves from right dot to left dot and back, and $[L, R, L]$ from left dot to right dot and back. We consider the time-trace data at the same range of biases used in section 3.3, with each long time-trace is segmented into 5 independent time-traces to obtain mean and standard deviation errors for the tunnel rate estimates.

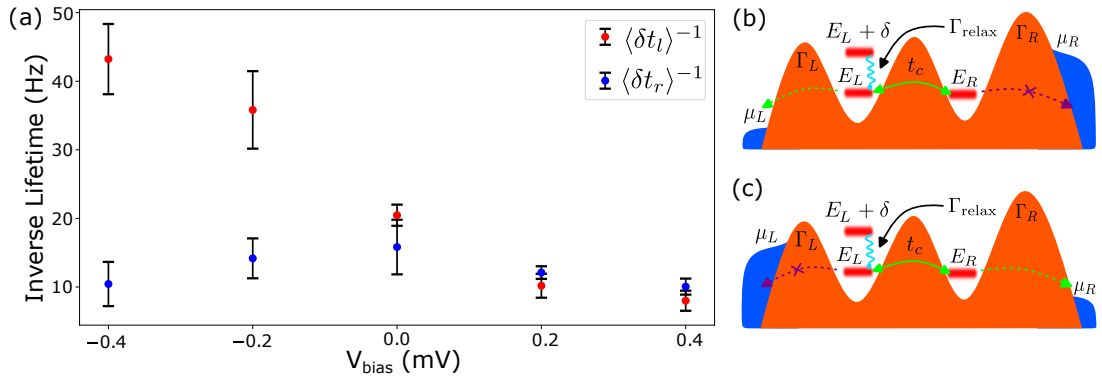

Figure 3.7: (a) Inverse lifetimes of charge states on each dot when counting interdot transitions. The points indicate the inverse mean lifetime on the left dot $\langle \delta t_l \rangle^{-1}$ (red) and right dot $\langle \delta t_r \rangle^{-1}$ (blue) with standard deviation errors for 5 independent time-traces of approximately 1 minute duration. The values used to compute the mean and standard deviation errors at each bias are the mean lifetimes in the relevant dot for each segment. (b) and (c) show the possible directions of travel for a charge from each dot at negative and positive bias, respectively. Dashed lines represent escape events to the leads. Green represents a non-zero tunnel rate, and purple with a cross represents a blocked transition due to the lead occupation. Details of the energy level structure are discussed in the next section.

The inverse mean lifetimes determined by counting transitions are shown in Figure 3.7. The lifetime of the charge state on the right dot is determined using the $[L, R, L]$ sequence, with largely consistent inverse values for each bias. The lifetime of the charge state on the left dot is determined using the $[R, L, R]$ sequence, with a significant difference between negative and positive bias. The disparity in lifetimes on each dot can be explained by asymmetric tunnel rates to the leads, whereby charge tunnels from the left dot to left lead at rate $\overline{W}_{\mathrm{L}}$, faster than from right dot to right lead at rate $\overline{W}_{\mathrm{R}}$. The directional tunnel rates $\overline{W}_{\mathrm{L(R)}}$ are weighted by the empty lead states according to Fermi occupation evaluated at the neighbouring dot electrochemical potential (i.e. $[1 - f_{\mathrm{L(R)}}(E_{\mathrm{L(R)}})]$). At the operation temperature of the device ≈ 100 mK, this means $\overline{W}_{\mathrm{R}}$ is effectively zero at negative bias, and $\overline{W}_{\mathrm{L}}$ is effectively zero at positive bias. A schematic of the possible tunnel rates from each dot is shown in Figure 3.7(b) at negative bias, and (c) at positive bias.

In addition to the asymmetry in lead tunnel rates, if $\overline{W}_{\mathrm{L}} > t_c$, the charge is likely to escape to the left lead before returning to the right dot. This escape of charge will limit the number of long δt_l lifetimes in $[L, R, L]$ sequences and result in an overestimation of $t_c = \langle \delta t_l \rangle^{-1}$. From this analysis, we can use the limited lifetimes on the left dot at negative bias to achieve a rough estimate of the maximum $\overline{W}_{\mathrm{L}}$ (i.e. $f_{\mathrm{L}}(E_{\mathrm{L}}) \approx 0$) of $\Gamma_L \approx 40$ Hz.

Following the same reasoning for positive bias, $\overline{W}_{\mathrm{L}}$ is effectively zero with $\overline{W}_{\mathrm{R}}$ acting as a possible limiter for lifetimes on the right dot. From Figure 3.7, the inverse lifetime on the right dot does not increase at positive bias in the same manner as the left dot at negative bias. We can then infer that $\overline{W}_{\mathrm{R}} < t_c$ as there is no significant change in lifetimes as $f_{\mathrm{R}}(E_{\mathrm{R}})$ decreases. In such a situation, the rate at which charge escapes to the right lead is slow enough to not affect the lifetime on the right dot determined by the interdot tunnel rate. We use the values of $\langle \delta t_l \rangle$ and $\langle \delta t_r \rangle$ at positive bias to estimate the interdot tunnel rate as $t_c = 9.02 \pm 1.68$ Hz.

3.5 Fitting an Open Quantum Systems Model

We develop a model to further our understanding of the estimated current shown in Figures 3.6(b) and compare it with the analysis of tunnel rates discussed in the previous section. We use a quantum master equation of a double quantum dot and include an orbital excited state on the left dot, evidence of which can be seen in Figure 3.3. The Hamiltonian of the model reads,

$$H = H_0 + H_l + H_{el}, \tag{3.2}$$

$$H_0 = \sum_{s=l,r}\sum_{i=1}^{n_s} E_{s_i}|s_i\rangle\langle s_i| + \sum_{i=1}^{n_l}\sum_{j=1}^{n_r} t_{ij}\Big(|l_i\rangle\langle r_j| + H.c.\Big), \tag{3.3}$$

$$H_l = \sum_k (\epsilon_k - \mu_l) d_{kl}^\dagger d_{kl} + (\epsilon_k - \mu_r) d_{kr}^\dagger d_{kr}, \tag{3.4}$$

$$H_{el} = \sum_k \left[\sum_{i=1}^{n_l}(t_{li} d_{kl}^\dagger c_l + H.c.) + \sum_{i=1}^{n_r}(t_{ri} d_{kr}^\dagger c_r + H.c.)\right], \tag{3.5}$$

were E_{s_i} is the energy of each dot state and t_{ij} is the interdot tunnel rate between the states $|l_i\rangle$ and $|r_j\rangle$ on the left and right dot, respectively. We specifically consider $n_l = 2$ and $n_r = 1$, but present the general model below. H_l describes the leads with $\mu_{l(r)}$ being the chemical potential of the left(right) leads, and $d_{kl(r)}^\dagger(d_{kl(r)})$ are the fermionic creation(annihilation) operators for the mode with energy ϵ_k in the left(right) lead. H_{el} describes the coupling between the dots and the leads where $c_{l(r)}$ is the fermionic annihilation operator acting on the left(right) dot, and $t_{l(r)i}$ are the tunnel couplings between the leads and the each dot state. As we are considering elastic transport between the dots, the influence of phonons is neglected.[2]

To model the steady state current flowing through the DQD at a given source-drain bias $V_{\text{bias}} = \mu_l - \mu_r$ we solve a weak-coupling master equation of the form,

$$\dot{\rho} = \mathcal{L}\rho = -i[H_0, \rho] + \mathcal{L}_{\text{leads}}\rho + \mathcal{L}_{\text{relax}}\rho \tag{3.6}$$

where ρ is the density matrix of the DQD system, $\mathcal{L}$ is the Liouvillian superoperator, and $\mathcal{L}_{\text{leads}}$ is the dissipator associated with the leads. $\mathcal{L}_{\text{relax}}$ is a dissipator associated with relaxation of charge in an orbital excited states on a dot relaxing to the ground

[2] At zero detuning, the eigenstates of H_0 have an energy separation of $\omega_p = 2t_c$, but share equal support on the left and right dots, so phonon transitions have no effect on charge transport.

state on the same dot [111]. The lead coupling dissipator can be expressed in the site basis as

$$\begin{aligned}\mathcal{L}_{\text{leads}} = &\sum_{i=1}^{n_l}\Big\{W_{Li}\mathcal{D}[|l_i\rangle\langle 0|] + \overline{W}_{Li}\mathcal{D}[|0\rangle\langle l_i|]\Big\} + \\ &\sum_{j=1}^{n_r}\Big\{W_{Rj}\mathcal{D}[|r_j\rangle\langle 0|] \ + \overline{W}_{Rj}\mathcal{D}[|0\rangle\langle r_j|]\Big\},\end{aligned} \tag{3.7}$$

where the Lindblad superoperators act according to $\mathcal{D}[A]\rho = A\rho A^\dagger - 1/2\{A^\dagger A, \rho\}$. The tunneling rates from a lead onto the dot are given by $W_{L(R)j} = \Gamma_{L(R)} f_{L(R)}(\epsilon_j)$ and from the dot onto the lead $\overline{W}_{L(R)j} = \Gamma_{L(R)}\Big[1 - f_{L(R)}(\epsilon_j)\Big]$ with $\Gamma_{L(R)} = \pi g_{L(R)}|t_{L(R)}|^2$, where $g_{L(R)}$ is the constant density of states in the leads in the wide band approximation, and $f_{L(R)}(\epsilon) = [e^{(\epsilon-\mu_{L(R)})/k_BT} + 1]^{-1}$ is the Fermi-Dirac distribution for the source(drain) lead. The process of charge in excited states relaxing to the ground state is described by the dissipator,

$$\mathcal{L}_{\text{relax}} = \Gamma_{\text{relax}}\Big(\sum_{i=1}^{n_l}\mathcal{D}[|l_0\rangle\langle l_i|] + \sum_{j=1}^{n_r}\mathcal{D}[|r_0\rangle\langle r_j|]\Big). \tag{3.8}$$

The choice of relaxation rate, Γ_{relax} is somewhat arbitrary without a microscopic derivation of the energy emission process (e.g. to a phonon bath), but having $\Gamma_{\text{relax}} \geq t_c$ typically explains double quantum dot transport data. A value of order 10 MHz has been estimated for a Si/SiGe electrostatically defined DQD [111], which is much faster than the tunnel rates considered in this chapter; we use this value in our model. This relationship between inter-dot tunnelling and relaxation rates suggests that transport between excited states from one dot to another does not typically occur.

Denoting the electronic charge as e, and ρ_{ss} the steady state solution of Eq. (3.6), the steady state current flowing though the DQD from left to right is

$$I = e\sum_{j=1}^{n_r}\overline{W}_R\text{Tr}(\rho_{\text{ss}}|r_j\rangle\langle r_j|) - W_R\text{Tr}(\rho_{\text{ss}}|0\rangle\langle 0|). \tag{3.9}$$

With this model to hand and the bias triangles displayed in Figure 3.3, we can quantitatively fit the current values in Figure 3.6(b). We can discern the location of the excited state by considering the detuning axis of the bias triangles in Figure 3.3 which shows an excited state in the $V_{\text{bias}} = -0.4$ mV transition, but not

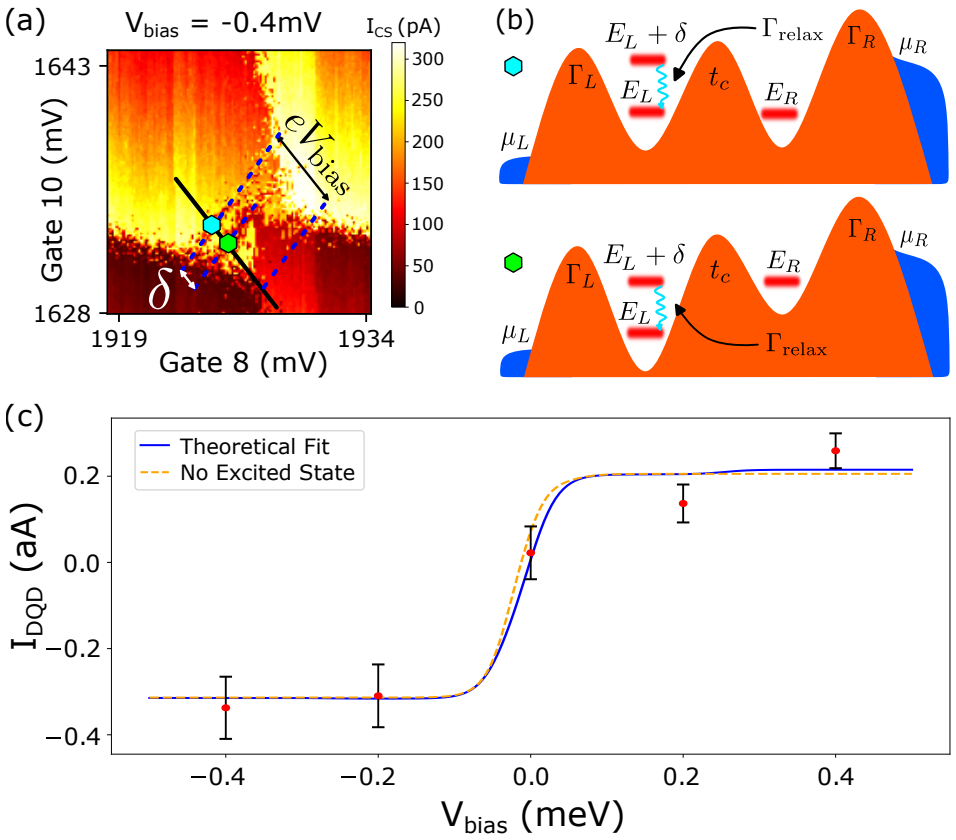

Figure 3.8: Details of the theoretical fit to the DQD current estimated from charge sensor time-trace measurements. (a) Charge transitions at $V_{\text{bias}} = -0.4$ mV showing an exited state. The lines indicate the energy scale of the triangle and difference between ground and excited state energy levels in the left dot. (b) Schematic of the model under consideration where the energies refer to the electrochemical potentials of the relevant charge states. Each schematic relates to the state of the dot energy levels at the associated coloured markers in (a). (c) The solid blue line displays a fit of the model. The fitted parameters are $\Gamma_L^* = 12.4$ Hz and $\Gamma_R^* = 2.86$ Hz. Other parameters are set to $t_c = 9.02$ Hz, $\Gamma_{\text{relax}} = 10$ MHz, and $T = 100$ mK. For comparison, the dashed orange line displays a fit using the same fitted parameter values, but with no excited state in the model.

the $V_{\text{bias}} = +0.4$ mV transition. As the bias voltage is applied to the left lead we can infer that there is an orbital excited state in the left dot. The charge transition at $V_{\text{bias}} = -0.4$ mV is shown again in Figure 3.8(a) with a schematic in panel (b) which shows the energy level arrangement to explain the data. Using the extent of the triangle as an energy scale, we set the excited state in the left dot to have an energy of $\delta = 0.13$eV above the ground state.

The fit of this model to the current values obtained in the previous section is shown in Figure 3.8(c), with fitted parameters of $\Gamma_L^* = 12.4$ Hz and $\Gamma_R^* = 2.86$ Hz,

and least squares uncertainties of 4.6Hz $< \Gamma_L^* <$ 75.2 Hz and 2.05 Hz $< \Gamma_R^* <$ 3.69 Hz. We set $\Gamma_{\text{relax}} = 10$MHz and $t_c = 9.02$ Hz as estimated in the previous section without fitting further as these parameters do not influence the rate of elastic transport at zero detuning, and $T = 100$ mK which reflects the operating temperature of the dilution refrigerator in which the measurements were taken. As expected from the analysis in the previous section, $\Gamma_{\text{L}} > t_c > \Gamma_{\text{R}}$, with the confidence intervals of Γ_{L} containing the estimate of $\overline{W}_{\text{L}} = \Gamma_{\text{L}} \approx 40$ Hz.

3.6 Phonon Assisted Transitions

With the ability to detect individual charge transitions, we can also investigate evidence of the phonon induced transitions discussed in the previous chapter. Full discussion of all the relevant terms can be found in Section 2.5, but we state the dissipator equation describing phonon interaction with a DQD for completeness,

$$\mathcal{L}_{\text{phonons}} = \gamma(\omega_p)\Big([n(\omega_p)+1]\mathcal{D}[|-\rangle\langle+|]\rho(t) + n(\omega_p)\mathcal{D}[|+\rangle\langle-|]\rho(t)\Big). \tag{3.10}$$

Here, $\gamma(\omega)$ is the energy dependent transition rate associated with the phonon bath spectral density, $|+\rangle$ and $|-\rangle$ are eigenstates of H_0, $\omega_p = \sqrt{\epsilon^2 + 4t_c^2}$ is the eigenstate energy splitting, and $n(\omega_p) = [e^{-\beta\omega_p} - 1]^{-1}$ is the Bose-Einstein occupation of the phonon bath. This dissipator only considers a single state in each dot, but a more general dissipator of this form can be inserted into Eq. (3.6) to model the current through the DQD with an excited state.[3] We qualitatively discuss the effect of phonons on charge transport in this section.

By performing a series of time-traces along the detuning axis of a bias triangle, transitions observed at large detuning and therefore far from the elastic transport regime would constitute evidence of phonon assisted transport. The asymmetry about zero detuning is explained by the phonon emission and absorption rates in Eq. (2.78) being weighted by the Bose-Einstein occupation of the phonon bath. For low temperatures (≈ 100 mK) and the meV energy scales under consideration

[3]Following from the discussion in Section 3.5 of $\Gamma_{\text{relax}} \geq t_c$ being a suitable choice, we can expect that the dominant source of phonon induced transitions will be between ground states on each dot, even when allowing for other transitions.

in the DQD, we find that $n(\omega_p) \ll 1$ and so emission processes dominate. With a positive bias applied to the left lead, we only expect phonon assisted transport in the positive detuning region where the electrochemical potential of the left dot is higher than that of the right dot. The opposite is expected for the equivalent negative bias on the left lead.

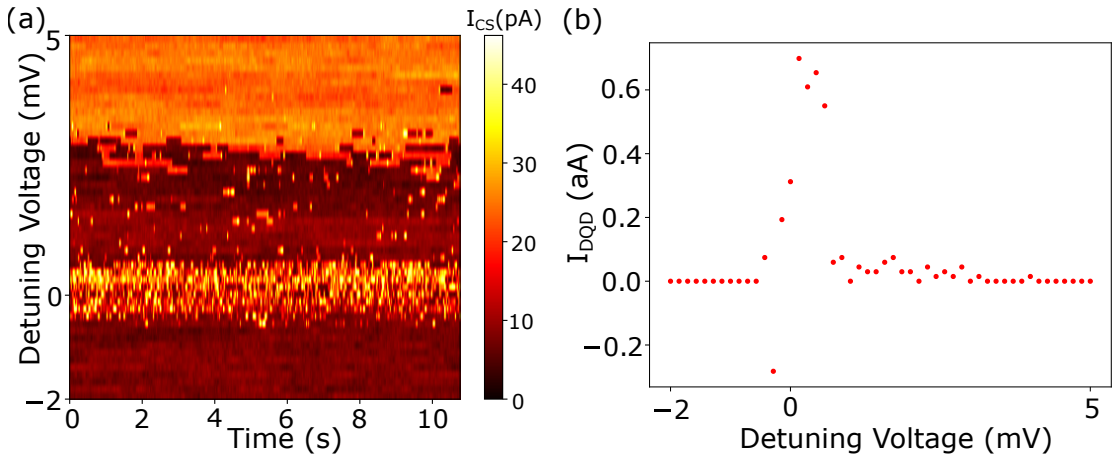

Figure 3.9: Exploring charge transport in the inelastic transport regime. (a) Charge sensing data for a sweep of a detuning axis voltage (a linear combination of Gates 8 and 10) with a time-trace performed at each voltage. (b) The current estimated at each voltage by counting the transfer of charge by transitions in the charge sensing data in (a). There is a notable outlier just below the zero detuning voltage.

To search for the effect of phonon assisted transport we choose a bias triangle at $V_{\text{bias}} = +0.4$ mV (such as shown in Figure 3.3) as there is no visible excited state. We define a linear combination of Gate 8 and Gate 10 such that it follows the detuning axis of the triangle, with the point of zero detuning voltage is chosen to be at the centre of the peak in signal associated with the base of the bias triangle. At each detuning voltage, we perform a time-trace with the charge sensor data shown in Figure 3.9(a). There appears to be noise in the signal in the positive detuning region, but performing the charge transition analysis presented above we find that there are charge transport events occurring in this region. The current estimated from this transition counting analysis is shown in panel (b) with a clear, albeit noisy, signal across the extent of the triangle. By the nature of the Lindblad operators in Eq. (2.78) and Eq. (3.10) it follows that we observe inelastic charge transport events which emit single phonons into the Si/SiGe lattice. There is one

outlier point, which may be a result of statistical noise in the time-trace. Due to a switch event occurring in the device, the measurements taken in Figure 3.9 were taken at different device voltages to those presented earlier in this chapter, but the detected current remains in the sub-attoampere regime.

The duration of our time-trace measurements along the detuning axis, and hence the signal to noise ratio in the estimated current values, is limited by the occurrence of switch events in the device. Our measurements are the first of this kind to be taken in a Ge/SiGe device, but a detailed study of these phonon induced transitions in a GaAs device in the slow tunnel rate regime has been performed in Ref. [112]. Our data is insufficient to achieve a theoretical fit providing meaningful insight into the parameters, however the weak-coupling model of phonon induced transitions discussed in Section 2.5 is particularly relevant. As GaAs is piezoelectric and Ge/SiGe is not, a comparison of theoretical fits should find different phonon spectral densities as discussed in Section 2.4. With significantly longer time-trace data at each detuning voltage, a better estimate of current could be achieved and facilitate a theoretical fit of the data leading to such a comparison.

3.7 Discussion

In this chapter we have considered the counting of charge transitions through a double quantum dot in a Ge/SiGe heterostructure device. We have fitted a classifier to determine DQD charge states from charge sensing data taken at a DQD charge transition. This classifier is used to search for sequences of transitions in time-trace measurements which indicate that a charge has moved from one lead to the other by traversing the double quantum dot. By counting the occurrences of these sequences in each direction, we estimate current through the DQD to be in the attoampere regime at several bias voltages. With the same time-trace data, we estimate the interdot tunnel coupling via transition lifetimes on each dot. The estimation of the interdot tunnel rate displays evidence of an asymmetry in the lead tunnel rates which is confirmed by a theoretical fit of a quantum master equation model to the estimated current values. The estimated tunnel rates are found to be in the Hertz

regime, consistent with the sub-attoampere current estimation. We also investigate the current along the detuning axis of a bias triangle and find clear signals of inelastic charge transport mediated by phonons. This has been a demonstration of this phonon interaction, and future work including longer time-trace measurements along the detuning axis could facilitate the first experimental characterisation of the phonon spectral density for a DQD in a Ge/SiGe device.

4

Machine Learning Accelerated Electrostatic Simulation

The electrostatic model of the device presented in this chapter was developed by the author using methods from the literature. The author worked jointly with Hyungil Moon to determine the transport path and number of quantum dots. The author performed all aspects of deep learning acceleration, including designing model architectures, generating training data, and training models.

This chapter considers a machine learning accelerated model of the electrostatic potential in a gate defined quantum dot device in a 2D heterostructure, and consider applications to developing a virtual device. An electrostatic model facilitates the investigation of how different gate voltages for a particular device design may impact the transport regime. We focus on a GaAs device using the heterostructure dimensions outlined in Figure 1.4(a) as it shall be considered in experimental results in the next chapter for an investigation of how electrostatic disorder impacts transport. The geometry of this device is shown in Figure 4.1. We present methods of identifying the transport regime of the device, namely whether the transport channel from source to drain is open or closed, and the formation of quantum dots. In order to improve the speed at which transport regimes can be identified, we train deep learning models using simulated data generated by the electrostatic

model. The speed of computation using such deep learning models with GPU hardware allows for large numbers of simulations to be generated quickly. A fast model provides a path towards building a useful virtual quantum dot device which can be used by humans or algorithms for tasks such as characterisation, control, or inference of quantum device properties.

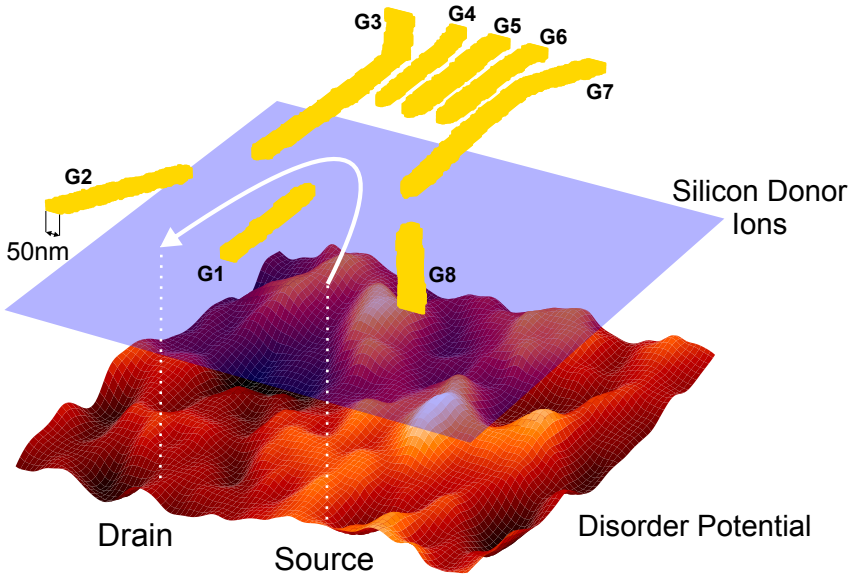

Figure 4.1: Gate design of the GaAs device considered in this chapter. The location of a delta-doping layer of Si donors is shown as a blue plane, and an example of a disorder potential is shown with the direction of current indicated by arrows.

4.1 Electrostatic Model

In the GaAs heterostructure under consideration there is a disorder potential induced by randomly located silicon donor ions as depicted in Figure 4.1, in addition to the potential induced by voltages applied to gate electrodes. The effects of gate electrodes and donor ions on the electrostatic potential in the plane of the two-dimensional electron gas (2DEG) are calculated using a self consistent method developed by Nixon et al. [113]. The vector from the origin to a point in 3-dimensional space is denoted as $\mathbf{R} = (\mathbf{r}, z)$, where $\mathbf{r}$ is a vector in the x-y plane with the surface of the device defined as z=0. The total electrostatic potential

$\phi_{\text{tot}}(\mathbf{r})$ is considered as the sum of components

$$\phi_{\text{tot}}(\mathbf{r}) = \phi_{\text{g}}(\mathbf{r}) + \phi_{\text{d}}(\mathbf{r}) + \phi_{\text{s}}(\mathbf{r}) + \phi_{\text{e}}(\mathbf{r}), \tag{4.1}$$

where $\phi_{\text{g}}(\mathbf{r})$ is the contribution from the gate electrodes, $\phi_{\text{d}}(\mathbf{r})$ is the contribution from the randomly located donor ions, $\phi_{\text{s}}(\mathbf{r})$ is a constant contribution from surface states, and $\phi_{\text{e}}(\mathbf{r})$ is the electrostatic potential caused by the presence of electrons in the 2DEG. The electrostatic potential energy of an electron at location $\mathbf{r}$ is

$$U(\mathbf{r}) = -e\phi_{\text{tot}}(\mathbf{r}). \tag{4.2}$$

The gate electrodes exist on the surface of the device and the potential from each gate at a depth $d = 115$ nm beneath the gates in the plane of the 2DEG is determined using analytic expressions [114]. Using zero potential boundary conditions, we consider the total potential from all the gates to be equal to the sum of gate potentials weighted by the voltage applied to each gate. The surface potential is determined by the Schottky barrier with the gates, as discussed by Ref. [115], and is set to a constant value of $\phi_{\text{s}} = -800$ mV.

The delta-doped heterostructure allows the donor ions to be treated as existing in a plane at a constant height $h = 45$ nm above the 2DEG. The contribution to the electrostatic potential at the 2DEG from a single donor ion at location $\mathbf{r}_{ij}$ in the donor plane is,

$$\phi_{\text{d}}(\mathbf{r}, \mathbf{r}_{ij}) = \frac{e}{4\pi\epsilon\epsilon_0}\left[\left(|\mathbf{r} - \mathbf{r}_{ij}|^2 + h^2\right)^{-1/2} - \left(|\mathbf{r} - \mathbf{r}_{ij}|^2 + (2d - h)^2\right)^{-1/2}\right] \tag{4.3}$$

where the second Coulomb term is required to satisfy the zero potential boundary condition on the surface. The total contribution from the donor ions is then $\phi_{\text{d}}(\mathbf{r}) = \sum_{ij} \phi_{\text{d}}(\mathbf{r}, \mathbf{r}_{ij})$, summing over the locations of each donor ion.

The electron number density is calculated using the Thomas-Fermi approximation in 2D

$$n(\mathbf{r}) = 2\frac{m^*}{\pi\hbar^2}\big(\mu_F - U(\mathbf{r})\big), \Theta\big(\mu_F - U(\mathbf{r})\big) \tag{4.4}$$

where m^* is the effective mass of an electron in GaAs, μ_F is the chemical potential or Fermi level of the 2DEG which is set to zero, and $\Theta(\cdot)$ is the Heaviside step

function. The factor of 2 accounts for spin degeneracy, and the Heaviside step function approximates the Fermi distribution at low temperatures. The electrostatic potential associated with the electron density is

$$\phi_{\mathrm{e}}(\mathbf{r}) = -\frac{e}{4\pi\epsilon\epsilon_0}\int \mathbf{dr}'\frac{n(\mathbf{r}')}{|\mathbf{r}-\mathbf{r}'|}. \tag{4.5}$$

The electron density contributes to the total electrostatic potential ϕ_{tot} but the electron density also depends on ϕ_{tot}. This requires a self-consistent solution which is achieved using an iterative under-relaxation process until convergence.

The density of donor ions in the donor plane is determined by matching the mean self-consistent electron density with zero gate voltages applied, to the experimentally measured electron density in the 2DEG. The donor density is taken as $\sigma = 1.25\times 10^{16}$ m^{-2} giving a calculated mean electron density of $\langle n(\mathbf{r})\rangle = (2.64 \pm 0.04)\times 10^{15}$ m^{-2}, which is the mean and standard deviation uncertainty of 100 repeated calculations with different disorder potentials. This value is in agreement with the experimental value of 2.64×10^{15} m^{-2}.

A scale factor is required to match the model results to experimental observations. The model underestimates the gate voltages required to deplete the 2DEG by approximately a factor of 4. This scale factor is somewhat inelegant and can be attributed to the zero-potential boundary conditions, but the quantity of interest is the relative strength of gate voltages for a particular device configuration rather than the absolute values. The model produces results which are in good qualitative agreement with experiment [116], providing grounds to pursue its explanatory power for understanding device characteristics.

4.2 Modelling the Transport Channel

Experimental current measurements rely on the transport of electrons from source to drain. As larger negative voltages are applied on the surface gates, the electrostatic energy U of regions in the 2DEG will exceed the Fermi level μ_F to deplete the electron density to zero. Given $\mu_F = 0$ (in any unit of energy), regions where $U(\mathbf{r}) < 0$ can be identified as having zero electron density using Eq. (4.4). If

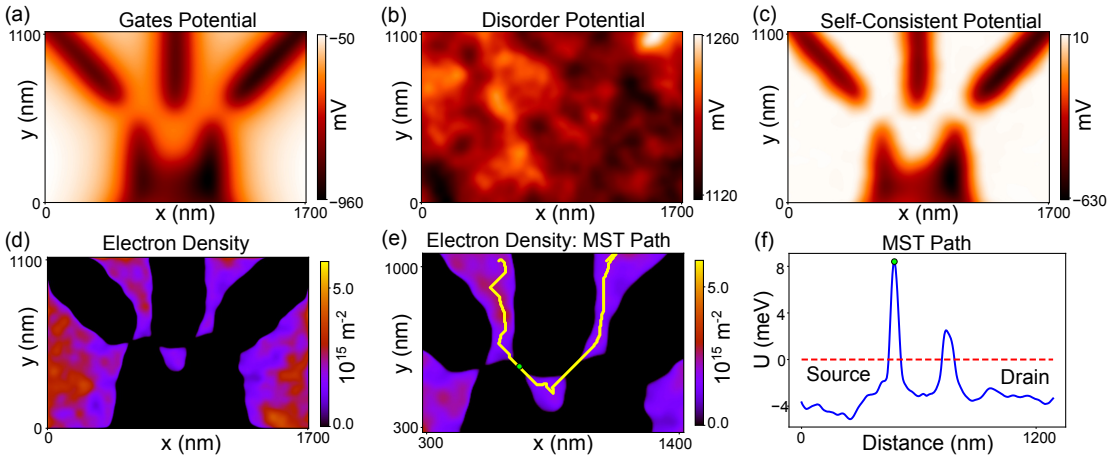

Figure 4.2: An example of the device model. Spatial coordinates x and y are used to indicate the scale of the device. (a) Electrostatic potential from the gate electrodes ϕ_{g}, (b) a disorder potential ϕ_{d}, and (c) self-consistent potential ϕ_{tot} given the potentials in (a) and (b). (d) The electron density in the 2DEG given the potential in (c), which shows a single dot. (e) Example of MST path from source to drain in 2D (yellow line) with the location of U^* is marked by a green circle. (f) The potential energy, U, corresponding to the MST path in (e) with U^* marked by a green circle. The horizontal axis indicates the total distance moved in 2D space. The channel is closed since the value of U^* is above the Fermi level indicated by the red dashed line.

there is no path between source and drain without the electron density being fully depleted, current stops and pinch-off occurs.

A semi-classical trajectory of electrons between source and drain regions is calculated by formulating an image of the potential as a graph G_ϕ, where each pixel is a node. G_ϕ is defined as

$$\begin{aligned} G_\phi = \Big(V, E\Big) \ , \ V = \{v_i\} \ , \ E = \{e_{ij}\} \ , \\ v_i = U(\mathbf{r}_i) \ , \ e_{ij} = \frac{1}{2}\Big[v_i + v_j\Big] \ , \end{aligned} \tag{4.6}$$

where V is the set of nodes in G_ϕ with v_i being the value of the i^{th} node, and E is the set of edges in G_ϕ with e_{ij} the edge connecting v_i and nearest neighbour v_j.

Given this graph formulation of the potential profile, we compute the minimum spanning tree (MST) of G_ϕ before using the Dijkstra algorithm [117] to find the path from source to drain. This path can be treated as a semi-classical trajectory of an electron. The MST of a graph is a subset of its edges which connects every node in the graph with the minimum sum of edge weights [118]. The unique path between any two nodes in the MST will then have the minimum sum of edge

weights. In the case of G_ϕ the edge weights are the mean of the node values, so the shortest path through its MST will have the minimum possible maximum of potential energy values. This point will be called the minimax point located at $\mathbf{r}_* = (x_*, y_*)$, with $U^* \equiv U(\mathbf{r}_*)$. If U^* is greater than or equal to the Fermi energy μ_F, the model transport channel is considered closed. A comparison of the paths computed using the full graph and the MST are shown in Figure 4.3, which indicates that using the full graph overestimates the value of U^*.

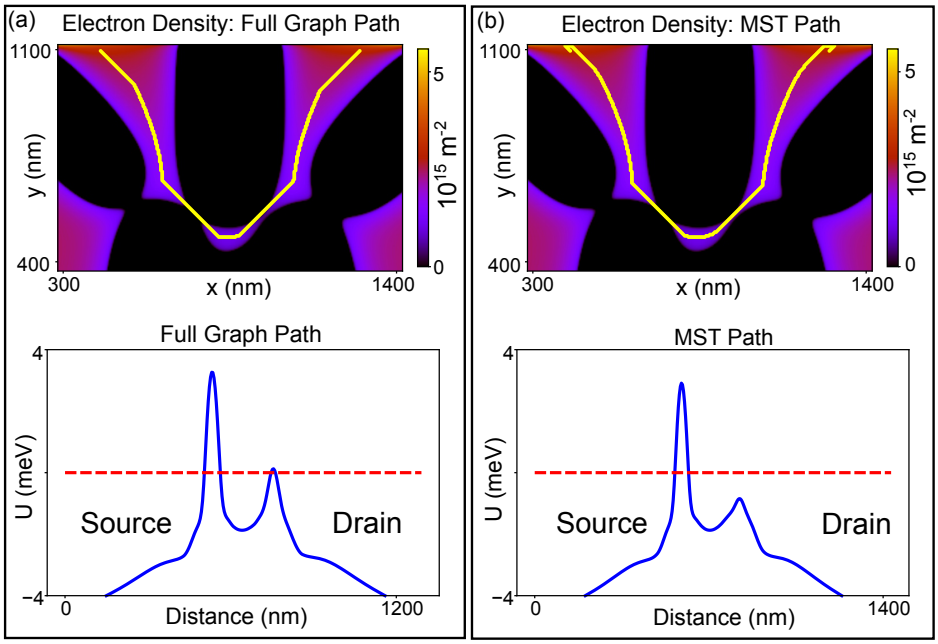

Figure 4.3: Comparison of the semi-classical electron trajectory for (a) the full graph G_ϕ and (b) the MST of G_ϕ at identical gate voltages. The electron density with the relevant transport path (yellow line) is shown in the upper plot of each panel. The potential along each path (blue line) is shown in the lower plot of each panel, where the Fermi energy, μ_F, is indicated by a red dashed line. The 'Distance' axis indicates the total distance moved in 2D space. The transport path using the full graph overestimates the potential barrier height as it shows two regions where $U > \mu_F$. The electron density demonstrates that there is only one region where $U > \mu_F$, matching the prediction of the MST path.

4.3 Dot Identification

The electron trajectory approximated by the MST path can also be used to determine the number of quantum dots formed by a given ϕ_{tot}. The number of dots defined in the device can be determined using regions of the 1D MST path where $U(\mathbf{r}) < \mu_F$

which are delimited by barriers with $U(\mathbf{r}) \geq \mu_F$. An example of the electron density and path corresponding to a single dot in our model is shown in Figure 4.2(d-f). Since dots in our device are 2-dimensional objects in the plane of the 2DEG, the 1-dimensional MST path from source to drain is not sufficient to fully determine the number of dots. Additional paths through the MST are calculated to ensure dot labels are robust to all possible configurations of the electron density. This method was developed for a particular device and while generally applicable, it is not best suited to large numbers of dots due to the computation of the extra paths for each dot. Transport features corresponding to quantum dots can only be observed near the closed channel boundary due to tunnel barriers typically suppressing current far beyond this boundary. The dots identified using our model are not affected by this limitation.

4.4 Machine Learning Acceleration

In this section we discuss how deep learning models can be used to accelerate the model presented in the previous sections. The motivation for this acceleration is the construction of a virtual device which can be used as part of other algorithms, such as the inference of disorder potentials discussed in Chapter 5. The architecture we choose for deep learning is that of a deep convolutional neural network (CNN). The primary reason for this choice is that our input data is a 2D image of an electrostatic potential and the output is either another 2D image or a vector of values associated with a device property. CNNs are specifically designed for such data [119]. They are a type of feed-forward neural network (i.e. information flows forwards through the network from input to output) in which each layer passes information to the next by the action of a set of convolutional filters and a non-linear activation function. If the output is the same dimension as the input we call it a fully-convolutional CNN, and if compression is required for a vector output the last convolution layer will feed into a multi-layer perceptron. A schematic of a CNN is shown in Figure 4.4.

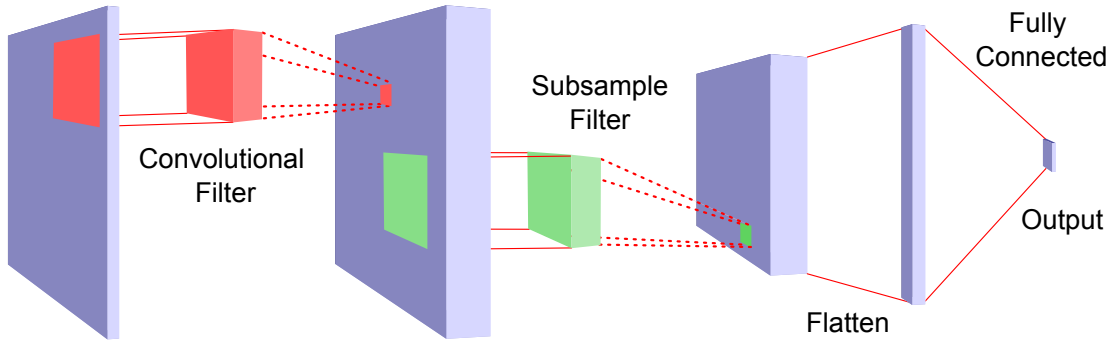

Figure 4.4: A schematic of a CNN. A set of convolutional filters act on the input layer to produce a set of intermediate layers. The filter parameters are learned during training. A non-linear activation function may also act on the filter outputs. This set is then acted on by a subsampling filter (e.g. max pooling which passes the maximum value to the next layer) to reduce the dimensionality. The next set of layers is flattened for input into a fully connected neural network which outputs a single value in the case of regression; a vector may be desired for classification.

4.4.1 Regression for Minimax Estimation

A CNN is trained to calculate $\phi_{\text{tot}}(\mathbf{r}_*)$. Each input is a 2D potential capturing the influence of the gates, disorder, and Schottky barrier, $\phi_{\text{in}} = \phi_{\text{g}} + \phi_{\text{d}} + \phi_{\text{s}}$ where ϕ_{g} and ϕ_{d} are randomly generated and ϕ_{s} remains constant. The output training data consists of the self-consistent potential ϕ_{tot} and $\phi_{\text{tot}}(\mathbf{r}_*)$ corresponding to each input, with $U^* = -\phi_{\text{tot}}(\mathbf{r}_*)$ in units of electron volts. The complete mapping, expressed as $\phi_{\text{in}} \to \phi_{\text{tot}} \to \phi_{\text{tot}}(\mathbf{r}_*)$, is approximated by the CNN $\mathcal{F}_U$. The resolution of ϕ_{in} and ϕ_{tot} is reduced from that used in the electrostatic model to improve the performance of $\mathcal{F}_U$. A series of resolution preserving convolutions in a residual neural network (ResNet) architecture [120] learn the non-linear transformation $\phi_{\text{in}} \to \phi_{\text{tot}}$ and further layers learn the mapping $\phi_{\text{tot}} \to \phi_{\text{tot}}(\mathbf{r}_*)$. A recurrent CNN [121] could have been trained to generate the iterative solution, however we only require the self-consistent potential and not intermediate potentials. The ResNet skip-connections used in $\mathcal{F}_U$, as shown in Figure 4.5(b), share a similar structure to the iterative method used to solve the self-consistent potential.

The training data set contains $85,000$ entries with each input being a potential profile $\phi_{\text{in}} = \phi_{\text{g}} + \phi_{\text{d}} + \phi_{\text{s}}$ where ϕ_{g} and ϕ_{d} are randomly generated. The output training data consists of the self-consistent potential ϕ_{tot} and $\phi_{\text{tot}}(\mathbf{r}_*)$ with $U^* =$

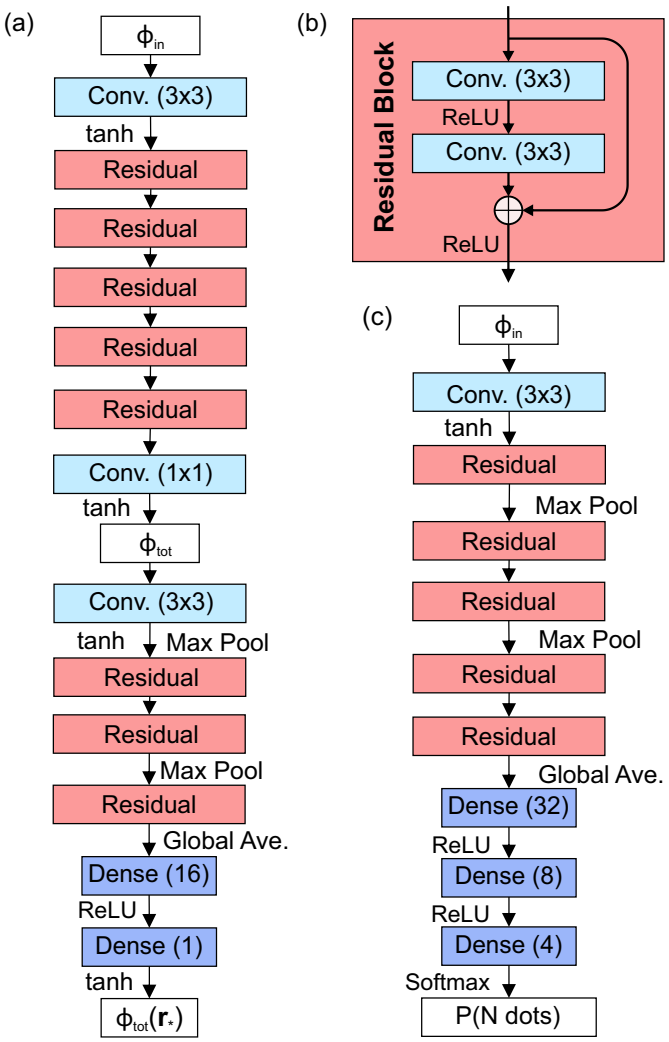

Figure 4.5: The neural networks used to compute U^* and classify dots. Text to the left and right of the arrows indicates the activation function applied and dimension reduction processes respectively. (a) Structure of $\mathcal{F}_U$ beginning with the 2D normalised input potential ϕ_{in}, to the self-consistent potential ϕ_{tot}, and finally to the minimax value $\phi_{\text{tot}}(\mathbf{r}_*)$. All convolutional units have 32 channels. (b) Schematic of a residual block as used in $\mathcal{F}_U$ and $\mathcal{F}_D$. The number of channels is preserved through a residual block. (c) Structure of $\mathcal{F}_D$ beginning with the normalised input potential, with a probability distribution for the number of dots as the output. All convolutional units have 64 channels, and dots are classified using one-hot encoding for $\{0, 1, 2, 3\}$ dot classes.

$-\phi_{\text{tot}}(\mathbf{r}_*)$. The resolution of each input is reduced from the high resolution required to accurately compute the training data, as shown in Table 4.1. Training is performed for 100 epochs using the mean squared error (MSE) loss on both outputs with a learning rate of 1×10^{-3} (dropping to 2.5×10^{-4} in two steps).

Test results achieve a mean absolute error (MAE) of 1.27 meV in U^* estimations,

with a 1.2% error when classifying the transport regime using U^*, with a comparison with the ground truth in Figure 4.6(a). Batching inputs and using a GPU (GTX 1080 Ti) gives a computation time of 0.6ms for a single U^* using $\mathcal{F}_U$, a speed up of order 10^4 over the electrostatic model and path finding algorithm. This evaluation of U^* is also significantly faster than measurement of current. The parallel computation of CNN outputs surpass any acceleration which could be achieved by optimising the exact computation of transport channel and dot number as discussed in sections 4.2 and 4.3, which cannot be easily parallelised, with the added benefit that CNN computation in TensorFlow is differentiable.[1]

ϕ_{in} Resolution Fraction	$\frac{1}{2}$	$\frac{1}{4}$	$\frac{1}{6}$	$\frac{1}{8}$
Time per Training Epoch (s)	430	130	69	65
Time per Output (ms)	1.66	0.46	0.24	0.18
$\phi_{\text{tot}}(\mathbf{r}_*)$: Test MAE (mV)	1.41	1.18	1.25	1.27
Transport Channel : Test Error (%)	1.57	1.23	0.96	1.20

Table 4.1: Performance metrics of $\mathcal{F}_U$ for different resolutions of ϕ_{in}, computed using a GPU (GTX 1080 Ti). Max-pooling processes are adapted for each resolution, otherwise the networks are identical. The resolution reduction fraction is applied to both input dimensions. Full resolution $(269, 411)$ is only required for computing training data, so not considered. Time per output is from a batch of 1000 inputs. MAE is chosen so that units remain in mV, and transport channel error is based on binary classification using the value of $\phi_{\text{tot}}(\mathbf{r}_*)$ produced by $\mathcal{F}_U$.

4.4.2 Classification for Dot Counting

A fast method of counting dots is required to make predictions of voltage settings which form quantum dots, as shall be discussed in the next chapter. A second CNN is trained to approximate the number of quantum dots at a given set of gate voltages. The input is ϕ_{in}, defined above for $\mathcal{F}_U$, with the output being the number of dots, $N_{\text{dot}} \in \{0, 1, 2, 3\}$. The network learns the mapping $\mathcal{F}_D : \phi_{\text{in}} \to P(N_{\text{dot}})$, where $P(N_{\text{dot}})$ is the probability for a given N_{dot} and classification is determined by the maximum $P(N_{\text{dot}})$. Due to the sparsity of dots in gate voltage space, the

[1] Differentiable models facilitate the use of gradient based optimisation algorithms and sampling methods (e.g. Hamiltonian Monte Carlo sampling).

training set used for $\mathcal{F}_U$ is such that the classifier cannot accurately determine N_{dot}, but only the presence or absence of dots. We thus use an intermediate classifier which produces a new training set that ideally only includes gate voltages for which $N_{\text{dot}} > 0$. A mixture of selected (dot-abundant) data and the original (dot-sparse) data is used to train $\mathcal{F}_D$. Using a GPU with batched inputs, the computation time for a single classification with $\mathcal{F}_D$ is 0.6 ms.

The structure of the dot classifier CNN is shown in Figure 4.5(c). The network learns the mapping $\mathcal{F}_D : \phi_{\text{in}} \to P(N_{\text{dot}})$ for $N_{\text{dot}} \in \{0, 1, 2, 3\}$, where classification is taken as the maximum value of $P(N_{\text{dot}})$. An intermediate classifier is used to generate a suitable dataset, as discussed above. Training is performed for 100 epochs using the categorical cross entropy loss function with a learning rate of 1×10^{-3} dropping to 5×10^{-4} after 70 epochs. Test results for dot classification have an accuracy of 98.0% on random data (dot-sparse) and 75.9% on selected (dot-abundant) data. The confusion matrix for the dot-abundant test data is shown in Figure 4.6(b). When determining the maximum number of dots in the direction of a random unit vector of gates voltages, $\mathcal{F}_D$ achieves 95.8% classification accuracy.

Following the notation used in Table 4.1, $\mathcal{F}_U$ and $\mathcal{F}_D$ use $\frac{1}{8}$ and $\frac{1}{6}$ resolution of ϕ_{in} respectively. The computation time for both networks $\mathcal{F}_U$ and $\mathcal{F}_D$ is approximately 0.2 ms given a 2D potential input and using a GPU. However, processing a vector of gate voltages into a 2D potential increases this time to 0.6 ms. The processing involves determining the total gate potential, and summing this with the disorder potential.

4.4.3 Regression for Self Consistent Potential

As a further consideration, a fully convolutional CNN $\mathcal{F}_\phi$ is used to approximate the transformation of $\phi_{\text{in}} \to \phi_{\text{tot}}$. This network shares the architecture of the first section of $\mathcal{F}_{\text{U}}$ but is trained independently to minimise losses due to ϕ_{tot} only being an intermediate output of $\mathcal{F}_{\text{U}}$ and thus the total loss is not optimal. Training is performed for 100 epochs using the MSE loss function with a learning rate of 1×10^{-3} dropping to 2.5×10^{-4} after 70 epochs. Test results achieve a MAE of 1.69 mV which

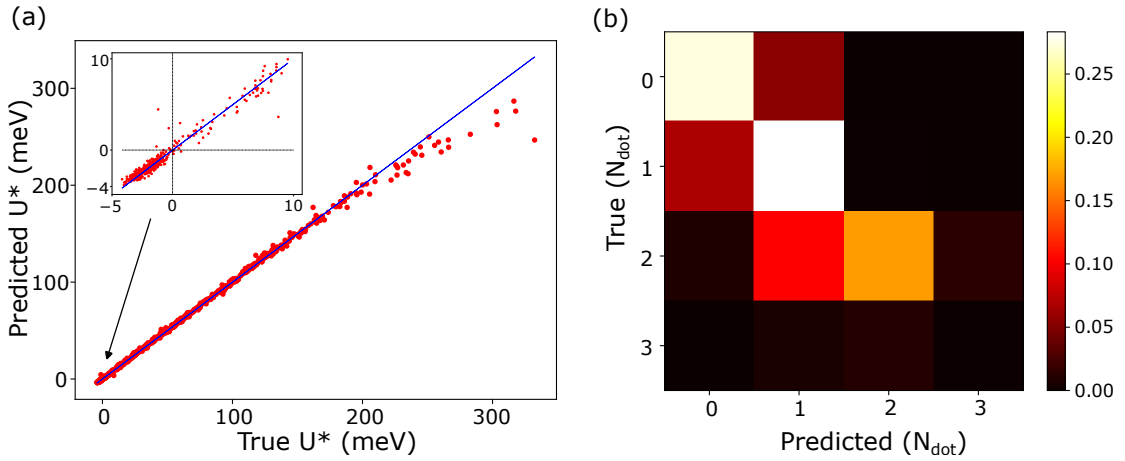

Figure 4.6: Performance of the CNNs on test data. (a) Comparison of $\mathcal{F}_U$ predictions with ground truth test data. The inset shows the points closest to $U^* = 0$ meV as the data is not evenly distributed about this value. (b) Confusion matrix of $\mathcal{F}_D$ dot classification on dot-abundant test data.

is sufficient to use the approximated potential as inputs to other functions to compute device features. To demonstrate this utility, a comparison of the electron density calculated from the output of $\mathcal{F}_\phi$ with the ground truth data is shown in Figure 4.7.

A limitation of $\mathcal{F}_\phi$ and $\mathcal{F}_\mathrm{U}$ is that they are trained for a specific heterostructure which defines the transformation $\phi_\mathrm{in} \rightarrow \phi_\mathrm{tot}$ and thus $\phi_\mathrm{in} \rightarrow \phi_\mathrm{tot} \rightarrow U^*$. For practical applications this means that only devices from a the same wafer can be simulated with the same approximated model.

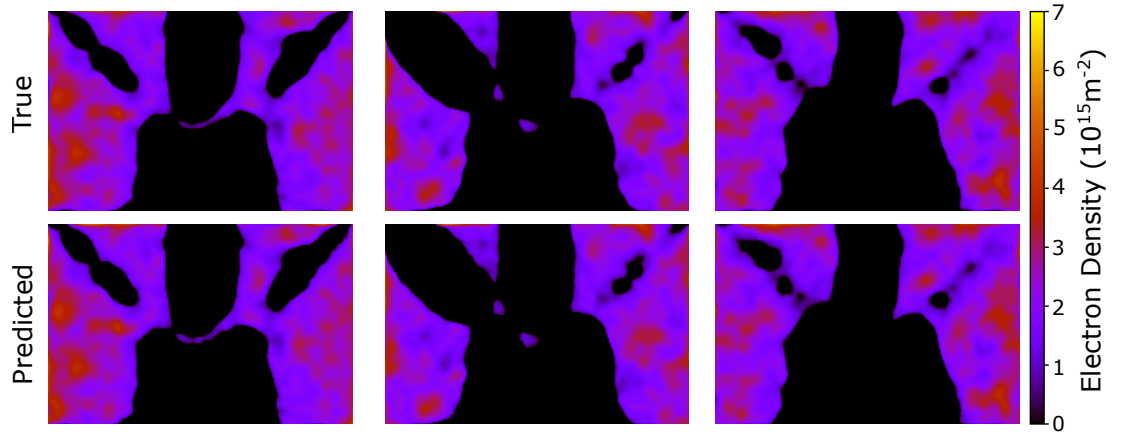

Figure 4.7: Example images of electron density computed using the output of $\mathcal{F}_\phi$ (bottom) and a comparison with the ground truth values (top). The centre example displays a double quantum dot which is reproduced by the $\mathcal{F}_\phi$ output. All images share a colour scale.

4.5 Machine Learning Accelerated Virtual Device

Beyond the models used in the next chapter, we now explore the possibility of efficiently simulating electrostatic quantum dot devices building from the electrostatic potential induced by the gate electrodes. The goal is to present a starting point necessary to produce a simulation which behaves like a real device across a range of transport regimes where fine detail in the accuracy of computation is sacrificed for speed. A fast simulator is necessary to test control algorithms designed for real devices without the need for expensive lab equipment and avoiding the risk of an errant algorithm (or human) breaking the device by operating outside of safe parameters.

The most common experimental measurements for characterising a device involve 1D and 2D scans of current over a range of voltages. In simulation, this requires repeated calculation of the electrostatic potential which is used to evaluate the transport regime and number of dots. The transport channel can be determined using the approach discussed in Section 4.2 with current being modelled as a simple binary value based on whether the transport channel is open or closed.

For dot identification, we note that the method discussed in Section 4.3 is computationally inefficient and requires some device specific knowledge. A more efficient means of dot identification are blob detection algorithms, such as the Laplacian of Gaussians [122]. For our simulation, a blob detection algorithm takes as input a binary image of the charge density induced by the self-consistent electrostatic potential. Enclosed regions of charge are then identified as dots and the location and size of the dots can be estimated by the blob detection algorithm.

When identifying quantum dots, it is important to track which dot is which relative to the index system chosen. For example, one may choose to index the dots from left to right and begin with a single dot labelled as dot 1, but upon varying the gate voltages a second dot forms further left than the original which then becomes dot 1. This relabelling results in errors when computing dot occupations during a scan of gate voltages, causing simulated charge stability diagrams to be unphysical. We employ a k-means clustering algorithm [123], where the number of clusters is

taken to be the maximum number of dots detected in the scan, to classify the dots based on their coordinates and circumvent this issue.

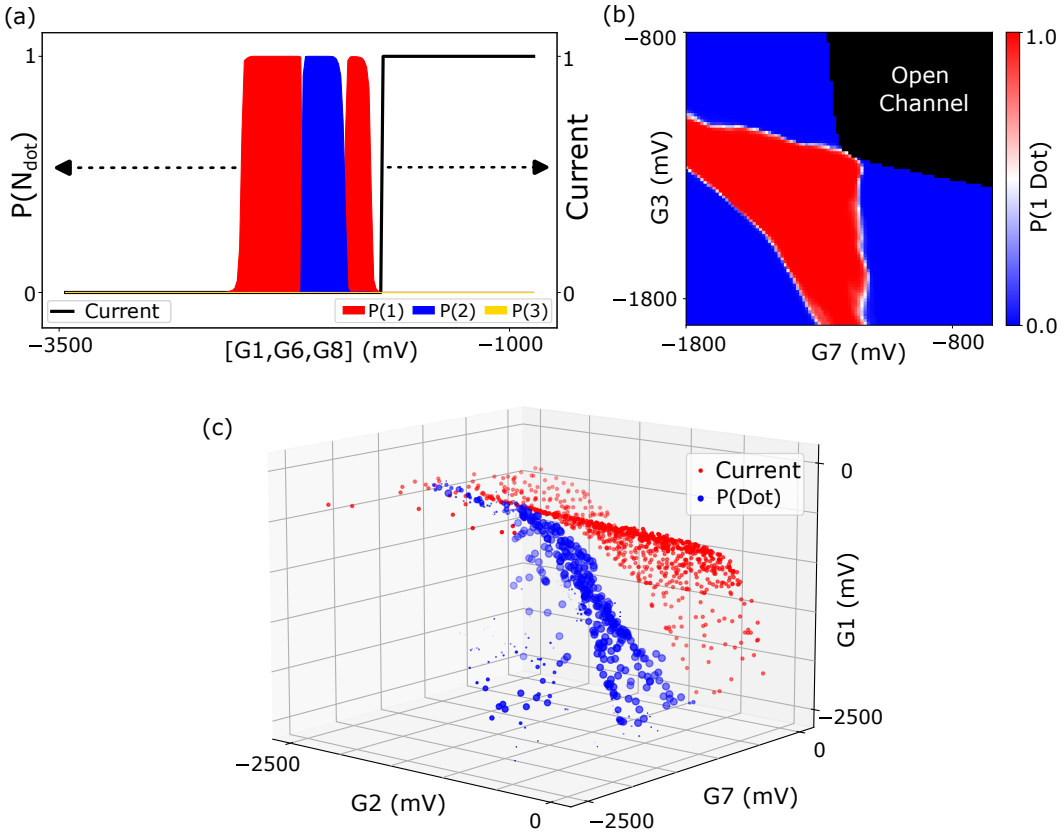

Figure 4.8: Examples of outputs from a virtual device constructed using the deep learning models $\mathcal{F}_U$ and $\mathcal{F}_D$. (a) A 1D scan over a vector of voltages which shows the open and closed channel regions along with the number of dots determined by $\mathcal{F}_D$ indicated by the probability $\mathrm{P}(N_{\mathrm{dot}})$ for $N_{\mathrm{dot}} \in \{0, 1, 2, 3\}$. Dashed arrows indicate which quantities relate to each y-axis scale. (b) A 2D voltage scan showing a corner of open channel current (black) and the region in which a single dot forms (red). (c) A 3D plot of the hypersurface separating open and closed channel regions (red) constructed from 1D scans of 1000 random gate voltage vectors. The most likely point to find a dot along each gate voltage vector is also shown (blue), where a larger point indicates a higher probability.

Combining these methods into a virtual device can yield useful results without considering further physical phenomena. Example outputs from such a virtual device (considering the gate architecture shown in Figure 4.1) are shown in Figure 4.8 which include 1D, 2D, and 3D gate voltage scans. The outputs contain information about the open or closed nature of the transport channel and the number of quantum dots, which are all key information for characterisation and tuning algorithms [61, 62,

124]. Accurately determining the number of dots based on transport measurements can be difficult [61], so having direct access to that number allows the success of characterisation and tuning algorithms to be evaluated more easily. We also note the time taken to produce the outputs in Figure 4.8 using a GPU as (a) 1s, (b) 42s, and (c) 250s. While transport measurement times on a real device can vary (e.g. different integration times), our virtual device times are an order of magnitude faster than typical transport measurements. This speed would allow for characterisation and tuning algorithms to be tested more efficiently and facilitate real-time integration of simulation with experiment.

4.6 Towards a Realistic Virtual Device

The previous section presented the functionality of our virtual device. In this section, we will briefly discuss the steps required to move towards a simulation which more closely matches experimental measurements. Quantum dot device simulation typically either takes a computationally expensive first principles approach [125], or is limited to a constant interaction model [20]. We aim to discuss a virtual device which captures a wide range of transport phenomena, while also remaining fast.

Following from the discussion of dot identification in the previous section, charge occupations of dots $\mathbf{Z}$ can be computed by integrating over the area of each dot and determining the integer charges $\mathbf{Q}$ which minimise the total electrostatic energy of the dots. The electrostatic energy of a system dots U_{dot} is computed by treating the dots as a system of capacitively coupled conductors with

$$U_{\text{dot}} = \frac{1}{2}(\mathbf{Q} - \mathbf{Z})^T C^{-1}(\mathbf{Q} - \mathbf{Z}), \tag{4.7}$$

where C is the inter-dot capacitance matrix. Rather than estimate the capacitance matrix elements by varying gate voltages as would be done in an experiment, we can define an inter-dot energy matrix as $E = \frac{1}{2}C^{-1}$ with

$$E_{ij} = \frac{\pi}{2}\delta_{ij}\int n^2(\mathbf{r}_i)d\mathbf{r}_i + |e|\int \phi_j(\mathbf{r}_i)n(\mathbf{r}_i)d\mathbf{r}_i, \tag{4.8}$$

where $\int d\mathbf{r}_i$ denotes an integral over the 2D coordinates of the i^{th} dot, $n(\mathbf{r}_i)$ is the charge number density on the i^{th} dot and $\phi_j(\mathbf{r}_i)$ is the electrostatic potential induced by the charge on the j^{th} dot as experienced on the i^{th} dot. The first term is the electrostatic energy of a dot in the Thomas-Fermi approximation [126] and the second term is the standard electrostatic energy $E = q\phi$ experienced by one dot from another. A version of this dot occupation model has proven effective in a 1D nanowire system [71, 127].

This model computes the charge occupations using only the electrostatic potential induced by the gate electrodes (and disorder), and can be automatically adapted to the number of dots present in the system. This is a step beyond constant interaction simulations of quantum dot devices which do not take into account the possible formation of new dots, or the transistor-like features associated with the transport channel being open or closed. Charging energies and gate capacitance effects are emergent from this approach as they are defined through the electrostatic potential which is controlled by gate voltages.

To model transport through arrays of dots, quantum master equations such as those discussed in Chapter 2 are appropriate. Such models require estimation of the interdot tunnel rates and tunnel rates between terminal dots and reservoirs. These tunnel rates can be approximated using the WKB approximation [128] which requires the semi-classical trajectory of a charge between two points s_0 and s_1 in the potential landscape $V(s)$ to give the transmission probability,

$$T_{12} \approx \exp\Big\{ -2 \int_{s_0}^{s_1} ds \sqrt{V(s)} \Big\}. \tag{4.9}$$

Estimating tunnel rates between quantum dots in an array by more accurate methods such as tight-binding models [129] would be more computationally expensive, but similar problems have been accelerated using deep learning [130]. Classical Markov chains have been used to simulate the transport of charge through quantum dots [71], but this approach fails to capture the correct bias triangle shape for a double quantum dot which implies that a quantum master equation approach would be more effective. Quantum master equation models also facilitate the simulation

of qubit dynamics using parameters estimated from the electrostatic potential, which is a significant advantage over classical models for extending virtual device functionality beyond steady state transport to dynamic quantum control.

4.7 Discussion

In this chapter we have presented an electrostatic model of a quantum dot device and approaches to determine the transport regime and the number of dots defined for a given set of gate voltages. These approaches have been accelerated using deep learning to allow fast simulation of a virtual device which can be used in real-time to test tuning algorithms, such as the algorithm presented in Ref. [61]. Such a virtual device could be considered a digital twin of a real device, but electrostatic disorder means that the model will not match the experiment. This gap between simulation and experiment will be investigated in the next chapter in the context of physics-aware machine learning using our virtual device.

We have discussed possible next steps to developing a more realistic virtual device, with components that can be accelerated by machine learning. Having a realistic and fast virtual device would provide an excellent testing ground for algorithms concerned with device design, device characterisation, and tuning quantum dots to qubits. Such a virtual device would circumvent the slow iterative process of fabrication and testing devices, and widen access to quantum device control without the need for expensive equipment.

5

Bridging the Reality Gap in Quantum Devices

The author worked jointly with Hyungil Moon to develop the inference algorithm presented in this chapter. Hyungil Moon developed the reparameterisation of the disorder potential. The author obtained the experimental data, with some assistance from Barnaby van Straaten and Federico Fedele. The author implemented all instances of the inference algorithm, and performed analysis of the resulting data.

Simulations often require fewer resources than real experiments but rarely capture the full complexity of a system, thus limiting their practical application. Some parameters in a simulation may be poorly estimated leading to a gap between simulation and reality, but this gap is widened further when there are quantities which are not directly observable.

Solid-state quantum devices of nominally identical design will often display different characteristics. This variability hinders the scalability of otherwise promising qubit realisations, such as in the spin states of electrons confined in electrostatically-defined quantum dots [21, 129, 131]. Different devices exhibit different electron transport features for identical gate voltage values. This variability is even observed in the same device after being exposed to thermal cycling [61]. In particular,

electrostatic disorder induced by randomly located donor ions can be a significant source of variability in delta-doped semiconductor quantum dot devices [132, 133].

In this chapter we develop a physics-aware machine learning approach to access the disorder characteristics that can only be observed indirectly. We use transport measurements of an electrostatically-defined quantum dot device in an AlGaAs/GaAs heterostructure to inform and verify our approach. To assess the performance of inference results we use the disorder potentials produced by the algorithm to predict the electron transport regime of new measurements. We also use a physical model to determine the number of quantum dots at a given gate voltage location. Using posterior disorder samples within this model allows us to predict the voltage locations of double quantum dots and verify these predictions with the experiment.

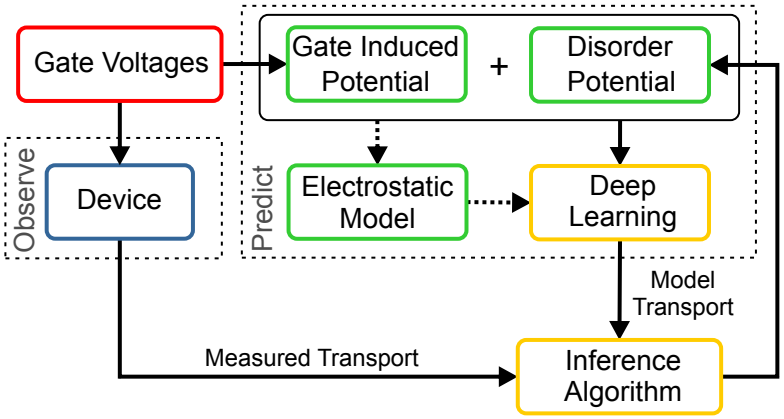

Figure 5.1: Schematic of the physics-aware disorder inference process. Colours indicate the following; red for experimentally controllable variables, green for quantities relevant to the electrostatic model, blue for experimental device, and yellow for machine learning methods. Dashed arrows represent the process of generating training data for the deep learning approximation and are not part of the disorder inference process.

5.1 The Device

The gate architecture of the device used for the experiments in this chapter is depicted in Figure 4.1, where each of the gate voltages can be set to any value between 0 V and −2 V; gate G6 is held at 0 V to avoid leakage currents. The device is operated at millikelvin temperatures in a dilution refrigerator.

A bias is applied to Ohmic contacts to drive current through the device from source to drain, and applying voltages to the gates allows for the control of this current. A random distribution of Si donor ions contributes a disordered component to the electrostatic potential experienced by electrons confined in a 2DEG. The distribution of donor ions is thought to freeze at low temperatures with rearrangement only possible significantly above device operating temperature [134].

5.2 Physics Aware Machine Learning Algorithm

The main components of our physics-aware machine learning algorithm are summarised in Figure 5.1. To infer the disorder potential we use a combination of transport measurements and predictions from a physical model. The physical model is the electrostatic simulation discussed in Chapter 4. Many simulations with different parameter settings are required to compare this physical model with transport measurements. To accommodate this need without extreme computation times, we develop a fast approximation of the model using deep learning as discussed in the previous chapter.

The transport measurements and electrostatic simulations inform the inference algorithm to produce posterior samples representing plausible disorder potentials. The inference mechanism follows the philosophy of approximate Bayesian computation [135–138] by utilising the deep learning approximation of the electrostatic model.

Directly implementing this inference would lead to impractical computation times. This is because electrons are confined in a 2D electron gas (2DEG), and thus the disorder potential to be inferred is a dense 2D function where each pixel value is a parameter to be inferred. We develop a novel reparameterisation to greatly reduce the dimensionality of the inference problem, while selecting the most informative regions of the disorder potential. This maps the non-parametric 2D disorder potential into a parametric model which approximates the function in the spatial and spectral domains simultaneously using an inducing point approximation of a Gaussian process [139–141], and random Fourier features [142–147]. Our approach can be adapted to capture various sources of disorder which may be

present in different device designs by considering an appropriate kernel for the Gaussian process. The algorithm finds optimal values for the spatial and spectral parameters by computing the likelihood of a measurement from a device, given a set of parameters used in the model to predict the outcome of the measurement.

5.3 Electrostatic Model

The physics aware machine learning algorithm requires a model of the quantum dot device. We use an electrostatic model, accelerated by deep learning as discussed in the previous chapter. Here we summarise the key points specific to the results of this chapter.

The effects of gate electrodes and donor ions on the electron density in the 2DEG are calculated self-consistently using the pinned surface model [113, 114]. Delta doping results in donor ions being randomly located in a plane at a constant height of 45 nm above the 2DEG. With $\mathbf{r}=(x,y)$ denoting a location in the 2DEG plane, the total electrostatic potential is

$$\phi_{\mathrm{tot}}(\mathbf{r}) = \phi_{\mathrm{g}}(\mathbf{r}) + \phi_{\mathrm{d}}(\mathbf{r}) + \phi_{\mathrm{s}}(\mathbf{r}) + \phi_{\mathrm{e}}(\mathbf{r}), \tag{5.1}$$

where the electrostatic potential contributions are ϕ_{g} from the gate electrodes, ϕ_{d} from the randomly located donor ions, ϕ_{s} from surface states, and ϕ_{e} from the presence of electrons in the 2DEG. A self-consistent solution for ϕ_{tot} is computed using an iterative under-relaxation process as in Ref. [113].

Following the methods presented in Section 4.2, a semi-classical electron trajectory between source and drain is calculated. The maximum potential along this path, U^*, determines the transport channel regime. The transport channel is considered closed if U^* is greater than or equal to the Fermi energy μ_F. The electron trajectory approximated by the MST path can also be used to determine the number of quantum dots formed by a given ϕ_{tot}, as discussed in Section 4.3.

For disorder inference we require fast prediction of the transport regime, determined by U^* in our model, given gate voltages and a disorder potential. Our implementation of the self-consistent electrostatic model and MST path require

up to 10 seconds to calculate U^* in serial computation. This computation time is impractical for the large batches of U^* required for the inference algorithm. Deep learning methods, and their ease of implementation on GPU hardware, allow for a significant acceleration [148, 149].

We use the models $\mathcal{F}_U$ and $\mathcal{F}_D$ presented in the previous chapter to provide a fast computation of minimax energy U^* and the number of dots N_{dot}, respectively. These models provide the acceleration necessary for practical computation times in the inference algorithm and predicting device features using posterior disorders, with computation times of under a millisecond per output using a GPU (GTX 1080 Ti).

5.4 Disorder Reparameterisation

The disorder potential used in the electrostatic model is a dense 2D grid covering the entire 2DEG plane, with an example displayed in Figure 4.2(b). A dense grid is unnecessary for inference since ϕ_{d} is continuous and values can be interpolated from a sparse grid. Using a dense grid would be unfeasible even with the reduced resolution of CNN inputs considered in the previous chapter due to the large number of parameter values to infer.

We develop a reparameterisation of this dense grid, with the objective to find a set of n_Z locations $Z = \{\mathbf{r}_k^Z | k = 1, \ldots, n_Z\}$, where the disorder potential values on those locations sufficiently determine the transport regime. Following the literature of Gaussian process regression [139], Z defines a set of inducing points. In our experiments, we parameterise Z as a 14×14 uniform grid defined by two corner points, with the initial grid shown in Figure 5.2(a).

Our reparameterisation requires the locations of the inducing points Z as well as the values of the disorder potential on these points, represented by a vector $\boldsymbol{\alpha} = [\phi_{\text{d}}(\mathbf{r}_1^Z), \ldots, \phi_{\text{d}}(\mathbf{r}_{n_Z}^Z)]$. The full dense grid of ϕ_{d} cannot be exactly recovered from the values on Z, because the inducing points are too sparse and random disorder potential variations between the points could influence the transport regime. This variability is encoded in the vector $\boldsymbol{\beta} = [\epsilon_1, \ldots, \epsilon_{2q}]$ containing amplitudes of random

Fourier features [142–147], where q is the number of frequencies considered. The parameters contained in $\boldsymbol{\beta}$ are thus dependent on Z.

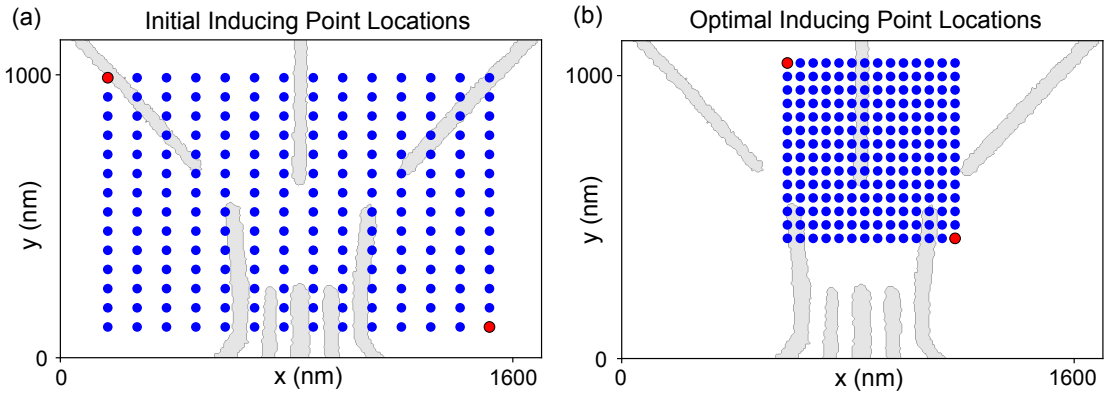

Figure 5.2: Gate architecture overlaid with inducing point locations Z, indicated by blue dots (a) before optimisation and (b) after optimisation. Red circles indicate the two corners defining the rectangular array of inducing points. The location of these corners are optimised to ensure that the disorder potential values at the inducing points determines whether the transport channel is open or closed. Hence the optimised inducing points are located closer to the source and drain reservoirs.

With optimal inducing points Z_{opt}, the disorder potential values contained in $\boldsymbol{\alpha}$ sufficiently determine the transport regime, while the contribution of random Fourier features from $\boldsymbol{\beta}$ is marginal. A numerical optimiser is used to find Z_{opt}, where the optimisation objective is to minimise the effect of $\boldsymbol{\beta}$ on transport regime predictions made by $\mathcal{F}_U$. During optimisation, the disorder potential contributing to the input of $\mathcal{F}_U$ is approximately reconstructed from Z, $\boldsymbol{\alpha}$, and $\boldsymbol{\beta}$ using a deterministic function f which is defined in Appendix C,

$$\phi_{\text{d}} \approx \hat{\phi} = f(Z, \boldsymbol{\alpha}, \boldsymbol{\beta}). \tag{5.2}$$

The optimisation of Z can be performed on simulated data, and the optimised inducing points used by our inference algorithm are shown in Figure 5.2(b). We observe that the inducing points are located where the transport channel is more likely to be depleted, so that the disorder potential on Z_{opt} can determine the transport regime of the device. Detailed formulation and implementation of the inducing point optimisation algorithm can be found in Appendix C.

5.5 Bayesian Inference

To reconstruct the disorder potential, we must infer suitable values of $\boldsymbol{\alpha}$ and $\boldsymbol{\beta}$ in addition to determining Z_{opt}. To do this, the inference algorithm requires measurements of current in gate voltage space. We generate random directions in the 7-dimensional gate voltage space, each defined by a unit vector $\mathbf{u}_j$ normalised such that $\max_i |u_j^i| = 1$ and $u_j^i \leq 0$ for $u_j^i \in \mathbf{u}_j$. A location in gate voltage space is defined as $\mathbf{v} = \mathrm{R}\mathbf{u}_j$, where R is the voltage distance along $\mathbf{u}_j$. Our inference algorithm considers information about the location of the boundary between open and closed channel transport. To obtain this information, stored in a dataset D, current is measured along a given $\mathbf{u}_j$ from the origin at $R = 0$ mV to the device voltage limit at $R = 2000$ mV. Each of these current measurements contributes 2 entries in D; the voltages immediately before and after current drops to half the open channel current, paired with $y = 1$ and $y = 0$ respectively. The resulting dataset can be defined by $D = \{(\mathbf{v}_i, y_i) | i = 1, \ldots, 2n_{\text{u}}\}$, where n_{u} is the number of unit vectors considered. We use $n_{\text{u}} = 200$, which is well below the typical data requirements of deep learning methods used to predict features of quantum devices [70, 73].

To infer $\boldsymbol{\alpha}$ and $\boldsymbol{\beta}$ using D we define a prior distribution $p(\boldsymbol{\alpha}, \boldsymbol{\beta})$ and a likelihood of data $p(D|\boldsymbol{\alpha}, \boldsymbol{\beta})$. The posterior distribution then follows the Bayes rule, $p(\boldsymbol{\alpha}, \boldsymbol{\beta}|D) \propto p(D|\boldsymbol{\alpha}, \boldsymbol{\beta}) p(\boldsymbol{\alpha}, \boldsymbol{\beta})$. In our formulation, $p(\boldsymbol{\alpha}, \boldsymbol{\beta})$ follows the multivariate normal distribution having the zero mean vector and diagonal covariance matrix. The likelihood function utilises the estimated U^* from the CNN $\mathcal{F}_U$ for each data point $(\mathbf{v}_i, y_i)$ by calculating ϕ_g from $\mathbf{v}$, and approximating ϕ_{d} from $\boldsymbol{\alpha}$ and $\boldsymbol{\beta}$. As discussed in Appendix C, we use a binomial likelihood function which compares the observed data with the probability of current predicted using $\boldsymbol{\alpha}$ and $\boldsymbol{\beta}$. This likelihood function reads

$$p(\boldsymbol{\alpha}, \boldsymbol{\beta}|D) \propto p(\boldsymbol{\alpha}, \boldsymbol{\beta}) \prod_{i=1}^{2n_u} \left(p_i^{\text{GP}}\right)^{y_i} \left(1 - p_i^{\text{GP}}\right)^{1-y_i}, \tag{5.3}$$

where p_i^{GP} is the probability of current estimated using our Gaussian process reparameterisation and the i^{th} set of gate voltages, and y_i is the observed state of the transport channel for the i^{th} measurement.

A set of n_s posterior samples $\{(\boldsymbol{\alpha}_i, \boldsymbol{\beta}_i)|i = 1, \ldots, n_\mathrm{s}\}$ can be drawn from Markov-chain Monte Carlo (MCMC) methods. Using Eq. (5.2), the posterior samples of $\boldsymbol{\alpha}$ and $\boldsymbol{\beta}$ generate a set of 2D disorder potentials $S_{\hat{\phi}} = \{\hat{\phi}_i|i = 1, \ldots, n_\mathrm{s}\}$, which can be used for CNN inputs. The CNN computation is differentiable, unlike the electrostatic model and path finding algorithm, allowing us to use Hamiltonian Monte Carlo (HMC) [150] with TensorFlow Probability [151].

5.6 Posterior Distributions of Disorder Potentials

We first test the inference results on a simulated dataset before considering real measurements. The inference algorithm produces a set of posterior values for the inducing point values, $\boldsymbol{\alpha}$, and random Fourier feature amplitudes, $\boldsymbol{\beta}$. These values are used to produce a set of posterior samples $S_{\hat{\phi}}$ of the real-space disorder potential as outlined above. The resolution of the posterior disorder potentials can be chosen depending on the desired use (e.g. as inputs to $\mathcal{F}_\mathrm{U}$, $\mathcal{F}_\mathrm{D}$, or the self-consistent electrostatic model). Figure 5.3 shows the true disorder and posterior samples for two iterations of the inference algorithm on a simulated device. To further visualise the performance of the inference algorithm we inspect the variation of inducing point values $\boldsymbol{\alpha}$ used to produce the posterior disorder potentials. A low posterior standard deviation on an inducing point means the inference algorithm has learned more about the disorder potential at that location. The number of inducing points with a low posterior standard deviation increases with the size of the training dataset as shown in Figure 5.4. This indicates that the inference algorithm has gained information about a larger area of the disorder potential by considering more random directions in voltage space. We can also observe that even for a small training dataset, the inference results are most confident about the disorder potential values at the tip of gate G1 (the 'nose') which reflects its role in depleting the electron density along the path from source to drain.

Using experimental datasets with $n_\mathrm{u} = 200$, the standard deviation of posterior inducing point values used to generate $S_{\hat{\phi}}$ is shown in Figure 5.5 for three thermal cycles of the same device. Just as for the simulated datasets shown above, in each

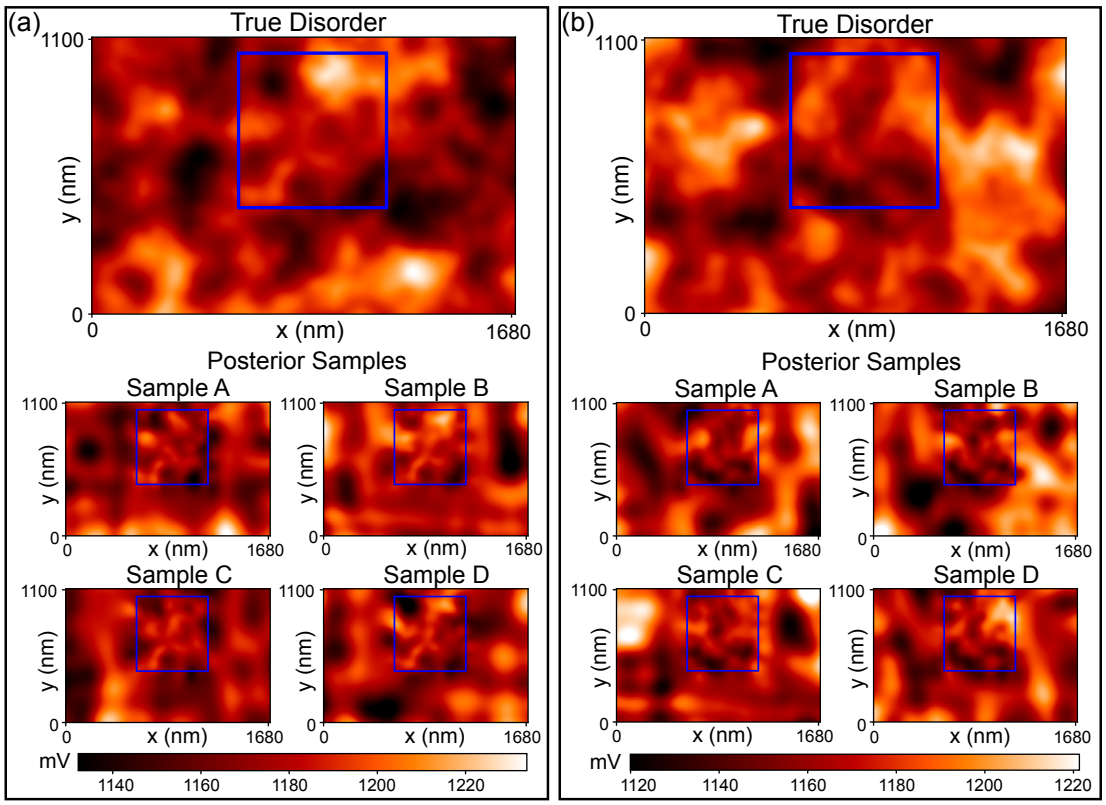

Figure 5.3: The true disorder and four randomly selected posterior disorder samples for two iterations of the inference algorithm on a simulated device, (a) and (b). The true disorder is randomly generated using the electrostatic model with randomly located donor ions. The blue box on each disorder potential indicates the region spanned by the optimised inducing points. The posterior disorder samples are the same resolution as the true disorder, (134x206). In each subfigure, the posterior disorders have more detailed features within the box, and qualitative similarities with the true disorder can be observed. All plots in each subfigure share the same scale, as shown at the bottom of each subfigure.

case the posterior standard deviation is lowest in regions surrounding gate G1. The lowest standard deviation on a given inducing point is approximately 2 mV using the simulated measurements to inform the inference algorithm, and approximately 5.5 mV using experimental measurements. This performance difference can be expected as the simulated device is a controlled and self-contained environment, whereas the experiment will have more unknowns which may not be accounted for in the model. Such unknowns may include fabrication variations, material defects, or quantum mechanical transport effects not considered in the electrostatic model.

The posterior samples shown in Figure 5.3 exhibit much more detailed features inside the region spanned by the optimised inducing points where qualitative simi-

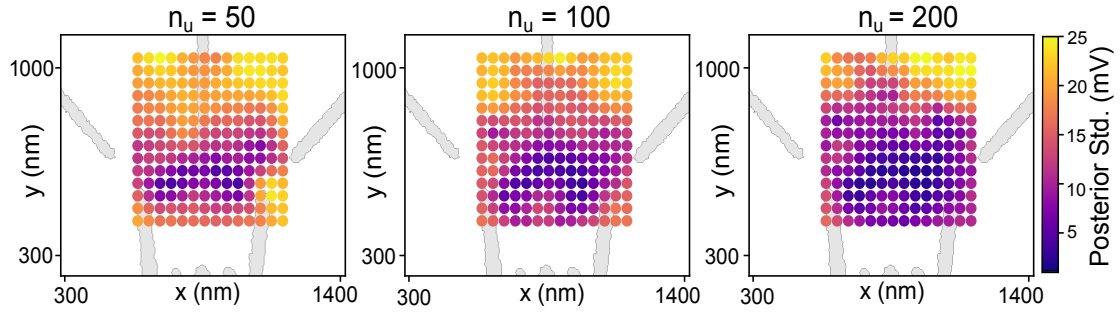

Figure 5.4: Disorder inference results using simulated data for three training dataset sizes ($n_{\mathrm{u}} = 50, 100, 200$), with $D = \{(\mathbf{v}_i, y_i)|i = 1, \ldots, 2n_{\mathrm{u}}\}$ as discussed in Section 5.5). The inducing point locations are indicated by circles with the gate structure in the background. The colour of each inducing point represents the standard deviation of the posterior disorder potentials at that point.

larities with the true disorder observed. This further demonstrates the information gained at these points (in addition to Figure 5.5). Features outside the inducing point region are governed by the amplitudes of random Fourier features contained in $\boldsymbol{\beta}$ which are necessary to ensure the posterior samples are continuous and suitable to be used as inputs to $\mathcal{F}_{\mathrm{U}}$ and $\mathcal{F}_{\mathrm{D}}$.

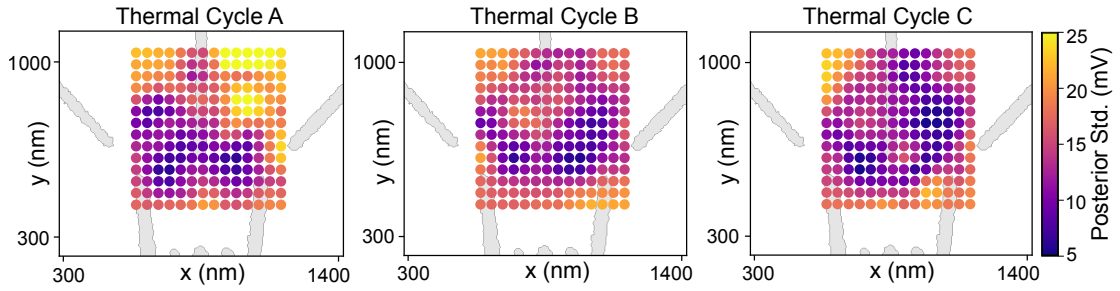

Figure 5.5: Disorder inference results using experimental data for three thermal cycles (A,B,C) of the same device. The inducing point locations, Z_{opt}, are indicated by circles with the gate structure in the background. The colour of each inducing point represents the standard deviation over posterior samples of the disorder potential value at that point.

5.7 Transport Channel Prediction

After performing inference of the disorder potential, the set of posterior samples can be used in the electrostatic model approximated by $\mathcal{F}_U$. We verify the posterior prediction of the distance R_{C} required to close the transport channel in both a simulated and experimental device for a set of unit vectors, $\{\mathbf{u}_i|i = 1, \ldots, n_{\mathrm{v}}\}$.

We set R_{C} to be the point at which the current drops below 50% of the open channel current. For a given $\mathbf{u} \in \{\mathbf{u}_i | i = 1, \ldots, n_{\mathrm{v}}\}$, we calculate the mean value of R_{C} predicted using each posterior sample in $S_{\hat{\phi}}$. To probe the generality of inference results, we evaluate predictions using the measurements which inform our inference (training data) and additional measurements which are not used by our inference algorithm (test data). The training and test datasets use $n_{\mathrm{v}} = n_{\mathrm{u}} = 200$ and $n_{\mathrm{v}} = 300$ unit vectors respectively.

For a simulated device in which the true disorder is known but remains hidden from the algorithm, we compare the performance of random and posterior disorder potentials when predicting the value of R_{C} over 5 independent iterations of the inference algorithm. Random disorder potentials, generated using the electrostatic model with randomly located donor ions, predict R_{C} with a mean absolute percentage error (MAPE) of 7.0% across training and test data. In contrast, posterior samples predict the value of R_{C} with a MAPE of 0.3% on training data, and 0.5% on test data. This demonstrates that the inference algorithm is successful in finding disorder potentials which effectively describe features of a simulated device.

We then verify the posterior prediction of R_{C} in a real device. Thermal cycling the device 4 times, we run a total of 5 iterations of the inference algorithm. The value of R_{C} is predicted with a MAPE of 1.5% for training data and 2.0% for test data. The MAE of R_{C} predictions is 24.3 mV and 31.9 mV for training and test data respectively. Random disorder potentials predict R_{C} with a MAPE of 7.5% across training and test data. We conclude that inference results are effective in predicting the gate voltages which close the transport channel in a real device. The added complexities of fabrication and materials defects, as well as a quantum mechanical treatment of transport features such as Coulomb peaks are not considered by our electrostatic model, and hence not directly captured by the Gaussian process. This additional complexity may contribute to the reduced performance of the inference algorithm compared to the simulated device. Our inference algorithm may still capture some of this extra complexity since a Gaussian process contains greater flexibility than a direct fit of a physical model. This flexibility, combined with

an appropriate Gaussian process kernel, is imperative to the applicability of this algorithm to different device realisations.

5.8 Double Quantum Dot Prediction

Inference results can be validated by predicting device features not used to inform the inference process, with quantum dots being a natural choice for our device. We implement a method requiring minimal knowledge of the transport characteristics of a particular device. Three pieces of information are required, i) quantum dots form near the closed channel boundary, ii) gates G3 and G7 in our device couple most strongly to dot energy levels, and iii) double quantum dots form features with periodicity in two gate voltage directions in transport measurements.

Our method of finding double quantum dots using posterior disorder samples is summarised in Figure 5.6(a). Random unit vectors $\mathbf{u}$, are generated and scanned from $R = 0$ mV to $R = 2000$ mV in the simulated device. A randomly chosen unit vector is unlikely to lead to double dot transport features given the sparsity of double dots in voltage space. Based on predictions made by $\mathcal{F}_D$ for each posterior disorder, we select candidate voltage vectors. If $\mathcal{F}_D$ detects a double dot along a vector for a given posterior disorder, the vector's score is increased by one. Vectors with a score greater than a selected threshold (taken to be $n_s/3$) are accepted to be investigated further in a test device.

Accepted vectors only indicate a direction in gate voltage space in which double quantum dot features could be observed in a test device. As these features are expected to be found near the closed channel boundary in transport measurements, we investigate multiple voltage locations near this boundary along each accepted vector. To investigate each accepted $\mathbf{u}$, an automated protocol performs a current measurement along $\mathbf{u}$ from the origin to the device voltage limit. The gate voltages are then set to the boundary between open and closed channel regimes along $\mathbf{u}$, identified by a drop of 20% from open channel current. To allow for the identification of double quantum dot transport features, gates G3 and G7 are scanned in a 200 mV$\times$200 mV window centred at this gate voltage location. Such 2D scans are

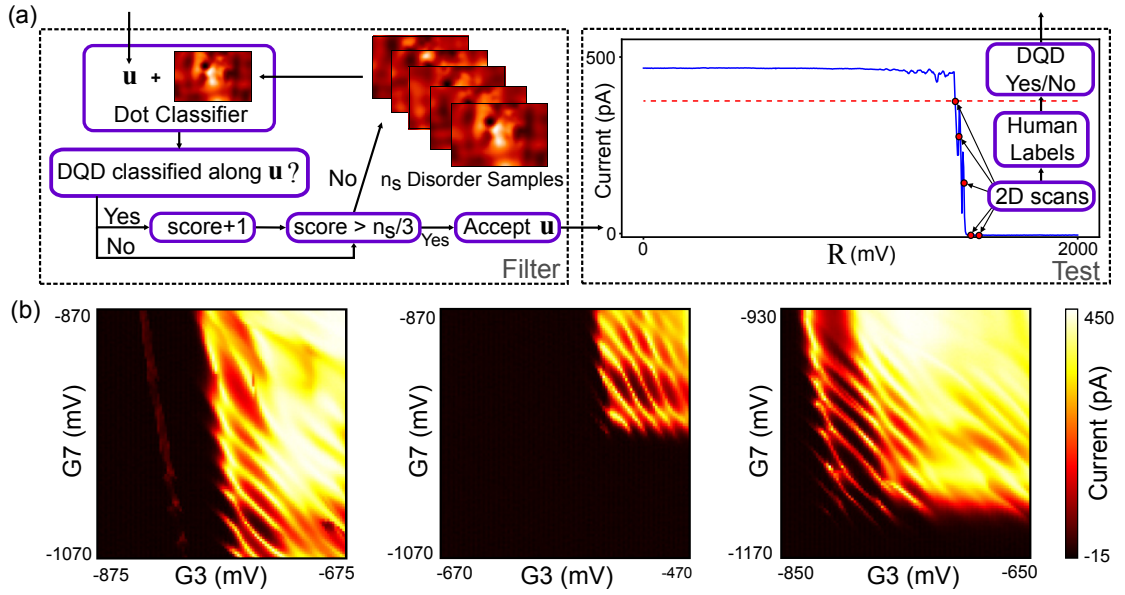

Figure 5.6: (a) Predicting double quantum dot locations. A unit vector $\mathbf{u}$ is passed to the filter which determines whether the vector is considered for the test device (which can be a real or simulated device). The filter uses the dot classifier $\mathcal{F}_D$ to scan along $\mathbf{v} = \mathrm{R}\mathbf{u}$ for each of the n_s disorder samples and the score is increased for each disorder sample which produces a double dot in the scan. Posterior disorder samples from the inference algorithm are shown. Vectors with a score greater than $n_\mathrm{s}/3$ are accepted to be tested. An example current measurement (solid blue line) of a voltage vector from the origin to the limit of device operation is shown. The dashed red line indicates the 80% threshold used to begin 2D current scans over gates G3 and G7. The 2D scans are taken at intervals along the extent of the original current measurement (indicated by red circles). The resulting 2D current scans are passed to multiple human experts to label the presence of double quantum dots. (b) Example current scans over G3 and G7 which scored highly for double dots when labelled by 6 human experts for 3 different unit vectors. Each scan is a 200 mV $\times$ 200 mV window with the voltages associated with the direction of $\mathbf{u}$ at the centre.

subsequently performed at intervals of 13.3 mV in R along the direction of $\mathbf{u}$ until the maximum current value in a 2D scan drops below 100 pA. The 2D scans are labelled by 6 human experts to determine the presence of double quantum dot features along $\mathbf{u}$. Multiple human experts are required as double quantum dot features are often subjective to human labellers and difficult to identify computationally [61].

As an initial test of the filtering process we use posterior, random, and featureless (i.e. constant valued) disorder potentials across 5 independent runs of the inference algorithm in a simulated device. Fewer vectors are accepted to be tested when using featureless disorders compared to using posterior or random disorders, and vectors

which produce the highest scoring 2D scans, identified in results of posterior disorder predictions, are not found by featureless disorders. We use the receiver operating characteristic (ROC) curve for posterior, random, and featureless disorders to identify suitable values for the threshold, as shown in Figure 5.7(a). A good classifier has a low FPR and high TPR. Posterior disorders and random disorders both perform much better than featureless disorders and a random classifier. Posteriors perform better than random disorders which is evidence of the success of our inference algorithm. A more detailed comparison in Figure 5.7(b) shows that the posterior curve has a much sharper increase in true positive rate. We choose a threshold value of $n_s/3$ for the experiment as it allows both posteriors and random disorders to have a moderate true positive rate, while maintaining a low false positive rate. A low false positive rate is desirable because experimental 2D current scans required for human labelling are slow. Other threshold values can be chosen depending on the desired acceptance rate. Due to the poor performance of featureless disorders, we do not consider them further.

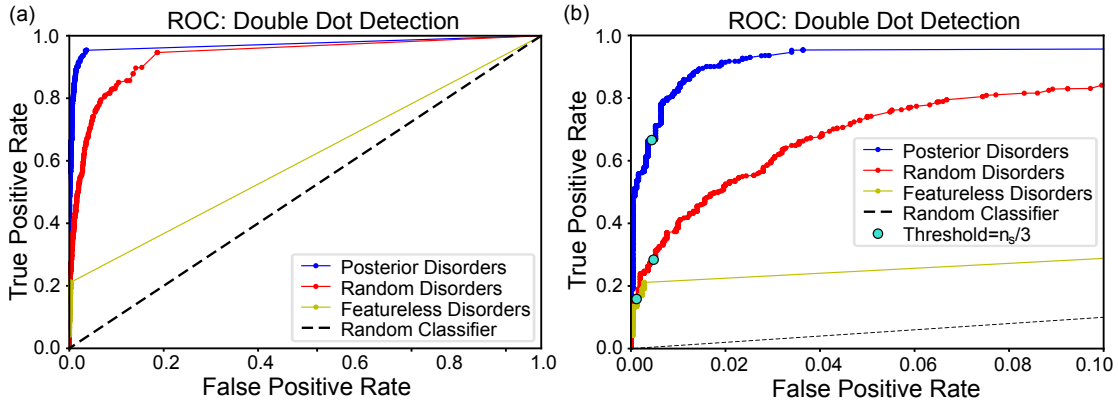

Figure 5.7: The receiver operator characteristic (ROC) curve, comparing the false positive rate (FPR) and true positive rate (TPR) across the domain of possible thresholds $[0, n_s]$ for n_s disorder samples. The mean FPR and TPR from 5 independent iterations of the inference algorithm and filtering process is shown. (a) The ROC curves for the double dot filter process using posterior (blue line), random (red line), and flat (yellow line) disorders, along with the ROC curve associated with a random classifier (dashed line). (b) The same ROC curves as shown in (a), but with a truncated false positive axis. The location corresponding to a threshold of $n_s/3$ as used in the experiment is indicated by a turquoise circle on each curve.

Similar to our R_C predictions, we first test the predictive power of posterior

disorders in a controlled environment (i.e. in a simulated device in which the true disorder potential is known). By selecting random unit vectors we find a mean double dot occurrence rate of 0.83% using several random disorder potentials, each generated using the electrostatic model with randomly located donor ions. We thus perform disorder inference followed by vector filtering. We do not scan gates G3 and G7 as necessary in the real device since $\mathcal{F}_D$ can determine the number of dots at a point in voltage space. After performing vector filtering, double dots are correctly identified in 28% of instances using random disorders, and in 67% of instances using posterior samples. This is consistent with the TPR values shown in Figure 5.7 and demonstrates that posterior disorder samples have greater predictive power than random disorder potentials.

In the real device, we produce two sets of posterior samples from independent iterations of disorder inference. Accepted vectors and the associated labels from both iterations are combined to provide larger sets of results using posterior and random disorders. Examples of 2D current scans which scored highly for double quantum dot features are shown in Fig 5.6(b) with examples of 2D current scans for a range of double dot scores in Appendix D. To assess the success of our dot prediction method, a Binomial distribution is fitted to posterior and random results, where the probability of finding a double dot along an accepted voltage vector is $P(\mathrm{DD}) = p$, with $P(\overline{\mathrm{DD}}) = 1 - p$. The fit results in 95% confidence intervals of $0.235 < p_{\mathrm{post}} < 0.449$ using posterior samples, and $0.004 < p_{\mathrm{rand}} < 0.149$ using random disorders.

These values, with a separation of the 95% confidence intervals, demonstrate that using posterior disorders results in a higher rate of success than random disorders in finding experimental double quantum dots. The width of the confidence intervals is a consequence of the quantity of data available, nevertheless a clear separation in these relatively wide intervals furthers the demonstration that our posterior disorders outperform random disorders. The success rate of posterior disorders is not high enough for a reliable tuning algorithm, but future work may improve on our approach (e.g. with more sophisticated physical models). Our results show that the inference algorithm produces disorder potentials with predictive power

beyond the original domain of training data, and can reduce the human expertise required to tune a double quantum dot.

5.9 Discussion

In this chapter we have presented a physics-aware machine learning approach to understand and narrow the reality gap induced by electrostatic disorder in a GaAs device. We demonstrate that hidden disorder in a nanoscale electronic device can be inferred with indirect measurements and physics-aware machine learning. The reparameterisation of the disorder potential proves effective in reducing the dimensionality of the problem, and the acceleration of an electrostatic model with a differentiable convolutional neural network allows for Bayesian inference. The entire inference process, from inducing point location optimisation to selecting posterior samples is general and applicable to any gate structure. Device specifics are contained in the electrostatic model as discussed in the previous chapter, and can easily be adapted to other gate architectures and materials. Different device realisations can also be considered by using an appropriate physical model, and updating the Gaussian process kernel to capture the disorder characteristics.

We demonstrate the benefits of model-assisted tuning, with results indicating that the posterior disorders perform better than random disorders when predicting the gate voltage locations of double quantum dots. We therefore conclude that the use of physics-aware machine learning has narrowed the reality gap. The remaining gap between simulation and experiment can be attributed to further unknowns such as fabrication defects in gate design, material defects, and quantum transport properties which are not considered in our physical model. Despite these additional complexities of real devices, our posterior disorders retain significant predictive power indicating that the inference algorithm has the flexibility to effectively capture the electrostatic landscape. The generality of this method and the minimal data required for inference are promising qualities for future utility in understanding nanoscale quantum devices. Our approach could be used to study the variability of devices in large arrays, extending over micro and millimeter areas [152–154]. Such

studies would advance our understanding of fabrication processes and accelerate the development of quantum dot devices as a platform for quantum computation.

6

A Differentiable Quantum Master Equation Solver

The differentiable master equation solver presented in this chapter was developed solely by the author. Application of the solver to each of the discussed models, including the parameter optimisation and data analysis, was performed by the author.

In this chapter we apply the concepts of differentiable programming to develop a fast and differentiable quantum master equation solver. Such a solver is necessary for use in machine learning algorithms which take advantage of gradient descent methods and requiring many evaluations of a model. We integrate our differentiable solver with optimisation algorithms and Bayesian inference, and test its performance on weak-coupling models of transport in quantum dot systems. We first outline our differentiable master equation solver and demonstrate its effectiveness and speed before applying it to parameter estimation problems. Such a differentiable model has not been previously presented in the literature in the context of steady state solutions, but there have been recent advances in using differentiable models for simulations of quantum systems with a focus on optimal control [155–158]. The focus of our model in a quantum transport setting is on steady state solutions,

however we also demonstrate the capability of our model to calculate time evolution of the charge state of a double quantum dot system.

We use our differentiable model in the context of parameter estimation using (simulated) quantum transport data in single and double quantum dot systems. As gradients cannot be computed with respect to all parameters defining the transport measurements under consideration, we develop a loss function to optimise these parameters while also utilising the differentiable nature of the model. Gradient descent methods are used to fit the remaining differentiable parameters, and Markov chain Monte Carlo methods are used to estimate posterior distributions from which parameter uncertainties can be obtained. We first demonstrate the effectiveness of our method using a model of a single quantum dot with an orbital excited state. Moving to a model of a double quantum dot coupled to a phonon bath, this fitting process also allows us to perform model selection with respect to phonon spectral densities relating to different materials and dimensions as discussed in Section 2.4. Such an approach would prove useful for determining the spectral density from measurements similar to those presented in Section 3.6.

6.1 Differentiable Model

For the purpose of parameter estimation, we use gradient-based methods which benefit from the use of differentiable programming. We develop a differentiable quantum master equation solver which is implemented using TensorFlow [159]. This facilitates evaluation of the gradient of an observable (or any other quantity) with respect to the master equation parameters, without the need for finite-element methods. Gradients can be obtained with similar computation time to forward evaluation of the model using automatic differentiation and back-propagation. Our implementation is not specific to the weak-coupling models considered in this thesis; our solver can determine the steady state solution and time evolution for a given Liouvillian superoperator acting on the system density matrix. Details of the numerical formulation of a quantum master equation and its steady state solution can be found in Appendix E.

Using TensorFlow allows direct use of in-built gradient-based optimisation methods such as Adam [160], and Bayesian inference methods such as Hamiltonian Monte Carlo (HMC) [150] which can be implemented using TensorFlow Probability [151]. Using TensorFlow also has the advantage of allowing vectorised (i.e. batched) inputs and computation performed on a graph which leads to significant speed-up when compared to the same computation performed using a standard library for modelling quantum systems, such as QuTiP [161]. Vectorised inputs refer to having the input to the differentiable model be an $n_\mathrm{b} \times n_\theta$ array for n_θ parameters and a batch of n_b different sets of parameter values, so that the output will be a $n_\mathrm{b} \times n_\mathrm{out}$ array, where n_out is the number of outputs from the model.

To demonstrate the effectiveness of our differentiable solver, we consider the case of a single quantum dot (SQD) coupled to left and right leads as discussed in Section 2.3. To model the steady state current flowing through the SQD at a given source-drain bias $V_\mathrm{bias} = \mu_l - \mu_r$ we solve a master equation of the form,

$$\dot{\rho} = \mathcal{L}\rho = -i[H_0, \rho] + \mathcal{L}_\mathrm{leads}\rho \tag{6.1}$$

where ρ is the density matrix of the SQD system, $\mathcal{L}$ is the Liouvillian superoperator, and $\mathcal{L}_\mathrm{leads}$ is the dissipator associated with the leads. As discussed in Section 2.3, in the weak-coupling regime $\mathcal{L}_\mathrm{leads}$ takes the form

$$\mathcal{L}_\mathrm{leads}\rho = -\Big(W_\mathrm{L}\mathcal{D}[c^\dagger]\rho + \overline{W}_\mathrm{L}\mathcal{D}[c]\rho + W_\mathrm{r}\mathcal{D}[c^\dagger]\rho + \overline{W}_\mathrm{R}\mathcal{D}[c]\rho\Big), \tag{6.2}$$

where the Lindblad superoperators act according to $\mathcal{D}[A]\rho = A\rho A^\dagger - 1/2\{A^\dagger A, \rho\}$. The energy dependent tunnel rates from a lead onto the dot are given by $W_\mathrm{L(R)} = \Gamma_\mathrm{L(R)} f_{l(r)}(\epsilon)$ and from the dot onto the lead $\overline{W}_\mathrm{L(R)} = \Gamma_\mathrm{L(R)}\Big[1 - f_{l(r)}(\epsilon)\Big]$, where ϵ is the electrochemical potential of the dot and $f_{l(r)}(\epsilon) = [e^{(\epsilon-\mu_{l(r)})/k_BT} + 1]^{-1}$ is the Fermi-Dirac distribution for the left(right) lead.

With e denoting the electronic charge and ρ_ss the steady state solution of Eq. (6.1), the steady state current flowing though the SQD is computed as

$$I_\mathrm{ss} = e\Big[\overline{W}_\mathrm{R}\mathrm{Tr}(\rho_\mathrm{ss}|1\rangle\langle 1|) - W_\mathrm{L}\mathrm{Tr}(\rho_\mathrm{ss}|0\rangle\langle 0|)\Big]. \tag{6.3}$$

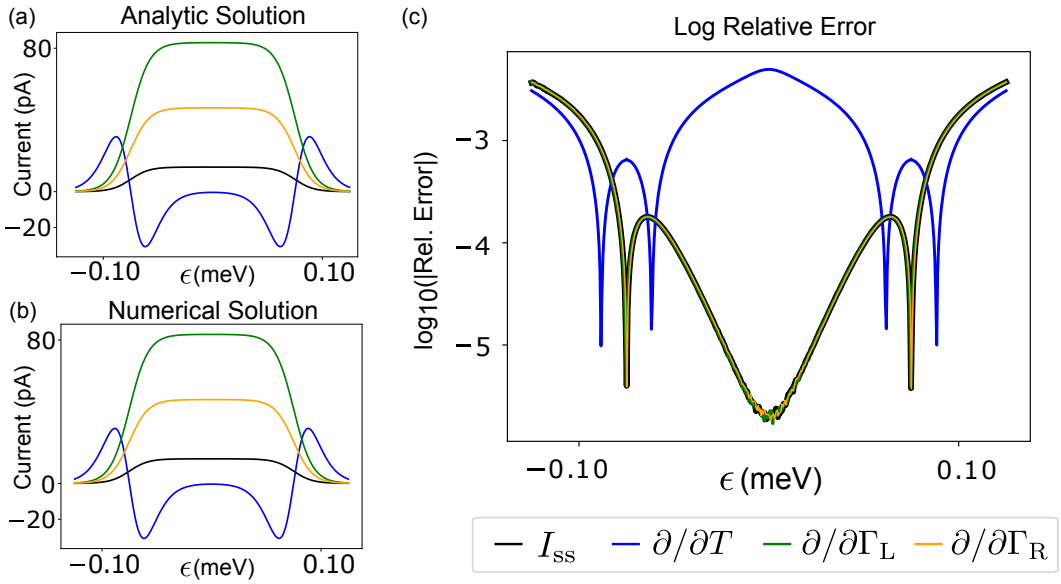

Figure 6.1: The steady state current and its derivatives using (a) analytic solutions and (b) the differentiable solver. Parameters are set as $\Gamma_L = 150$Hz, $\Gamma_R = 200$Hz, and $T = 100$mK. A quantitative comparison of the numerical outputs and analytic solutions is shown in (c) using the logarithm of the relative absolute error. All plots share the same legend.

This model has the benefit of a simple analytic solution for the steady state current which can be used to directly compare with the output and gradients generated by our solver. The steady state current is

$$I_{ss} = e\,\frac{W_L\overline{W}_R - \overline{W}_L W_R}{\Gamma_L + \Gamma_R} \tag{6.4}$$

with gradients with respect to Γ_L, Γ_R, and T being

$$\frac{\partial I_{ss}}{\partial \Gamma_L} = \frac{e\Gamma_R^2}{(\Gamma_L+\Gamma_R)^2}\Big[f_l(\epsilon) - f_r(\epsilon)\Big], \tag{6.5}$$

$$\frac{\partial I_{ss}}{\partial \Gamma_R} = \frac{e\Gamma_L^2}{(\Gamma_L+\Gamma_R)^2}\Big[f_l(\epsilon) - f_r(\epsilon)\Big], \tag{6.6}$$

$$\frac{\partial I_{ss}}{\partial T} = \frac{e\Gamma_L\Gamma_R}{\Gamma_L+\Gamma_R}\Big[\frac{\partial f_l(\epsilon)}{\partial T} - \frac{\partial f_r(\epsilon)}{\partial T}\Big], \tag{6.7}$$

where

$$\frac{\partial f_{l(r)}(\epsilon)}{\partial T} = \frac{\epsilon - \mu_{l(r)}}{k_B T^2}\cosh^{-2}\left(\frac{\epsilon-\mu_{l(r)}}{2k_BT}\right). \tag{6.8}$$

Values of I_{ss} and its derivatives computed using the differentiable solver are compared with the analytic results in Figure 6.1, displaying good agreement in relative error across the domain of dot energy ϵ. We use 32 bit precision for real

valued elements of the differentiable solver, with complex values defined using two 32 bit floats.

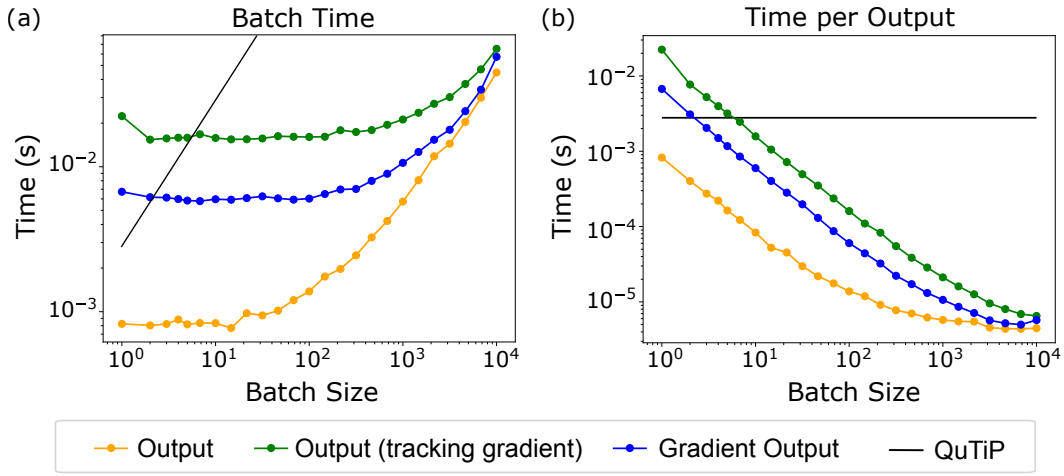

Figure 6.2: The total time (a) and the time per output (b) for computations on a range of batch sizes using the differentiable master equation for the single quantum dot model described in Eq. (6.1). Each point is an average of 100 evaluation times and the time per output is simply the total time divided by the batch size. Output refers to the time taken to compute the output of a batch of input parameters. To compute a gradient by automatic differentiation, a variable must be tracked during the output computation, and once the output is available the gradient can be evaluated. Both plots share the same legend. The black lines corresponding to QuTiP execution times are extrapolated from the time taken for a single computation.

Having established that our differentiable solver returns the desired values, we now investigate the speed of the model and how computation time scales with the batch size, n_b. The numerical results presented in Figure 6.1 were performed by sending a batch of $n_\mathrm{b} = 200$ parameter values with varying dot energy ϵ to our solver. We compare the evaluation of the output on the same hardware[1] with QuTiP, an established library for solving quantum master equations. As shown in Figure 6.2(a), our differentiable model computes batch outputs significantly faster than QuTiP (where batch computation scales linearly[2]) across all tested batch sizes. Tracking and evaluating gradients adds an overhead to computation time which is much more noticeable at low batch sizes. Considering the computation

[1]The processor used is a Intel(R) Core(TM) i5-9500 CPU. Tests with GPU hardware achieved similar performance.

[2]When computing steady state solution using the method outlined in Appendix E, QuTiP must evaluate each element of a batch sequentially when running on a single thread.

time per output, Figure 6.2(b) demonstrates the advantage of batched inputs with our solver where the time per output decreases to less than 10 μs. These fast computation times make our model ideal for computing a vector of outputs and evaluating the desired gradients.

6.2 Optimising Non-Differentiable Parameters

We aim to estimate values for parameters in quantum master equations such as Eq. (6.1) using ground truth data. We consider case studies of transport through a single quantum dot with an orbital excited state, and through a double quantum dot coupled to a phonon bath. A sketch of the parameter estimation process is shown in Figure 6.3(a) along with the case studies in (b) and (c). For both the single and double quantum dot case studies, the source-drain bias V_{bias} and a single 1D current scan are used to inform the parameter estimation. Not all parameters in a model may be differentiable as discussed below, and others may have minimal impact on a loss function so gradients become ineffective. We shall present our method for dealing with such parameters in general terms before presenting results for each case study.

We denote the n_{c} parameters which are controlled to produce a batch of n_{b} data points as $\boldsymbol{\theta}^{\text{c}}$, and the remaining n_{v} parameters under consideration for estimation as $\boldsymbol{\theta}^{\text{v}}$. The ground truth data is then $D = \{d_j | j = 1 \dots n_{\text{b}}\}$ and the total set of $n_\theta = n_{\text{c}} + n_{\text{v}}$ parameters is then $\boldsymbol{\theta} = [\boldsymbol{\theta}^{\text{c}}, \boldsymbol{\theta}^{\text{v}}]$. The output of a model is a function of these parameters, $f(\boldsymbol{\theta})$, which may not be differentiable with respect to certain elements of $\boldsymbol{\theta}$. In our case such parameters are the definition of the bias window in $\boldsymbol{\theta}^{\text{c}}$. In other situations, $f(\boldsymbol{\theta})$ may only have gradients in a small region of parameter space, which renders gradient descent methods impractical.

To circumvent the issue of a mixture of differentiable and non-differentiable parameters, we design an optimisation procedure which takes advantage of the fast differentiable model. The idea is to find the non-differentiable parameters for which the remaining differentiable parameters provide the best fit. A Nelder-Mead optimisation routine [162] finds appropriate values for the non-differentiable parameters, where the function being optimised is a fit of the model to ground

truth data using the remaining differentiable parameters. This fit first involves a log-spaced grid search of the differentiable elements of $\boldsymbol{\theta}^{\mathrm{v}}$ where the evaluation of $f(\boldsymbol{\theta})$ with the lowest loss with respect to the ground truth data is selected as a starting point for a short gradient descent optimisation using the Adam optimiser. The evaluation of the function being optimised by the Nelder-Mead routine is simply the final loss after this gradient descent. Finally, using the optimal non-differentiable parameters, conducting a longer gradient descent optimisation of the differentiable parameters provides an estimate of all parameters in $\boldsymbol{\theta}$. A schematic of this procedure is shown in Figure 6.3(d).

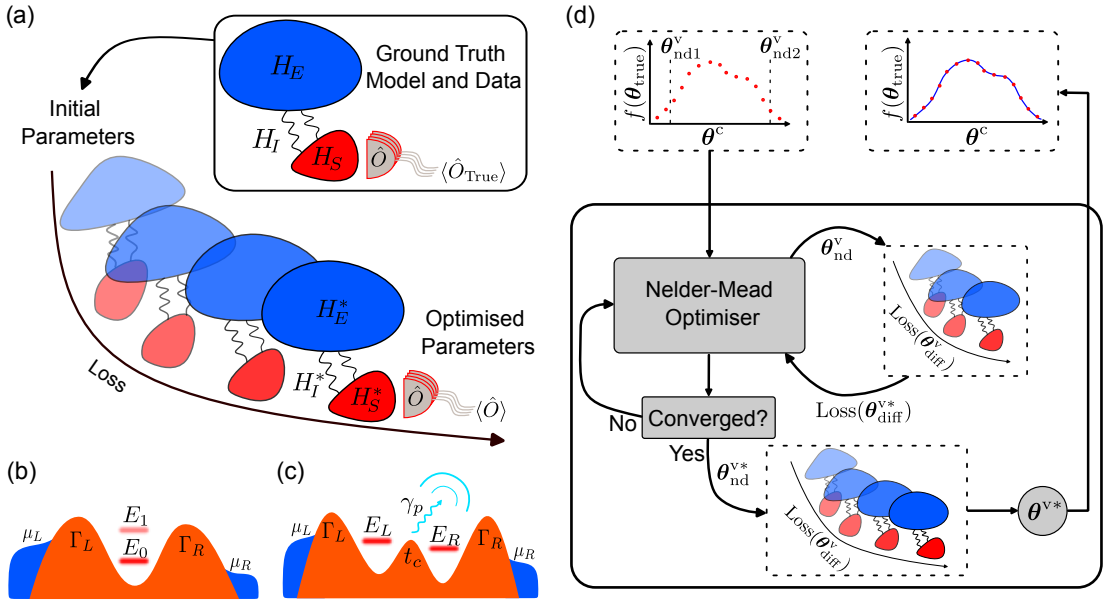

Figure 6.3: (a) An abstracted schematic of the process of estimating parameters of an open quantum system using gradient descent. Expectation values of an observable $\langle\hat{O}\rangle$ are generated from a ground truth model and a differentiable model is used to fit these values by gradient descent. (b) Representation of the first case study of a single quantum dot with an excited state coupled to left and right leads. (c) Representation of the second case study of a double quantum dot coupled to left and right leads, and a phonon bath. In each case study the observable used to inform parameter estimation is the steady state current from left to right lead. (d) A schematic of our approach for optimising differentiable and non-differentiable parameters when fitting to data. Here, we denote non-differentiable parameters as $\boldsymbol{\theta}^{\mathrm{v}}_{\mathrm{nd}}$ and differentiable parameters as $\boldsymbol{\theta}^{\mathrm{v}}_{\mathrm{diff}}$. Sets of optimised parameters are indicated with an asterisk.

The parameter fitting algorithm discussed above is general to the situation when some non-differentiable parameters must be optimised before optimising

differentiable parameters. In our case, the non-differentiable parameters define the energy scale of the measurement axis, which in turn defines how parameters such as tunnel rates change the profile of the fit. This is a result of dot electrochemical potentials being controlled by gate voltages in experiments, which do not have a well defined values relative to the bias window. In other experimental settings, it may be the case that the measurement axis is easily quantifiable (e.g. the frequency of an oscillating signal) and so the order in which differentiable and non-differentiable parameters are optimised becomes less important.

6.3 Bayesian Estimation of Differentiable Parameters

We assume that the ground truth data D is described by a function of the true parameters $f(\boldsymbol{\theta}_{\text{true}})$ with Gaussian noise of standard deviation σ such that each point in D is $d_j \sim \mathcal{N}(f(\boldsymbol{\theta}_{\text{true}}), \sigma)$. Under this assumption we formulate the likelihood of the measurement data given a set of parameters $\boldsymbol{\theta}^{\text{v}}$ used to estimate the function $\hat{d} = f(\boldsymbol{\theta}^{\text{v}})$ over the domain of $\boldsymbol{\theta}^{\text{c}}$ as

$$P(D|\boldsymbol{\theta}^{\text{v}}) \propto \exp\left(- \frac{\sum_{j=1}^{n_{\text{b}}} (\hat{d}_j - d_j)^2}{\sigma^2} \right). \tag{6.9}$$

This likelihood can be used in Bayes' formula $P(\boldsymbol{\theta}^{\text{v}}|D) \propto P(D|\boldsymbol{\theta}^{\text{v}})P(\boldsymbol{\theta}^{\text{v}})$ to estimate the posterior values for parameters in $\boldsymbol{\theta}^{\text{v}}$. The prior of each parameter in $\boldsymbol{\theta}^{\text{v}}$ can be chosen independently such that $P(\boldsymbol{\theta}^{\text{v}}) = \prod_{i=1}^{n_{\text{v}}} P(\theta_i^{\text{v}})$. The set of parameters which produce the mode of the posterior distribution is the maximum a posteriori (MAP) estimate, and for uniform priors this becomes maximum likelihood estimation (MLE). Evaluation of the negative log probability of the posterior distribution can be used as a differentiable loss function for the gradient descent portion of the parameter fitting process discussed in the previous section. The parameters which minimise this loss correspond to the MAP estimate.

Further to this, a Bayesian approach allows the use of Markov-chain Monte Carlo (MCMC) methods to estimate the posterior distribution for each parameter. We specifically consider Hamiltonian Monte Carlo (HMC) implemented in TensorFlow

Probability [151] to generate a set of n_s posterior samples for the parameter values $S = \{\boldsymbol{\theta}_j^{\mathrm{v}} | j = 1 \dots n_s\}$, using the MAP estimate as a seed to reduce burn-in.[3] These posterior samples allow for an estimate of uncertainty and correlations in the parameter values. The posterior distribution can also be normalised and used to update the prior distribution for use with further ground truth data.

6.4 Case Study: Single Quantum Dot with Orbital Excited State

Model

We model a single quantum dot with an orbital excited state as shown in Figure 6.3(b) such that the set of charge states correspond to a maximum of one excess charge on the dot. This restriction is motivated by the large charging energy of the quantum dot compared to the bias window and the energy splitting between the ground and first orbital excited state. The available charge states are $|0\rangle$, $|G\rangle$, and $|E\rangle$, where $|0\rangle$ has M charges on the dot, $|G\rangle$ has a single charge in the ground state, and $|E\rangle$ has a single charge in the orbital excited state. The Hamiltonian describing the coupling between these charge states and the leads is given by

$$H = H_0 + H_l + H_{el}, \tag{6.10}$$

$$H_0 = E_{\mathrm{g}}|G\rangle\langle G| + \Big(E_{\mathrm{g}} + \delta\Big)|E\rangle\langle E|, \tag{6.11}$$

$$H_l = \sum_k (\epsilon_k - \mu_s) d_{kl}^\dagger d_{kl} + (\epsilon_k - \mu_d) d_{kr}^\dagger d_{kr}, \tag{6.12}$$

$$H_{el} = \sum_k \sum_{j=g,e} (t_s d_{kl}^\dagger c_j + t_d d_{kr}^\dagger c_j + H.c.), \tag{6.13}$$

where E_{g} is the energy of the ground state, and δ is the energy splitting between the ground and orbital excited state. H_l describes the leads with $\mu_{l(r)}$ being the chemical potential of the left(right) leads, and $d_{kl(r)}^\dagger (d_{kl(r)})$ are the fermionic creation(annihilation) operators for the left(right) lead for the mode of energy ϵ_k. H_{el} describes the coupling between the dot states and the leads where $c_{g(e)}$ is the

[3] When starting from a random initial set of parameters, MCMC methods must run for a number of 'burn-in' steps to approach the region of parameter space close to higher posterior probabilities before accepting samples. Results in this chapter use 500 burn-in steps.

fermionic annihilation operator acting on the ground(excited) dot, and $t_{l(r)}$ are the tunnel couplings between the leads and the dot states. We assume the same tunnel rates to the leads for both the ground and excited charge state. We do not consider a relaxation rate from excited state to ground state as this rate does not always influence the steady state current [163]. The absence of such a rate can also be physically motivated by lead tunnel rates being faster than the relaxation process which may be the case in some experimental settings.

To model the steady state current flowing through the DQD at a given source-drain bias $V_{\text{bias}} = \mu_l - \mu_r$ we solve a master equation of the form,

$$\dot{\rho} = \mathcal{L}\rho = -i[H_0, \rho] + \mathcal{L}_{\text{leads}}\rho \tag{6.14}$$

where ρ is the density matrix of the SQD system, $\mathcal{L}$ is the Liouvillian superoperator, and $\mathcal{L}_{\text{leads}}$ is the dissipator associated with the leads. In the weak-coupling regime $\mathcal{L}_{\text{leads}}$ takes the form

$$\mathcal{L}_{\text{leads}} = \sum_{j=G,E} \Big\{ \Big(W_{sj} + W_{dj}\Big)\mathcal{D}[|j\rangle\langle 0|] \; + \Big(\overline{W}_{dj} + \overline{W}_{sj}\Big)\mathcal{D}[|0\rangle\langle j|] \Big\}, \tag{6.15}$$

where the Lindblad superoperators act according to $\mathcal{D}[A]\rho = A\rho A^\dagger - 1/2\{A^\dagger A, \rho\}$. The tunnel rates from a lead onto the dot are given by $W_{\text{L(R)}j} = \Gamma_{\text{L(R)}} f_{\text{L(R)}}(E_j)$ and from the dot onto the lead $\overline{W}_{\text{L(R)}j} = \Gamma_{\text{L(R)}}\Big[1 - f_{\text{L(R)}}(\epsilon_j)\Big]$, where $\Gamma_{\text{L(R)}} = \pi g_{\text{L(R)}}|t_{l(r)}|^2$ with $g_{\text{L(R)}}$ the constant density of states in the leads in the wide band approximation, and $f_{\text{L(R)}}(\epsilon) = [e^{(\epsilon-\mu_{l(r)})/k_BT} + 1]^{-1}$ is the Fermi-Dirac distribution for the left(right) lead.

With e denoting the electronic charge and ρ_{ss} the steady state solution of Eq. (6.14), the steady state current flowing though the SQD is

$$I = e \sum_{j=E,G} \overline{W}_{j\text{R}} \text{Tr}(\rho_{\text{ss}}|j\rangle\langle j|) - W_{j\text{R}} \text{Tr}(\rho_{\text{ss}}|0\rangle\langle 0|). \tag{6.16}$$

Results

We consider the model presented above as a case study to assess the performance of each part of the parameter estimation process. This model has a single controlled

parameter $\boldsymbol{\theta}^c = E_\mathrm{g}$ which is swept through the bias window. The variable parameters $\boldsymbol{\theta}^v = [\mu_l, \mu_r, \delta, \Gamma_\mathrm{L}, \Gamma_\mathrm{R}, T]$ can be separated into differentiable parameters $[\Gamma_\mathrm{L}, \Gamma_\mathrm{R}, T]$ and non-differentiable parameters $[\mu_l, \mu_r, \delta]$. The left and right chemical potentials are non-differentiable as they define the energy scale of the data before the model is computed, and the orbital excited state energy splitting δ has zero gradient for large areas of the parameter space and is thus optimised as a non-differentiable parameter.

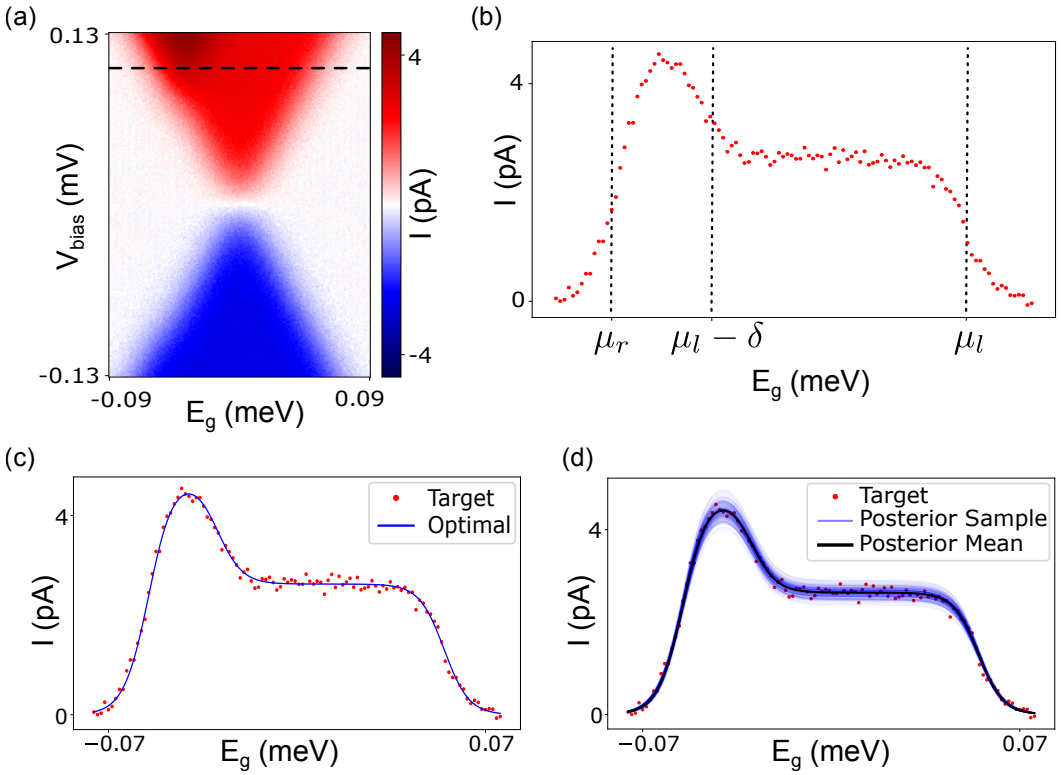

Figure 6.4: An example of our parameter estimation algorithm applied to a single quantum dot with an orbital excited state. (a) A Coulomb diamond from which the current trace in (b) is taken, indicated by the black dashed line. (b) The example ground truth simulated current data with 100 fA Gaussian noise used to fit parameters, with the bias set to 0.109 mV. Nominal locations of the points on the E_g axis defined by the non-differentiable parameters $[\mu_l, \mu_r, \delta]$ are indicated by vertical dashed lines. (c) The results of gradient descent parameter optimisation on $[\Gamma_\mathrm{L}, \Gamma_\mathrm{R}, T]$ after the non-differentiable parameters have been fitted. (d) The HMC posterior samples of the current values generated using 500 posterior samples of the parameters $[\Gamma_\mathrm{L}, \Gamma_\mathrm{R}, T]$. Ground truth and optimal parameter values, as well as posterior means with standard deviation errors for relevant parameters, are shown in Table 6.1.

An example of the parameter fitting process for a single quantum dot with an orbital excited state is shown in Figure 6.4 with parameter estimates shown

in Table 6.1. In this example, the largest absolute percentage error in optimised non-differentiable values is 1.2%, and in optimal differentiable values is 4.5%. Posterior means and standard deviations drift slightly further from the optimal parameter values, but retain a good fit. While a single example demonstrates the success of parameter fitting, we also consider the distributions of percentage errors for each parameter in Figure 6.5 for a set of 100 iterations of our parameter estimation algorithm on randomly generated data. The distributions are all peaked at zero percentage error which indicates that our parameter estimation method is generally effective. There are a small number of outliers with large errors, but upon further inspection we find that most of these examples have no discernible second peak in the current profile (see insets of Figure 6.5, specifically Outliers A, C, and D). This means the location of the excited state cannot be determined at the first optimisation step, which has consequences for the estimation of further parameters. We note that all the outliers have a lower signal to noise ratio than typical examples which may further impact the parameter estimation, as evident in Outlier B which does have an excited state peak. From Figure 6.5, we can also see that the parameter estimate using the posterior mean from HMC samples has a more narrow distribution around zero percentage error, and is therefore generally better than the gradient descent optimal values.

Parameter	Unit	Ground Truth	Optimal	Posterior Mean ± Std.
μ_l	pixels	15.41	15.25	-
μ_r	pixels	96.59	96.35	-
δ	meV	0.084	0.085	-
Γ_{L}	MHz	18.1	18.0	18.4 ± 0.8
Γ_{R}	MHz	183.1	180.6	171.3 ± 4.3
T	mK	55.9	53.4	59.4 ± 1.8

Table 6.1: Ground truth, optimal, and posterior means with standard deviation errors for the example shown in Figure 6.4. The non-differentiable parameters are not part of the HMC sampling and therefore do not have posterior means and uncertainties.

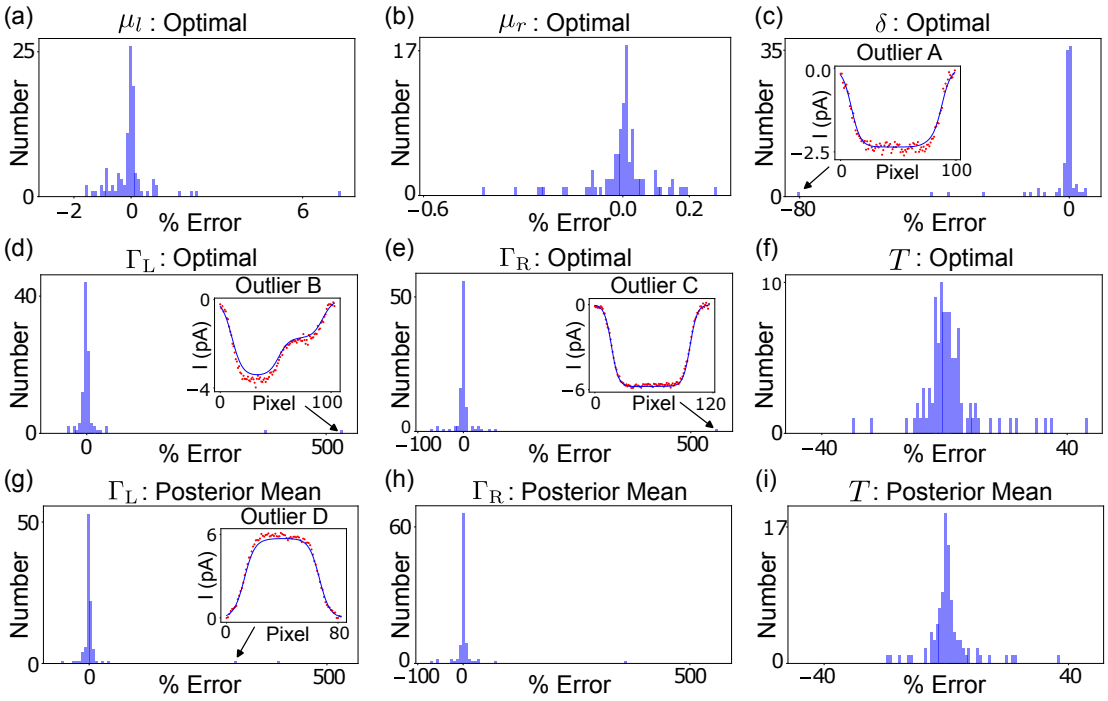

Figure 6.5: Distributions of parameter estimation absolute percentage errors over a test set of 100 randomly generated current traces for a single quantum dot with an orbital excited state. Distributions displayed are: (a)-(c) optimal values of non-differentiable parameters $[\mu_l, \mu_r, \delta]$, (d)-(f) optimal values of differentiable parameters $[\Gamma_L, \Gamma_R, T]$, and (g)-(i) posterior means for the differentiable parameters. All distributions are peaked at zero absolute % error, with a small number of outliers. Insets show the target (red points) and optimal fit (blue line) for selected outliers.

6.5 Case Study: Double Quantum Dot

Model

As discussed previously in this thesis, we model a double quantum dot coupled to left and right leads and a phonon bath as shown in Figure 6.3(c). The states describing the DQD are $|0\rangle$, $|L\rangle$, and $|R\rangle$ where $|0\rangle$ has (M, N) charges on the dot, $|L\rangle$ has $(M+1, N)$ charges, and $|R\rangle$ has $(M, N+1)$ charges. The Hamiltonian describing

the coupling between these charge states, the leads, and the phonon bath is given by

$$H = H_0 + H_l + H_p + H_{el} + H_{ep}, \tag{6.17}$$

$$H_0 = \frac{\epsilon}{2}\sigma_z + t_c\sigma_x, \tag{6.18}$$

$$H_l = \sum_k (\epsilon_k - \mu_l) d_{kl}^\dagger d_{kl} + (\epsilon_k - \mu_r) d_{kr}^\dagger d_{kr}, \tag{6.19}$$

$$H_p = \sum_{\mathbf{k}} \omega_{\mathbf{k}} a_{\mathbf{k}}^\dagger a_{\mathbf{k}}, \tag{6.20}$$

$$H_{el} = \sum_k (t_l d_{kl}^\dagger c_l + t_r d_{kr}^\dagger c_r + H.c.), \tag{6.21}$$

$$H_{ep} = \sigma_z \sum_{\mathbf{k}} \lambda_{\mathbf{k}} (a_{\mathbf{k}}^\dagger + a_{\mathbf{k}}), \tag{6.22}$$

where σ_μ are the Pauli operators in the subspace $|L\rangle$ and $|R\rangle$, $\epsilon = E_{\mathrm{L}} - E_{\mathrm{R}}$ is the detuning between the dot energy levels, and t_c is the interdot tunnel rate. H_l describes the leads with $\mu_{l(r)}$ being the chemical potential of the left(right) leads, and $d_{kl(r)}^\dagger (d_{kl(r)})$ are the fermionic creation(annihilation) operators for the left(right) lead for the mode of energy ϵ_k. H_{el} describes the coupling between the dots and the leads where $c_{l(r)}$ is the fermionic annihilation operator acting on the left(right) dot, and $t_{l(r)}$ are the tunnel couplings between the leads and the dots. The phonon bath is described by H_p where $a_{\mathbf{k}}^\dagger (a_{\mathbf{k}})$ are the creation(annihilation) operators for the phonon mode of angular frequency $\omega_{\mathbf{k}}$. The electron-phonon interaction is described by H_{ep} where $\lambda_{\mathbf{k}}$ is the coupling constant between the dots and the phonons.

To model the steady state current flowing through the DQD at a given source-drain bias $V_{\mathrm{bias}} = \mu_l - \mu_r$ we solve a master equation of the form

$$\dot{\rho} = \mathcal{L}\rho = -i[H_0, \rho] + \mathcal{L}_{\mathrm{leads}}\rho + \mathcal{L}_{\mathrm{phonons}}\rho, \tag{6.23}$$

where ρ is the density matrix of the DQD system, $\mathcal{L}$ is the Liouvillian superoperator, and $\mathcal{L}_{\mathrm{leads}}$ and $\mathcal{L}_{\mathrm{phonons}}$ are the dissipators associated with the leads and phonon bath respectively. In the weak-coupling regime $\mathcal{L}_{\mathrm{leads}}$ takes the form

$$\mathcal{L}_{\mathrm{leads}} = W_{\mathrm{L}}\mathcal{D}[|L\rangle\langle 0|] + \overline{W}_{\mathrm{L}}\mathcal{D}[|0\rangle\langle L|] + W_{\mathrm{R}}\mathcal{D}[|R\rangle\langle 0|] + \overline{W}_{\mathrm{R}}\mathcal{D}[|0\rangle\langle R|], \tag{6.24}$$

where the tunnel rates from a lead onto a dot are given by $W_{L(R)} = \Gamma_{L(R)} f_{L(R)}(E_{\mathrm{L(R)}})$ and from a dot onto the lead $\overline{W}_{L(R)} = \Gamma_{L(R)}\Big[1 - f_{L(R)}(E_{\mathrm{L(R)}})\Big]$ with $\Gamma_{L(R)} =$

$\pi g_{L(R)}|t_{L(R)}|^2$, where $g_{L(R)}$ is the constant density of states in the leads in the wide band approximation, and $f_{L(R)}(\epsilon) = [e^{(\epsilon-\mu_{L(R)})/k_BT}+1]^{-1}$ is the Fermi-Dirac distribution for the left(right) lead.

As discussed in Section 2.5, the phonon dissipator is most conveniently expressed in terms of the eigenstates of H_0, which for positive detuning are

$$|+\rangle = \cos(\theta/2)|L\rangle - \sin(\theta/2)|R\rangle, \tag{6.25}$$

$$|-\rangle = \sin(\theta/2)|L\rangle + \cos(\theta/2)|R\rangle, \tag{6.26}$$

with energy $\hbar\omega_\pm = \pm\sqrt{\epsilon^2/4+t_c^2}$. The energy splitting between the eigenstates is $\hbar\omega_p = \hbar(\omega_+ - \omega_-)$, and $\theta = \arctan(2t_c/\epsilon)$. The weak-coupling phonon dissipator is then,

$$\mathcal{L}_{\text{phonons}} = \gamma(\omega_p)\Big([1+n(\omega_p)]\mathcal{D}[|-\rangle\langle+|] + n(\omega_p)\mathcal{D}[|+\rangle\langle-|]\Big), \tag{6.27}$$

where $\gamma(\omega) = \sin^2\theta J(\omega)$ is the rate at which the phonon bath induces interdot charge transitions in the DQD, dictated by the phonon spectral density which we take as

$$J(\omega) = J_0\left(\frac{\omega}{\omega_d}\right)^{n-\alpha}\left[1-\text{sinc}\left(\frac{\omega}{\omega_d}\right)\right]e^{-\omega^2/2\omega_a^2}, \tag{6.28}$$

where $\omega_d = \frac{2\pi c}{d}$ and $\omega_a = \frac{2\pi c}{a}$, with d the centre-to-centre separation of the dots, a the length scale of the dots, and c the speed of sound in the crystal, and J_0 is a scale factor. We also have n as the dimension of the system and $\alpha = 0$ for piezoelectric coupling and $\alpha = 2$ for deformation potential coupling to phonons. The complete set of spectral densities for varying dimensions and coupling mechanism is shown in Table 2.1.

The Bose-Einstein occupation of the phonon bath $n(\omega) = [e^{\omega/k_BT}-1]^{-1}$ produces a temperature dependence on the phonon emission and absorption processes described by $\mathcal{D}[|-\rangle\langle+|]$ and $\mathcal{D}[|+\rangle\langle-|]$ respectively. As the DQD system is at low temperature ($T < 100$ mK and $k_BT \ll \omega_p$), phonon emission processes dominate.

With e denoting the electronic charge, using the steady state solution of Eq. (6.23), ρ_{ss}, the steady state current flowing though the DQD is

$$I = e\Big[\overline{W}_{\text{R}}\text{Tr}(\rho_{\text{ss}}|R\rangle\langle R|) - W_{\text{R}}\text{Tr}(\rho_{\text{ss}}|0\rangle\langle 0|)\Big]. \tag{6.29}$$

Results

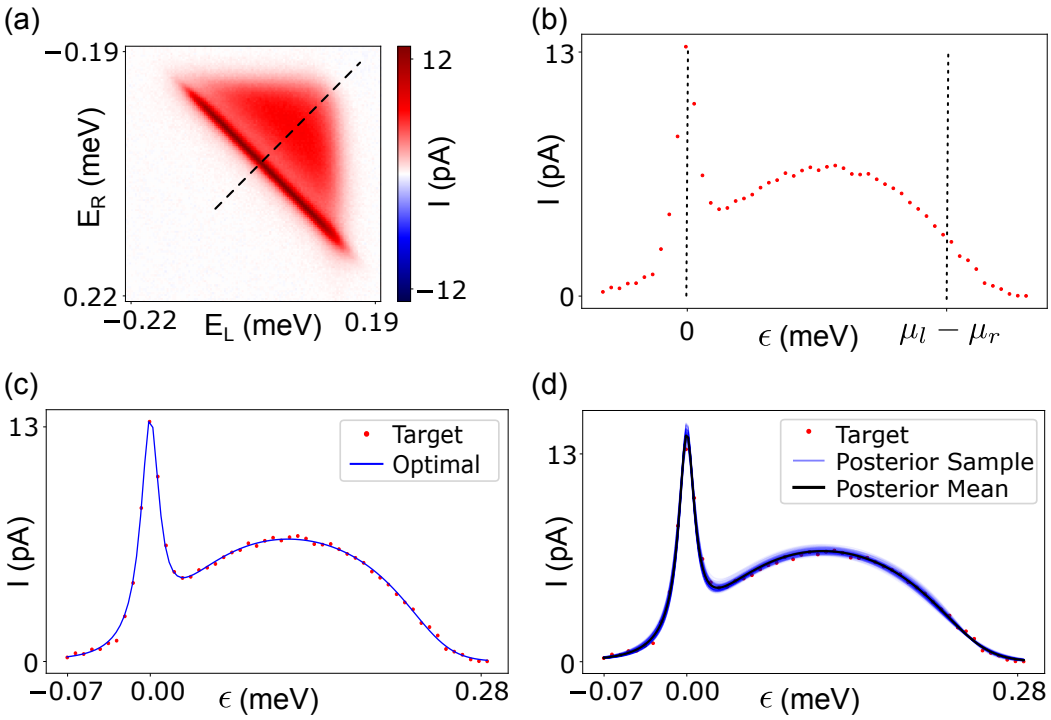

Figure 6.6: An example of our parameter estimation algorithm applied to a double quantum dot coupled to a phonon bath. (a) A bias triangle from which the current trace in (b) is taken, indicated by the black dashed line. (b) The example ground truth simulated current data with 100 fA Gaussian noise used to fit parameters, with the bias set to 0.241 mV. Nominal locations of the points on the E_g axis defined by the non-differentiable parameters $[\mu_l, \mu_r]$ are indicated by vertical dashed lines. (c) The results of gradient descent parameter optimisation on $[\Gamma_\mathrm{L}, \Gamma_\mathrm{R}, t_c, J_0, T]$ after the non-differentiable parameters have been fitted. (d) The HMC posterior samples of the current values generated using 500 posterior samples of the parameters $[\Gamma_\mathrm{L}, \Gamma_\mathrm{R}, t_c, J_0, T]$. We consider a 3-dimensional piezoelectric phonon spectral density with fixed parameters are $c_s = 3000$ ms^{-1}, $a = 20$ nm, and $d = 100$ nm. Ground truth and optimal parameter values, as well as posterior means with standard deviation errors for relevant parameters, are shown in Table 6.2

As for the previous case study, we consider the model presented above to assess the performance of our parameter estimation algorithm. This model has a single controlled parameter $\boldsymbol{\theta}^c = [\epsilon]$ which is varied such that each dot energy level is swept through the bias window. We choose the variable parameters to be $\boldsymbol{\theta}^v = [\mu_l, \mu_r, \Gamma_\mathrm{L}, \Gamma_\mathrm{R}, t_c, J_0, T]$ which can be separated into differentiable parameters $[\Gamma_\mathrm{L}, \Gamma_\mathrm{R}, t_c, J_0, T]$ and non-differentiable parameters $[\epsilon_0, \epsilon_\mathrm{bias}]$ which are the points where $\epsilon = 0$ and $\epsilon = \mu_\mathrm{L} - \mu_\mathrm{R}$ respectively. The remaining parameters are set to

representative fixed values of $c_s = 3000$ ms^{-1}, $a = 20$ nm, and $d = 100$ nm. We choose these parameters to be fixed as they can all be estimated from the device design. The dot radius a in particular has minimal impact on the fit for the energy scales probed by typical experimental measurements. These parameters can also be included in the set of differentiable parameters.

Parameter	Unit	Ground Truth	Optimal	Posterior Mean ± Std.
ϵ_0	pixels	10.37	10.29	-
ϵ_{bias}	pixels	45.53	45.61	-
Γ_{L}	MHz	854.1	127.0	126.2 ± 5.4
Γ_{R}	MHz	166.4	529.5	540.9 ± 38.2
t_c	GHz	1.485	0.912	0.940 ± 0.041
J_0	GHz	0.981	3.18	2.96 ± 0.3
T	mK	143.7	136.5	126.1 ± 24.7

Table 6.2: Ground truth, optimal, and posterior means with standard deviation errors for the example shown in Figure 6.6. The non-differentiable parameters are not part of the HMC sampling and therefore do not have posterior means and uncertainties.

An example of the parameter fitting process for a double quantum dot coupled to a phonon bath is shown in Figure 6.6 with parameter estimates shown in Table 6.2. Despite the fit to data points being accurate, we see much less convincing estimates of each parameter, particularly the differentiable parameters, when compared to performance in the previous case study. This example is representative of other fits, so we conclude that there are too many parameters with compensating effects to fit the true model for a single current trace along the detuning axis.[4]

Despite this apparent failure to fit parameters to a current scan along the detuning axis of a double quantum dot, we make use of our algorithm to gain insight into the interaction of the double quantum dot with phonons. Since the fit remains accurate, albeit with inaccurate parameter estimations, we use our fitting process to perform model selection on the phonon spectral density. It may be the case that we are unsure whether a device has deformation potential or piezoelectric coupling as the dominant phonon coupling mechanism, in which case using a detuning trace to determine the correct model would be useful. It is also

[4]We refer to the quote, "With four parameters I can fit an elephant, and with five I can make him wiggle his trunk," attributed to John von Neumann.

interesting to consider the dimensionality of the phonon spectral density as even in a bulk 3D device, the formation of quantum dots at a thin layer of the heterostructure could potentially act to confine phonons in 2D.

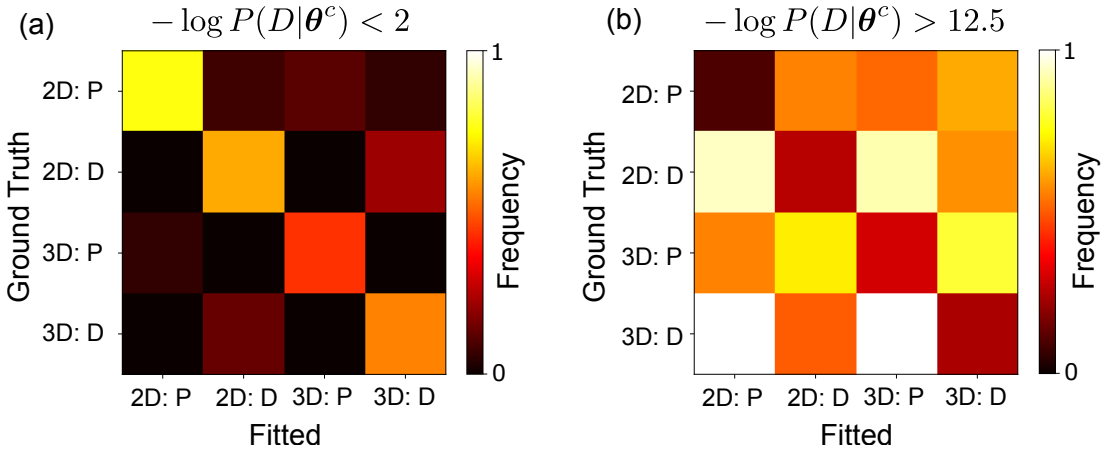

Figure 6.7: The occurrence of fits which have a negative log likelihood of (a) less than 2, and (b) greater than 12.5 in a test set of 50 for each ground truth model. In each ground truth model a different phonon spectral density is used, with "3D: D" being 3-dimensional deformation potential, "3D: P" 3-dimensional piezoelectric, "2D: D" 2-dimensional deformation potential, and "2D: P" 2-dimensional piezoelectric. With Gaussian noise, $-\log P(D|\boldsymbol{\theta}^c) < 2$ indicates that the average error is less than 2 noise standard deviations from the ground truth which we consider to be a good fit. Fits with $-\log P(D|\boldsymbol{\theta}^c) > 12.5$ indicates that the average error is more than 5 noise standard deviations, representing a failure of fitting. We fit the non-differentiable parameters $[\epsilon_0, \epsilon_{\text{bias}}]$ and the differentiable parameters $[\Gamma_{\text{L}}, \Gamma_{\text{R}}, t_c, J_0, T]$. Fixed parameters are $c_s = 3000\text{ms}^{-1}$, $a = 20\text{nm}$, and $d = 100\text{nm}$.

In Figure 6.7 we present the results of performing our fitting process with each phonon spectral density (2D and 3D deformation potential, 2D and 3D piezoelectric) on datasets with different ground truth spectral densities. We use the negative log likelihood, $-\log P(D|\boldsymbol{\theta}^c)$, as a metric for our fit. As the data has Gaussian noise, the value of the negative log likelihood indicates the number of noise standard deviations a given fit is from the true value. In Figure 6.7(a) we display the frequency of fits which are within two standard deviations of the true value on average. Having the largest values along the diagonal indicates that our fit is only successful when the correct model is used. This seems in contrast to the findings of Figure 6.6, whereby the model successfully fitted the data with incorrect parameters, but we now have evidence that the functional form of the spectral density adds a

significant constraint on the fit. The failed fits which are on average more than five standard deviations from the true value are shown in Figure 6.7(b), and in this case the diagonal has the lowest values indicating that the fitting process does not fail often when using the correct model. We can also observe from this plot that the fitting process is notably worse when fitting piezoelectric spectral densities to data with deformation potential spectral densities, and also performs poorly when fitting deformation potential spectral densities to data generated using piezoelectric spectral densities in 3D. Fits which are between 2 and 5 standard deviation of the ground truth could still be determined successful, but may be more subjective so we do not consider them useful when assessing our fitting of different spectral densities.

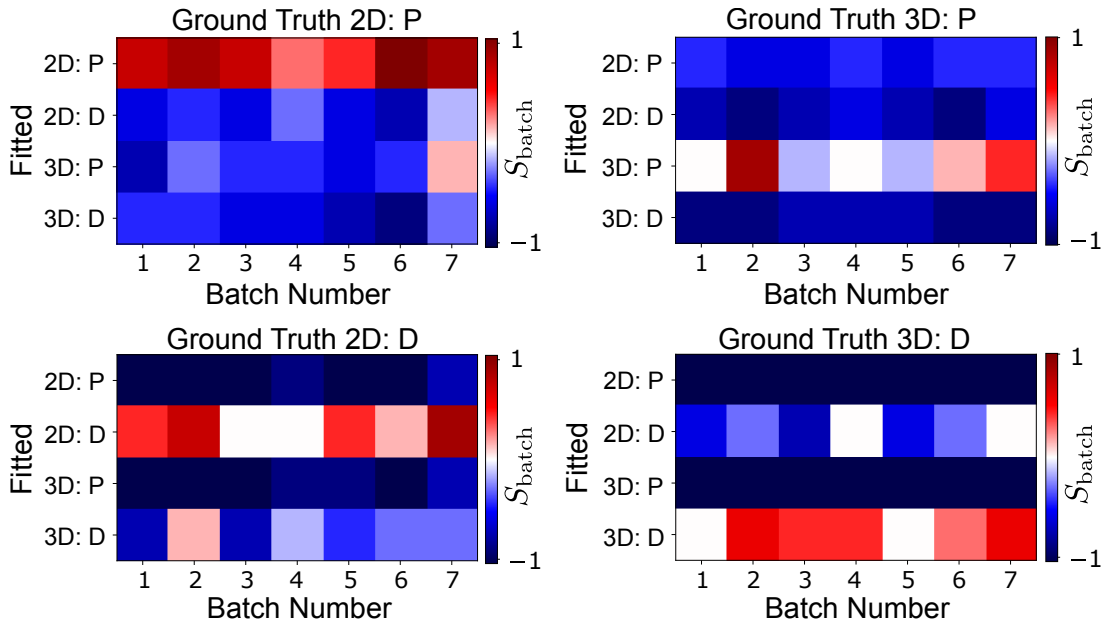

Figure 6.8: The score of fitting to a batch of size $n_{\text{batch}} = 7$ for each phonon spectral density considered in Figure 6.7. The batch score $S_{\text{batch}} = (n_{\text{success}} - n_{\text{failure}})/n_{\text{batch}}$ for seven independent batches is plotted for each fitted spectral density. A positive score indicates that the spectral density fit succeeds more than it fails within the batch, in accordance to the definitions of success and failure discussed in the text. We see that the best scores for each batch correlate with the ground truth spectral density.

We conclude that our fitting process provides useful insight into the electron-phonon coupling mechanism in a double quantum dot system. In order to apply this strategy to real data where the ground truth is not available, using a batch of size n_{batch} detuning traces from different bias triangles allows a choice of model to

be made given the frequencies of fit outcomes displayed in Figure 6.7. Defining a score function $S_{\text{batch}} = (n_{\text{success}} - n_{\text{failure}})/n_{\text{batch}}$ where n_{success} is the number of fits in a batch with $-\log P(D|\boldsymbol{\theta}^c) < 2$ and n_{failure} is the number of fits in a batch with $-\log P(D|\boldsymbol{\theta}^c) > 12.5$ provides reliable insight into the correct phonon coupling mechanism for simulated test data as shown in Figure 6.8 which considers the case of $n_{\text{batch}} = 7$.

6.6 Time Evolution

Having considered parameter estimation using steady state solutions to quantum master equations using our differentiable solver, this section briefly explores time-evolution functionality and its limitations. We consider the model of a double quantum dot coupled to fermionic leads and a phonon bath outlined above, as this can also be interpreted as a charge qubit [164, 165]. The evolution of the density matrix is determined by the Liouvillian superoperator $\mathcal{L}$, and a Lindblad master equation can be easily recast as a set of coupled ordinary differential equations (ODEs) (see Appendix E) which means standard ODE solvers can be used. Our solver implements a 4^{th} order Runge-Kutta method [166] to compute time-dynamics. To verify that our solver is accurate, Figure 6.9 shows that the steady state solution is reached after a suitable evolution time under the influence of a time-independent Hamiltonian. This figure also demonstrates batch computation of time-evolution, whereby a batch of $n_{\text{b}} = 250$ detuning values is evolved from an initial state of $|\psi(0)\rangle = (|0\rangle + |L\rangle + |R\rangle)/\sqrt{3}$ over 15 ns for 1500 time steps in 0.38s using the same hardware as in Figure 6.2.

In addition to evolution under a time-independent Hamiltonian, our solver can handle time-dependent Hamiltonians. We demonstrate this functionality by considering a Rabi pulse sequence on the DQD system operating as a charge qubit, with the details and results of this pulse sequence shown in Figure 6.10. We initialise the DQD such that the charge is on the left dot, with its electrochemical potential remaining below the source and drain chemical potentials for the duration of the sequence. The electrochemical potential of the right dot is pulsed by an energy $\delta\epsilon$

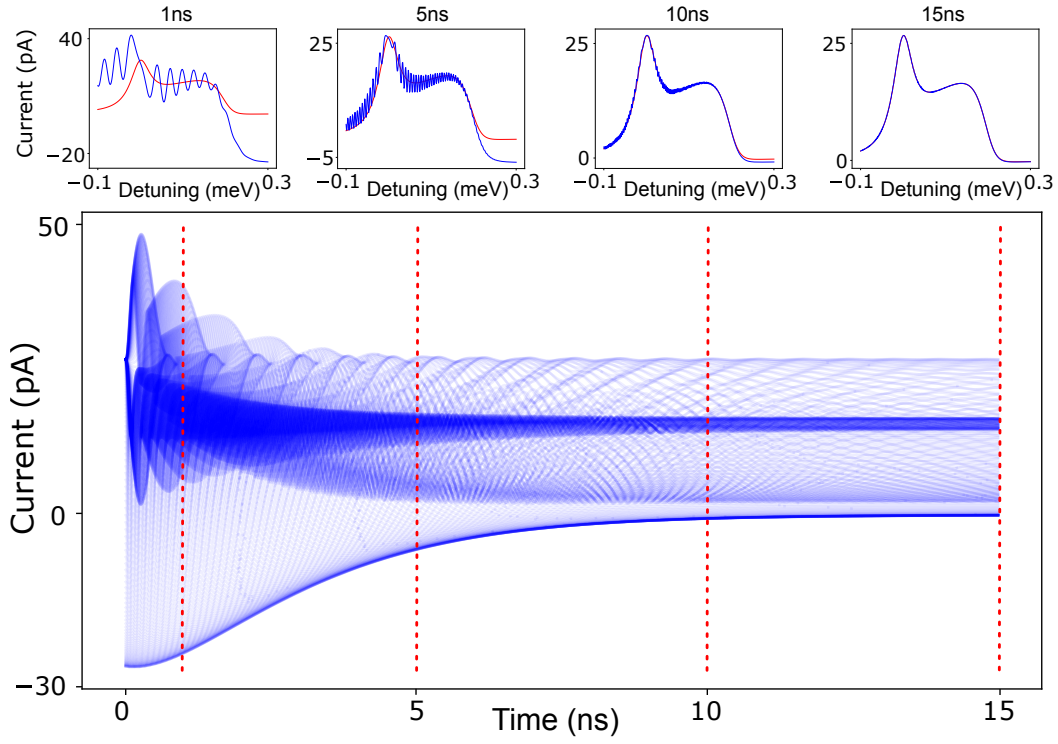

Figure 6.9: The time-evolution of a double quantum dot system coupled to left and right leads and a phonon bath with a time-independent Hamiltonian. The upper plots display the current as a function of detuning at several points along the evolution, with the steady state current (red) shown for comparison. The evolution is computed as a batch of $n_\mathrm{b} = 250$ detuning values and evolved for 15 ns with a step-size of 0.01 ns. The initial state for the entire batch is the pure state, $|\psi(0)\rangle = (|0\rangle + |L\rangle + |R\rangle)/\sqrt{3}$. Parameter values used are, $V_\mathrm{bias} = 0.2$ mV, $\Gamma_\mathrm{L} = \Gamma_\mathrm{R} = 500$ MHz, $t_c = 4$ GHz and $T = 100$mK. The phonon coupling follows a 3D piezoelectric spectral density with $c_s = 3000$ ms^{-1}, $a = 20$ nm, and $d = 50$nm, and $J_0 = 1$ GHz.

for a duration τ_p which defines the Rabi pulse. We then simulate the integration of current for a duration of τ_m and output the mean current during this period. In relation to our solver, we note that gradients with respect to pulse parameters do not function, and therefore further work would be required to implement a differentiable model for optimal quantum control.

The charge qubit Rabi chevrons in Figure 6.10 display some interesting features. Most notably, the amplitude of the oscillations is asymmetric about the point of zero pulse detuning. This has been observed experimentally and attributed to finite rise-times of pulses [165]. In our model, we consider ideal square pulses which implies that this is not the case. In fact, Ref [167] demonstrates an analytic result

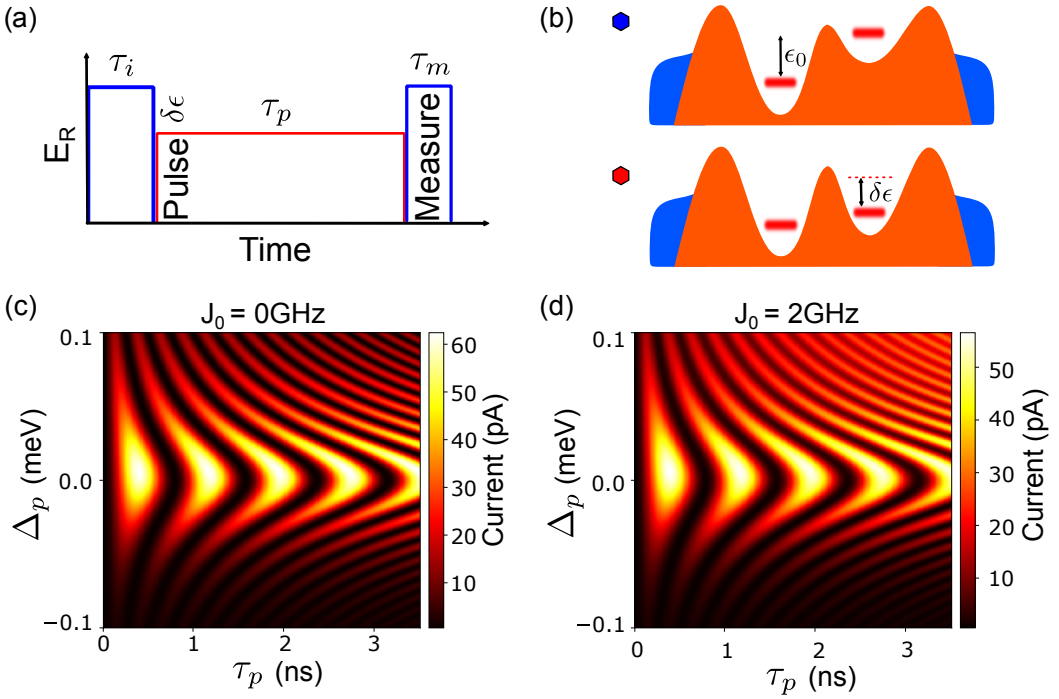

Figure 6.10: Demonstration of a Rabi pulse sequence on a DQD charge qubit computed using our quantum master equation solver. (a) Outline of the sequence whereby the DQD is initialised to be $|\psi(0)\rangle = |L\rangle$ and after a time $\tau_i = 1$ ns a pulse is applied to the right dot to vary the detuning by $\delta\epsilon$ for a duration of τ_p, and current is measured for a time $\tau_m = 1$ ns. (b) Schematics of the DQD in the initialisation and measurement regime (top and the pulsed regime (bottom). Rabi chevrons without (c) and with (d) coupling to a phonon bath. We define the pulse detuning $\Delta_p = |\delta\epsilon| - |\epsilon_0|$ and the measured current is taken to be the mean current integrated during the measurement period. Parameter values used are, $\Gamma_L = \Gamma_R = 500$ MHz, $t_c = 4$ GHz and $T = 100$ mK. The phonon coupling follows a 3D piezoelectric spectral density with $c_s = 3000$ ms^{-1}, $a = 20$ nm, and $d = 50$ nm, and $J_0 = 1$ GHz.

explaining this asymmentry as a result of finite coherences between the dot states; even when the dot is strongly localised on the left dot at initialisation, the Rabi oscillations occur between the system Hamiltonian eigenbasis as defined in Eq (6.25) and thus a there is a small superposition of initialisation in the qubit excited state. A further asymmetry is added to the Rabi chevron when considering the influence of phonons which enhances exchange from left to right dot state at positive pulse detunings, with the consequence of also inducing decoherence as shown in Figure 6.10(d). Successfully reproducing the expected charge qubit dynamics under time-independent and time-dependent Hamiltonians is a demonstration that our 4$^{\text{th}}$ order Runge-Kutta solver is sufficient for the phenomena considered, however more

sophisticated solvers could make computation of dynamics more efficient [166].

6.7 Discussion

In this chapter we have presented a fast and differentiable quantum master equation solver. We have demonstrated its capability to compute steady state solutions and time evolution of open quantum systems with a specific focus on transport through quantum dots. Our solver can be applied to any system described by a Lindblad master equation, and minimal changes would permit application to a more general weak-coupling approach involving fewer approximations. The speed of our solver comes from its capability to compute a batch of outputs in a single evaluation of a model. This speed in turn facilitates more involved algorithms requiring many computations, which would be impractical using standard solvers. An example of such an algorithm is the parameter estimation algorithm we develop which employs both gradient-based and gradient-free optimisation, and MCMC methods.

We have applied our parameter estimation algorithm to case studies of transport through a single quantum dot with an orbital excited state, and a double quantum dot coupled to a phonon bath. We find that our algorithm is successful for the case of a single quantum dot, but fails to find the correct parameter values for the double quantum dot. We do not attribute this to a fundamental failure of the algorithm as the fits remain close to the ground truth, but rather to an under-defined problem in which there are too many parameters to uniquely fit the data. A better estimate of parameters could be achieved by considering further data, such as a current trace along the baseline of a bias triangle. We investigate the possibility of performing model selection using our algorithm, specifically considering the electron-phonon coupling mechanism in a double quantum dot and find that it is possible to reliably determine the ground truth spectral density. Our approach could be directly applied to experimental studies of the spectral density, such as in Chapter 3. Decoherence from electron-phonon interactions impacts both charge and spin qubits, therefore characterising the details of this coupling mechanism is important for understanding qubit dynamics.

7 Conclusion

This thesis has approached the inference of electrostatic quantum dot device characteristics by probing transport phenomena from experimental and theoretical perspectives. We have combined these perspectives with machine learning in a range of transport regimes, and uncovered otherwise inaccessible details of electrostatic disorder. Particular attention was paid to the theory of electron-phonon interactions since it is required to explain transport measurements in a double quantum dot, as outlined in Chapter 2 and explored in Chapters 3 and 6.

The results in Chapter 3 took a more traditional approach to inferring parameters from experimental data, but used analysis of single-charge tunnelling events to estimate current. We presented sub-attoampere currents through a double quantum dot in Ge/SiGe, inferred tunnel rates in the Hertz range, and observed evidence of phonon assisted transport. This work lays the foundation for a direct comparison of the phonon coupling mechanism in Ge/SiGe with other material systems. Being able to resolve single-charge tunnel events through a double quantum dot also has potential applications in thermodynamics where repeated charge transition events may represent the stochastic ticks of a quantum clock [168].

The transport regime of an electrostatic quantum dot device varies depending on the region of gate voltage space in which it is operated. In Chapter 4 we presented a machine learning accelerated model which facilitates the rapid determination of

the transport regime of a device, namely whether the transport channel is open or closed, and the number of quantum dots formed. This information is vital for coarse tuning of devices to the regime required for more detailed transport measurements such as those presented in Chapter 3. Having developed this model into a virtual device and discussed the requirements for a broader scope of physical simulation, we anticipate that such simulations will become paramount to testing the tuning and control algorithms necessary for the future of scalable quantum computing in electrostatic quantum dots [58–65].

The machine learning accelerated model was applied to a physics-aware machine learning algorithm in Chapter 5. Using simple transport measurements, this algorithm was able to infer disorder potentials in a GaAs device which were effective in narrowing the reality gap between simulation and experiment. The primary source of disorder was modelled as the presence of silicon donor ions, but the algorithm can easily adapt to alternative sources of disorder by considering an appropriate model. This flexibility means that our algorithm can be readily applied to different devices, and characterising disorder is key to understanding larger arrays of devices and how features vary over a wafer [124]. The ability to characterise disorder across larger devices would provide invaluable insight into fabrication processes and help accelerate quantum dots as a platform for quantum computing.

Following the theme of accelerated models and inferring device parameters from transport data, we developed a fast and differentiable quantum master equation solver in Chapter 6. Such a solver for steady state solutions has not been presented previously, and we have used our solver as part of a parameter estimation algorithm when considering transport through quantum dots. We demonstrate the capability of our solver to compute steady state solutions as well as time evolution under the influence of time-independent and time-dependent Hamiltonians. We considered two case studies for our parameter estimation algorithm: a single quantum dot with an orbital excited state, and a double quantum dot coupled to a phonon bath. In the instance of a double quantum dot, we demonstrated the utility of our algorithm by developing a model selection process to determine the dominant phonon coupling

mechanism from noisy simulated current values. While our study was performed on simulated data, which was necessary to compare to known true parameter values, we have designed our parameter estimation algorithm to be readily applied to experimental data. This could find utility in determining device characteristics, such as tunnel rates and temperature, from standard transport measurements. The selection of electron-phonon coupling mechanisms could also prove useful for experimental studies such as those performed in Ref. [112] and Chapter 3.

This thesis has demonstrated several approaches to enhance our capability to probe, understand, and scale electrostatic quantum dot devices across a range of transport regimes. Analysing single-charge tunnelling events allowed us to experimentally probe a double quantum dot in the slow tunnel rate regime. Using the boundary separating open and closed channel transport and a machine learning accelerated model, we inferred the hidden electrostatic disorder potential. Developing a fast and differentiable quantum master equation solver allowed integration with machine learning techniques, with applications to a parameter estimation algorithm to study transport in single and double quantum dots. The interlinked use of theory, experiment, and machine learning has proven key to results in this thesis, and similar approaches could refine our understanding of many other physical phenomena in future.

Appendices

A

Device Preparation and Control

This appendix outlines the practical details of how experimental measurements are taken, beginning with sample preparation, followed by the associated control electronics. The experimental data presented in this thesis came from two devices: in Chapter 3 from a Ge/SiGe based device from the Katsaros group at IST Austria, and in Chapter 5 from a GaAs device from the Zümbuhl group at the University of Basel. The measurements were taken at the University of Oxford.

A.1 Sample Preparation

Before measurements can be taken, a sample must be attached to a sample board which interfaces the device with signals sent to it. The sample is fixed in place using polymethyl methacrylate (PMMA) which is a suitable adhesive due to it being strong enough to hold the sample in place, but weak enough for the sample to remain intact upon removal. Metallic gate electrodes on the device are then electrically connected to pads on the sample board using a wire bonder. Certain sample board pads will have different connectivity capabilities, and as we may wish to send DC and AC signals to the device through different fridge lines, the connections must be chosen accordingly during bonding. Once the sample has been bonded, the sample board can be loaded into a puck for insertion into a dilution

refrigerator. A dilution refrigerator will typically operate at a base temperature of 20mK, but care must be taken in thermalising the sample with the puck and minimising power dissipation near the sample from incoming signals.

A.2 Classical Electronics

Signals are sent to and from the sample using classical electronics in order to control and measure the device. All DC lines exit the top of the dilution refrigerator and are connected to a 48 channel breakout box via a fisher cable. Each DC line has a BNC connector on the breakout box which can be set to grounded or floating. A 16 channel 16-bit digital to analogue converter (DAC) is used to generate the voltage applied to the DC lines. Each channel of the DAC has a 4V range and can be operated in positive, negative, or bipolar mode. Different samples require different voltage ranges, for example electron based depletion mode quantum dot devices need negative voltages to control while the equivalent hole based device would need positive voltages. The 16-bit channels have a voltage resolution of 60μV but voltage dividers can be used to achieve finer resolution, with typical divider ranges being from $\frac{1}{1000}\frac{V}{V}$ to $\frac{1}{100}\frac{V}{V}$. The DAC is controlled from a PC in the laboratory with communications being sent via a fibre-optic cable. The DAC voltages can be changed on a timescale of 10ms. To measure the current flowing through a device, the drain is connected to a current amplifier which converts the current to a voltage with an adjustable amplifier gain which is set to $1 \times 10^{-9}\frac{A}{V}$.

B

Phonon Spectral Density for a Double Quantum Dot

This appendix considers the functional form of the phonon spectral density experienced by a double quantum dot as discussed in Chapter 2 and considered in the results presented in Chapter 6.

B.1 Coupling Matrix Element

We assume a single excess electron in a double quantum dot system and define a basis of $\{|L\rangle, |R\rangle\}$ corresponding to the electron occupying the left and right dot respectively. This is a two-level system which can be mapped to the spin-boson Hamiltonian as shown in Eq. (2.59).

The interaction Hamiltonian can be shown to have a diagonal (σ_z) system operator by considering well defined quantum dots with minimal overlap of the dot wavefunctions, i.e. $\langle L|R\rangle \ll 1$. Using the single particle wavefunctions, the phonon coupling matrix element $\lambda_{\mathbf{k}}$ is defined as,

$$\begin{aligned}\lambda_{\mathbf{k}} &= M_{\mathbf{k}}\Big(\langle L|e^{i\mathbf{k}\cdot\mathbf{r}}|L\rangle - \langle R|e^{i\mathbf{k}\cdot\mathbf{r}}|R\rangle\Big) \\ &= M_{\mathbf{k}}\int d\mathbf{r}\Big[|\psi_L(\mathbf{r})|^2 - |\psi_R(\mathbf{r})|^2\Big]e^{i\mathbf{k}\cdot\mathbf{r}}.\end{aligned} \tag{B.1}$$

Adopting the notation $\mathbf{k} = (\boldsymbol{\kappa}, k_z)$ and $\mathbf{r} = (\boldsymbol{\rho}, r_z)$, we assume the dots exist in the x-y plane and have identical, radially symmetric wavefunctions separated by

a vector $\mathbf{d}$ such that $\psi_L(\boldsymbol{\rho}, r_z) = \psi(\boldsymbol{\rho}, r_z)$ $\psi_R(\boldsymbol{\rho}, r_z) = \psi(\boldsymbol{\rho} - \mathbf{d}, r_z)$ we find

$$\lambda_{\mathbf{k}} = M_{\mathbf{k}}\Big(1 - e^{i\boldsymbol{\kappa}\cdot\mathbf{d}}\Big)|\tilde{\psi}(\boldsymbol{\kappa}, k_z)|^2. \tag{B.2}$$

B.2 Angular Form Factor

Recalling the definition of the spectral density, $J(\omega) = \sum_{\mathbf{k}} |\lambda_{\mathbf{k}}|^2 \delta(\omega - \omega_{\mathbf{k}})$, we can derive the form factor for $J(\omega)$. We use a linear dispersion relation, $\omega_k = c|\mathbf{k}| = ck$ where c is the speed of sound in the crystal, and omit the prefactor $M_{\mathbf{k}}$ to find the angular form factor, $F(\omega)$, based on the dot geometry,

$$F(\omega) = \sum_{\mathbf{k}} \delta(\omega - ck)|\tilde{\psi}(\kappa, k_z)|^4 |1 - e^{i\boldsymbol{\kappa}\cdot\mathbf{d}}|^2. \tag{B.3}$$

We convert the sum over wavevectors to a 3D integral, $\sum_{\mathbf{k}} \to \frac{v}{(2\pi)^3}\int d\mathbf{k}$. Using the Jacobi-Anger expansion we can identify

$$\begin{aligned} |1 - e^{i\boldsymbol{\kappa}\cdot\mathbf{d}}|^2 &= 2[1 - \cos(\kappa d\cos\phi)] \\ &= 2[1 - J_0(\kappa d)] - 4\sum_{n=1}^{\infty}(-1)^n J_{2n}(\kappa d)\cos 2n\phi, \end{aligned} \tag{B.4}$$

where $J_0(\cdot)$ is the zeroth order Bessel function of the first kind, and the infinite sum reduces to zero after performing the azimuthal integral over ϕ. We then have

$$\begin{aligned} F(\omega) &= \frac{v}{2\pi^2}\int_0^{\pi}\int_0^{\infty} \delta(\omega - ck)|\tilde{\psi}(\kappa, k_z)|^4 [1 - J_0(\kappa d)]k^2 \sin\theta dk d\theta \\ &= \frac{v\omega^2}{2\pi^2 c^3}\int_0^{\pi} \left|\tilde{\psi}\Big(\frac{\omega}{c}\sin\theta, \frac{\omega}{c}\cos\theta\Big)\right|^4 \Big[1 - J_0\Big(\frac{\omega d}{c}\sin\theta\Big)\Big]\sin\theta d\theta. \end{aligned} \tag{B.5}$$

Changing variables to $x = \cos\theta$ and observing that the integral only depends on the magnitude of the wavevector we have,

$$F(\omega) = \frac{v\omega^2}{\pi^2 c^3}\int_0^1 \left|\tilde{\psi}\Big(\frac{\omega}{c}\sqrt{1-x^2}, \frac{\omega}{c}x\Big)\right|^4 \Big[1 - J_0\Big(\frac{\omega d}{c}\sqrt{1-x^2}\Big)\Big]dx. \tag{B.6}$$

To simplify this integral we assume a sharply peaked electron density, then the Fourier transformed wavefunction tends to unity. In the context of a double quantum dot system this is a reasonable assumption as the dots are usually confined to a narrow region of space in all directions. The finite extent of the dot wavefunctions leads to a cutoff frequency $\omega_a \approx c/a$ for phonon interactions,

where a is the length scale of the dot. This cutoff can be modelled as a Gaussian exponential decay of the spectral density, related to the Fourier transform of a Gaussian wavefunction in the spatial domain.

Finally, we make use of the integral $\int_0^z J_0(\sqrt{z^2-x^2})dx = \sin z$ and the assumption $|\tilde{\psi}(\boldsymbol{\kappa}, k_z)|^4 \approx 1$ to evaluate the angular form factor of the spectral density as

$$F(\omega) = \frac{v}{\pi^2 c d^2}\left(\frac{\omega}{\omega_d}\right)^2\left(1-\operatorname{sinc}\frac{\omega}{\omega_d}\right)e^{-\frac{\omega^2}{2\omega_a^2}}, \tag{B.7}$$

where $\omega_d = {}^{c}\!/_{d}$ and $\omega_a = {}^{c}\!/_{a}$.

B.3 Deformation Potential and Piezoelectric Interaction

Comparing Eq. (B.2) with Eqs. (2.49) and (2.56) to identify the form of $M_{\mathbf{k}}$ which was neglected in deriving the angular form factor of the spectral density, we find

$$M_{\mathbf{k}} = D\left(\frac{\hbar}{2\mu v \omega_{\mathbf{k}}}\right)^{-\frac{1}{2}}|\mathbf{k}| \tag{B.8}$$

for deformation potential coupling, and

$$M_{\mathbf{k}} = iP\left(\frac{\hbar}{2\mu v \omega_{\mathbf{k}}}\right)^{-\frac{1}{2}} \tag{B.9}$$

for piezoelectric coupling. As these expressions are either constant or depend on the magnitude of the wavevector, they can be trivially evaluated in the 3D integral over $\mathbf{k}$ due to the presence of $\delta(\omega - ck)$. The complete expressions for the deformation potential and piezoelectric spectral densities are then

$$J_{3D}^{D}(\omega) = \frac{D^2\hbar}{2\pi^2\mu c^2 d^3}\left(\frac{\omega}{\omega_d}\right)^3\left(1-\operatorname{sinc}\frac{\omega}{\omega_d}\right)e^{-\frac{\omega^2}{2\omega_a^2}}, \tag{B.10a}$$

$$J_{3D}^{P}(\omega) = \frac{P^2\hbar}{2\pi^2\mu c^2 d}\frac{\omega}{\omega_d}\left(1-\operatorname{sinc}\frac{\omega}{\omega_d}\right)e^{-\frac{\omega^2}{2\omega_a^2}}. \tag{B.10b}$$

C

Reparameterisation of a 2D Disorder Potential

This appendix relates to the reparameterisation of a 2D disorder potential discussed in Chapter 5. We outline the mathematical details of the reparameterisation and discuss the optimisation and inference of parameters required to generate posterior disorders.

C.1 Inducing Points and Random Fourier Features

Let $X = \{\mathbf{r}_k^X | k = 1, \ldots, n_X\}$ denote the set of dense grid points (34×52 or 45×69 for the experiments in the paper, depending on the CNN model) on the x-y plane, the potential of which is the input of the CNN. Without any measurement, the disorder potential values on X, denoted by ϕ^X, is approximately a random vector following the normal distribution:

$$\phi^X \sim \mathcal{N}(m\mathbf{1}, K_X), \tag{C.1}$$

where m is the pre-calculated mean potential level, $\mathbf{1}$ is a one-filled vector, and K_X is the covariance matrix, of which element (i, j) is $k(\mathbf{r}_i^X, \mathbf{r}_j^X)$. For the results presented in Chapter 5, the value of $m = 1184$mV is determined from the mean values of

1000 random disorder potentials generated using the electrostatic model (with ϕ_s absorbed into the disorder potential, $m = 384$mV). For the sake of simplicity, the all derivations below are based on the mean-adjusted potential: $\mathbf{f} = \phi^X - m\mathbf{1}$. In order to generate a random sample from $\mathbf{f}$, we can draw a random sample from $\epsilon_X \sim \mathcal{N}(\mathbf{0}, I_X)$ and then transform it as

$$\mathbf{f} = L_X \epsilon_X, \tag{C.2}$$

where $\mathbf{0}$ is a zero-filled vector, I_X is the $n_X \times n_X$ identity matrix, and L_X is the lower Cholesky decomposition of K_X.

Since n_X is too large for a practical Bayesian inference problem, and we want to make the inference algorithm independent of n_X, the inducing point approach is used. The set of inducing points, $Z = \{\mathbf{r}_k^Z | k = 1, \ldots, n_Z\}$, usually has many fewer points than X: $n_Z < n_X$. Let $\mathbf{u}$ denote the vector of the mean-adjusted potential values at Z (i.e. $\mathbf{u} = \boldsymbol{\alpha} - m\mathbf{1}$ using notation from Chapter 5). The two mean-adjusted potential vectors $\mathbf{f}$ and $\mathbf{u}$ are jointly a normal distribution, and the joint distribution can be decomposed into two terms: $p(\mathbf{u}, \mathbf{f}) = p(\mathbf{u})p(\mathbf{f}|\mathbf{u})$. The first term is a prior distribution, $p(\mathbf{u}) = \mathcal{N}(\mathbf{u}; \mathbf{0}, K_Z)$, where K_Z is the covariance matrix, of which element (i, j) is $k(\mathbf{r}_i^Z, \mathbf{r}_j^Z)$. The second term is the conditional distribution of $\mathbf{f}$ given $\mathbf{u}$:

$$p(\mathbf{f}|\mathbf{u}) = \mathcal{N}(\mathbf{f}|K_{XZ}K_Z^{-1}\mathbf{u}, K_X - K_{XZ}K_Z^{-1}K_{ZX}). \tag{C.3}$$

The computational complexity of computing the covariance of $\mathbf{f}|\mathbf{u}$ is $O(n_X^3)$ because of the covariance matrix in Eq. (C.3). To reduce the computational complexity, any low-rank approximation can be used. In this paper, we approximate the covariance matrix with spectral features, where the idea is to let inducing points account for spatially important locations, and the spectral features control relatively unimportant spatial information. The approximation of various covariance kernel functions with spectral features is extensively studied in the context of random Fourier features [142–147].

The spectral feature is

$$\psi(\mathbf{r}) = \frac{1}{\sqrt{q}}[\cos(\omega_1^\top \mathbf{r}), \sin(\omega_1^\top \mathbf{r}), \ldots, \cos(\omega_q^\top \mathbf{r}), \sin(\omega_q^\top \mathbf{r})], \tag{C.4}$$

where q is an arbitrary chosen integer satisfying $n_Z < 2q < n_X$, and w_i is a random sample whose probability density function depends on the underlying covariance kernel function. We use $q = 300$ in this work. The $n_z < 2q$ inequality ensures $\Psi_Z \Psi_Z^\top$ (defined below) is invertible, and $2q < n_x$ ensures that an advantage is gained in computational complexity when using random Fourier features.

C.2 Disorder Covariance

A Gaussian Process, requiring a covariance function of the random disorder potential, is used to generate random disorder potentials in the inference algorithm. The donor plane divided into cells, with a random variable $I_{ij} \in \mathbb{N}_0$ determining the number of donors in the cell at $\mathbf{r}_{ij} = (x_i, y_j)$. The potential the 2DEG from the donor ion distribution is given by $\phi_\mathrm{d}(\mathbf{r}) = \sum_{ij} I_{ij} \phi_\mathrm{d}(\mathbf{r}, \mathbf{r}_{ij})$, summing over each cell in the donor plane.

The covariance between two points in the 2DEG plane can be evaluated numerically, and appropriate kernel parameters are fitted. The covariance of ϕ_d between two points in the 2DEG plane can be computed numerically as $\mathrm{cov}\Big(\mathbf{r}, \mathbf{r}'\Big) = \mathrm{var}(I) \sum_{ij} \phi_\mathrm{d}(\mathbf{r}, \mathbf{r}_{ij}) \phi_\mathrm{d}(\mathbf{r}', \mathbf{r}_{ij})$, where I is the distribution from which each I_{ij} is independently drawn. Using the correlation function eliminates the dependence on I,

$$\mathrm{corr}\Big(\mathbf{r}, \mathbf{r}'\Big) = \frac{\sum_{ij} \phi_\mathrm{d}(\mathbf{r}, \mathbf{r}_{ij}) \phi_\mathrm{d}(\mathbf{r}', \mathbf{r}_{ij})}{\sqrt{\sum_{ij} \phi_\mathrm{d}(\mathbf{r}, \mathbf{r}_{ij})^2} \sqrt{\sum_{ij} \phi_\mathrm{d}(\mathbf{r}', \mathbf{r}_{ij})^2}}. \tag{C.5}$$

A rational quadratic kernel function

$$k(\mathbf{r}, \mathbf{r}') = \sigma \left(1 + \frac{|\mathbf{r} - \mathbf{r}'|^2}{\rho^2}\right)^{-1} \tag{C.6}$$

is chosen, with fitted values of $\rho = 139.8\mathrm{nm}$ and $\sigma = 20.8\mathrm{mV}$. Alternative kernels provide better fits, but the explicit form of the corresponding frequency distribution of random Fourier features is unknown or intractable.

The corresponding probability distribution of the frequency samples $\omega_1, \ldots, \omega_q$ given the kernel function Eq. (C.6) is

$$p(\omega) = \rho e^{-\rho\|\omega\|_1}, \tag{C.7}$$

where ω is an angular frequency, and $\|\cdot\|_1$ is the L1 norm function.

C.3 Approximating the Posterior Distribution

The prior covariance matrices, K_X and K_Z, are approximated by the spectral features: $K_X \approx \Psi_X \Psi_X^\top$ and $K_Z \approx \Psi_Z \Psi_Z^\top$, where $\Psi_X \in \mathbb{R}^{n_X \times 2q}$ with $\psi(\mathbf{r})^\top$ for $\mathbf{r} \in X$ as rows, and Ψ_Z is defined in a similar fashion. The posterior covariance in Eq. (C.3) is approximated as $\mathrm{cov}(\mathbf{f}|\mathbf{u}) \approx \bar{\Psi}_X \bar{\Psi}_X^\top$, where $\bar{\Psi}_X = \Psi_X - \Psi_X \Psi_Z^\top (\Psi_Z \Psi_Z^\top)^{-1} \Psi_Z$. The approximated random field by substituting the approximated covariance matrix into Eq. (C.3) is

$$\mathbf{f} \approx K_{XZ} {L_Z^{-1}}^\top \boldsymbol{\epsilon}_Z + \bar{\Psi}_X \boldsymbol{\epsilon}_{2q}, \tag{C.8}$$

where $\boldsymbol{\epsilon}_Z$ and $\boldsymbol{\epsilon}_{2q}$ are standard normal random vectors with length n_Z and $2q$, respectively, and L_Z is the lower Cholesky decomposition of K_Z. The approximated posterior random vector is straightforward,

$$\mathbf{f}|\mathbf{u} \approx K_{XZ} {L_Z^{-1}}^\top \mathbf{u} + \bar{\Psi}_X \boldsymbol{\epsilon}_{2q}. \tag{C.9}$$

The equation defines the reconstruction of ϕ^X through the function

$$\phi^X \approx f(Z, \mathbf{u}, \boldsymbol{\epsilon}_{2q}) = K_{XZ} {L_Z^{-1}}^\top \mathbf{u} + \bar{\Psi}_X \boldsymbol{\epsilon}_{2q} + m\mathbf{1}, \tag{C.10}$$

using the mean adjusted values, and

$$\hat{\phi} = f(Z, \boldsymbol{\alpha}, \boldsymbol{\beta}) = K_{XZ} {L_Z^{-1}}^\top (\boldsymbol{\alpha} - m\mathbf{1}) + \bar{\Psi}_X \boldsymbol{\beta} + m\mathbf{1}. \tag{C.11}$$

using the notation in Eq. (5.2) where $\boldsymbol{\alpha} = \mathbf{u} + m\mathbf{1}$, and $\boldsymbol{\beta} = \boldsymbol{\epsilon}_{2q}$.

C.4 Optimisation of Inducing Point Locations

The inducing point locations, Z, must only be optimised once for a given gate electrode architecture. The optimisation routine considers only simulated data, with the inputs being: a set of disorder potentials randomly generated using the electrostatic model, Φ^X_{sim}, a set of randomly generated gate voltages near the closed channel boundary, $\mathcal{V}_{\text{sim}}$, and initial inducing point locations, Z_{init}. In order to perform the optimisation, we also require a Gaussian process kernel function for disorder as presented in Eq. (C.6), the CNN $\mathcal{F}_U$ discussed in Chapter 4, and an optimiser for which we choose Adam [160].

The idea is to compare the location of the closed channel boundary for the simulated disorder potentials, Φ^X_{sim}, and a set of disorder potentials approximated using the Gaussian process reparameterisation discussed above, Φ^X_{GP}. The values on the inducing points $\boldsymbol{\alpha}$ are set to the true values at those locations for each element of Φ^X_{sim}, which means that the optimal inducing point locations, Z_{opt}, will generate Φ^X_{GP} which best match the current predictions of Φ^X_{sim}. We consider the difference in current probability predictions made using Φ^X_{sim} and Φ^X_{GP} for gate voltages in $\mathcal{V}_{\text{sim}}$, which are randomly distributed on either side of the boundary. The probability of current p for a given disorder potential ϕ_d and gate voltages $\mathbf{v}$ uses the evaluation of $\phi_{\text{tot}}(\mathbf{r}_*)$ from F_U (with $U^* = -\phi_{\text{tot}}(\mathbf{r}_*)$) to give,

$$p = \sigma_\xi(\mathcal{F}_U(g(\phi_{\text{d}}, \mathbf{v})); 10) \tag{C.12}$$

where $g(\phi_{\text{d}}, \mathbf{v})$ computes ϕ_{in} on the dense grid for CNN (see Section 4.4.1), and σ_ξ is a modified sigmoid function with margin ξ and steepness parameter η, $\sigma_\xi(\cdot;\eta) = \xi + (1-2\xi)\sigma(\cdot;\eta)$. Choosing a steepness parameter of $\eta = 10$ means that the boundary is relatively sharp, while also remaining differentiable as required for use with the Adam optimiser. Choosing a margin $\xi = 0.01$ allows for discrepancy between the approximated model and the real data.

We quantify the difference by considering the KL divergence between the set of current probability predictions $\mathbf{p}$ and $\mathbf{p}^{\text{GP}}$ made using Φ^X_{sim} and Φ^X_{GP} respectively.

The KL divergence is evaluated as

$$\mathrm{KL}(\mathbf{p}, \mathbf{p}^{\mathrm{GP}}) = \sum_i \Big[p_i \log(p_i/p_i^{\mathrm{GP}}) + (1-p_i)\log((1-p_i)/(1-p_i^{\mathrm{GP}})) \Big], \tag{C.13}$$

and is used to generate a loss function which is symmetric with respect to the order of the probability distributions,

$$L = \mathrm{KL}(\mathbf{p}, \mathbf{p}^{\mathrm{GP}}) + \mathrm{KL}(\mathbf{p}^{\mathrm{GP}}, \mathbf{p}). \tag{C.14}$$

In our optimisation routine, we follow standard principles of stochastic optimisation, and split the data sets of Φ^X_{sim} and $\mathcal{V}_{\mathrm{sim}}$ into mini-batches where a set $n_v = 20$ voltage values are considered for each of $n_d = 20$ disorder potentials. We perform 3×10^4 iterations of the optimisation routine to arrive at the optimised inducing point locations Z_{opt} displayed in Figure 5.2.

C.5 MCMC Inference

The goal of the MCMC inference is to generate random samples from the posterior distribution of uncertain variables. The uncertain variables in (C.9) are $\mathbf{u}$ and $\boldsymbol{\epsilon}_{2q}$. the posterior probability of $(\mathbf{u}, \boldsymbol{\epsilon}_{2q})$ given observed current measurements in D is

$$p(\mathbf{u}, \boldsymbol{\epsilon}_{2q}|D) \propto p(\mathbf{u})p(\boldsymbol{\epsilon}_{2q}) \prod_{i=1}^{2n_u} \left(p_i^{\mathrm{GP}}\right)^{y_i} \left(1 - p_i^{\mathrm{GP}}\right)^{1-y_i}, \tag{C.15}$$

where $p_i^{\mathrm{GP}} = \mathcal{F}_U^{\mathrm{prob}}(f(X, \mathbf{u}, \boldsymbol{\epsilon}_{2q}), \mathbf{v}_i)$. The prior distributions $p(\mathbf{u})$ and $p(\boldsymbol{\epsilon}_{2q})$ are defined earlier in this Appendix. A Binomial likelihood function is used for the i^{th} measurement where $\mathcal{F}_U^{\mathrm{prob}}(f(X, \mathbf{u}, \boldsymbol{\epsilon}_{2q}), \mathbf{v}_i)$ is the probability of current flowing at voltages $\mathbf{v}_i$. Evaluating the likelihood function with sufficient speed to maintain practical inference times is facilitated by using CNN computation of $\mathcal{F}_U(\cdot)$ on GPU hardware. Each time MCMC inference is performed a different number of posterior samples are generated. In the results presented in Chapter 5 we use Hamiltonian Monte Carlo (HMC) sampling and find typical posterior sample sizes to be $150 < n_{\mathrm{s}} < 320$.

D

Double Quantum Dot Labels

In Figure D.1 we show examples of the 2D current scans used for human expert labellers to determine the presence of double quantum dots as discussed in Chapter 5. When scanning an accepted voltage vector in the experiment, 2D current scans are taken at 13.3mV intervals in R once the current drops to 80% of the open channel value. The protocol stops taking scans once the maximum current value in a 2D scan is less than 100pA. The set of 2D scans corresponding to each vector is labelled by 6 human experts to determine whether a double dot exists along that vector. If more than 3 out of the 6 human experts label a double dot in a set of scans, then a double dot is deemed to exist in transport measurements along the given vector. In the event of a split decision (i.e. 3 out of 6 double dot labels), we do not consider a double dot to exist.

There is variation among human expert double quantum dot classification, necessitating a decision based on multiple labels. In the comparison of random and posterior disorders, this variation is not a significant concern. The human experts were not informed of which type of disorder selected the measurement, so a labeller is equally discriminant across both random and posterior disorders. The harshest labeller identified double quantum dots with approximately a third of the frequency of the most generous labeller. Using 6 human experts results in a more balanced outcome, with results reported in Chapter 5.

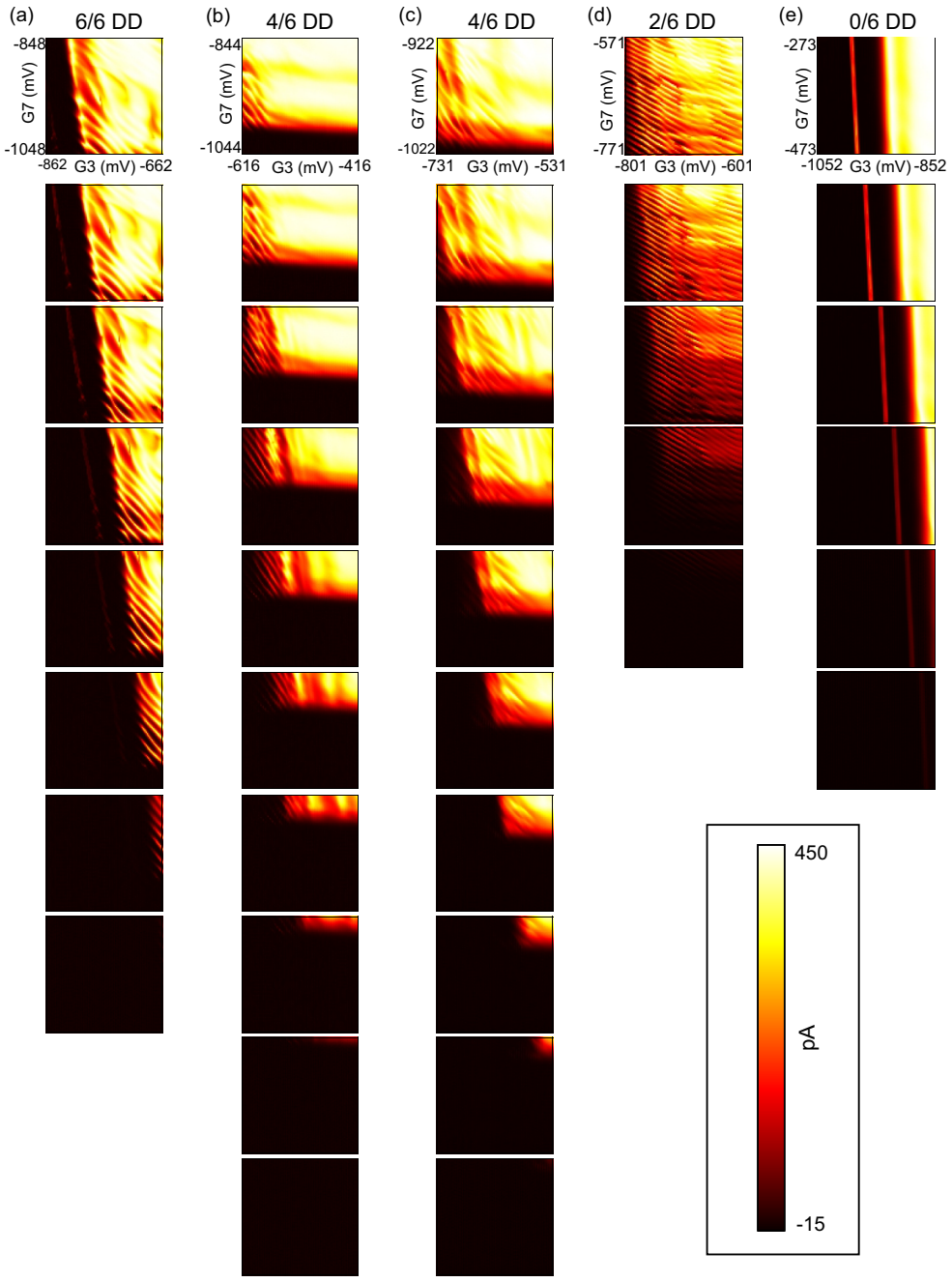

Figure D.1: Each column (a)-(e) is a set of 2D current scans taken using a vector accepted by the filtering process discussed in Chapter D.1. Each scan is a 200 mV × 200 mV window over gates G3 and G7, with the original 7-dimensional voltage vector at the centre. The magnitude of R (as defined in Chapter D.1) is increased by 13.3 mV from one row to the next. The axes of the first scan in each column are labelled to indicate the range of voltage values considered. The colour scale shared by all plots is shown in the box. The result of human expert labels is indicated at the top of each column. For example, '4/6 DD' indicates that 4 out of 6 labellers considered a double dot to exist in the set of current scans. The vectors (a)-(d) were only accepted using posterior disorders and (e) was only accepted using random disorders. Some vectors were accepted by both random and posterior disorders, but not the examples shown.

E

Numerical Solution of Quantum Master Equations

This appendix considers the numerical solution of the quantum master equations discussed in Chapter 2 and explored in the differentiable quantum master equation solver developed in Chapter 6.

E.1 Steady State Solution

The general form of a quantum master equation describing the evolution of a density matrix ρ in a Hilbert space of dimension d is,

$$\frac{d\rho}{dt} = \mathcal{L}\rho, \tag{E.1}$$

where $\mathcal{L}$ is the Liouvillian superoperator containing details of the evolution. To cast this equation into a numerically tractable problem, we transform the $d \times d$ density matrix ρ into a complex valued vector $\vec{\rho}$ of length d^2, which we call superspace. In this notation, the Liouvillian superoperator becomes a $d^2 \times d^2$ matrix L and the master equation in Eq. (E.1) becomes a system of coupled linear differential equations. The density matrix is cast as a vector such that

$$\vec{\rho} = \mathrm{col}(\rho_{11}, \rho_{21}, \ldots, \rho_{d1}, \rho_{12}, \rho_{22}, \rho_{32}, \ldots, \rho_{dd}). \tag{E.2}$$

The general solution of Eq. (E.1) describing time evolution of the density matrix in superspace is then

$$\vec{\rho}(t) = e^{\mathbf{L}t}\vec{\rho}(0), \tag{E.3}$$

which for small systems can be computed directly. The steady state density matrix $\vec{\rho}_{ss}$ is the solution to Eq. (E.1) in the long-time limit. This solution is the zero eigenvalue of $\mathbf{L}$ and can be recast into a system of linear equation by setting $\mathbf{L}\vec{\rho}_{ss} = 0$. To impose the constraint that the solution has unit trace (as required for a density matrix), we have

$$(\mathbf{L} + w\mathbf{T})\vec{\rho} = \begin{pmatrix} w \\ 0 \\ 0 \\ \vdots \end{pmatrix}, \tag{E.4}$$

where w is a weighting factor, and the matrix $\mathbf{T}$ gives the trace of the density matrix in superspace. Further details on numerical approaches to the steady state solution of quantum master equations can be found in Ref. [169].

E.2 Lindblad Master Equation Liouvillian

The solutions discussed in the previous section hold for a generic form of the Liouvillian $\mathcal{L}$ and thus $\mathbf{L}$. The difficulty often lies in finding the details of the Liouvillian, and here we consider the Lindblad master equations as relevant to this thesis. The Liouvillian of a Lindblad master equation is expressed in Hilbert space as

$$\frac{d\rho}{dt} = -i[H, \rho] + \sum_k \Gamma_k \Big(A_k \rho A_k^\dagger - \frac{1}{2}(A_k^\dagger A_k \rho + \rho A_k^\dagger A_k) \Big), \tag{E.5}$$

where H is the Hamiltonian, A_k is the k^{th} Lindblad operator acting with dissipation rate Γ_k. To cast this construction into superspace we must transform the operators appropriately. Consider an operator O represented as $O = \sum_{nm=1}^{d} O_{nm}|n\rangle\langle m|$, where $\{|n\rangle\}_{n=1}^{d}$ are basis states spanning a fictitious Hilbert space. In superspace we define a basis $\{|\alpha\rangle\}_{n=1}^{d^2}$ such that $|\alpha = n + (m-1)d\rangle = |n\rangle \otimes |m\rangle$, and express the operator O as a vector,

$$\vec{O} = \sum_{\alpha=1}^{d^2} O_\alpha |\alpha\rangle. \tag{E.6}$$

This representation is equivalent to the definition of $\vec{\rho}$ given in Eq. (E.2). We now consider the action of additional operators A and B acting on O. The superoperator $\mathcal{S}O = AOB = \sum_{klnm=1}^{d} O_{nm}A_{kn}B_{mn}|k\rangle\langle l|$ acting on O in Hilbert space, acts on $\vec{O}$ in superspace as

$$\mathbf{S}\vec{O} = \sum_{klmn=1}^{d} O_{nm}A_{kn}B_{mn}|k\rangle \otimes |l\rangle. \tag{E.7}$$

We can rearrange this expression using the definition of A and B as operators acting in Hilbert space (e.g. $A|n\rangle = \sum_{i=1}^{d} A_{in}|i\rangle$). We then have

$$\mathbf{S}\vec{O} = \sum_{nm=1}^{d} O_{nm}(A|n\rangle \otimes B^T|m\rangle) = (A \otimes B^T)\vec{O} \tag{E.8}$$

which shows that in superspace, the action of an operator to the left corresponds to the action of the operator on the first fictitious Hilbert space, and operators on the right correspond to the action of the transpose of that operator on the second fictitious Hilbert space. We can then arrive at a representation of the master equation Eq. (E.5) in superspace

$$\frac{d\vec{\rho}}{dt} = \Big[-i\Big(H\otimes I - I\otimes H\Big) + \sum_k \Gamma_k\Big(A_k\otimes(A_k^\dagger)^T - \frac{1}{2}A_k^\dagger A_k\otimes I - \frac{1}{2}I\otimes(A_k^\dagger A_k)^T\Big)\Big]\vec{\rho}, \tag{E.9}$$

where I is the identity operator.

References

[1] John Bardeen and Walter Hauser Brattain. "The transistor, a semi-conductor triode". In: *Physical Review* 74.2 (1948), p. 230.

[2] Jack S Kilby. "Invention of the integrated circuit". In: *IEEE Transactions on Electron Devices* 23.7 (1976), pp. 648–654.

[3] John Shalf. "The future of computing beyond Moore's Law". In: *Philosophical Transactions of the Royal Society A* 378.2166 (2020), p. 20190061.

[4] Daniel Loss and David P DiVincenzo. "Quantum computation with quantum dots". In: *Physical Review A* 57.1 (1998), p. 120.

[5] Stephan GJ Philips et al. "Universal control of a six-qubit quantum processor in silicon". In: *Nature* 609.7929 (2022), pp. 919–924.

[6] Akito Noiri et al. "Fast universal quantum gate above the fault-tolerance threshold in silicon". In: *Nature* 601.7893 (2022), pp. 338–342.

[7] G Granger et al. "Quantum interference and phonon-mediated back-action in lateral quantum-dot circuits". In: *Nature Physics* 8.7 (2012), pp. 522–527.

[8] TR Hartke et al. "Microwave detection of electron-phonon interactions in a cavity-coupled double quantum dot". In: *Physical Review Letters* 120.9 (2018), p. 097701.

[9] Martin Josefsson et al. "A quantum-dot heat engine operating close to the thermodynamic efficiency limits". In: *Nature Nanotechnology* 13.10 (2018), pp. 920–924.

[10] S Sasaki et al. "Kondo effect in an integer-spin quantum dot". In: *Nature* 405.6788 (2000), pp. 764–767.

[11] B Babić, T Kontos, and C Schönenberger. "Kondo effect in carbon nanotubes at half filling". In: *Physical Review B* 70.23 (2004), p. 235419.

[12] Annika Kurzmann et al. "Kondo effect and spin–orbit coupling in graphene quantum dots". In: *Nature Communications* 12.1 (2021), p. 6004.

[13] Tobias Böhler, Achim Edtbauer, and Elke Scheer. "Conductance of individual C 60 molecules measured with controllable gold electrodes". In: *Physical Review B* 76.12 (2007), p. 125432.

[14] Pascal Gehring et al. "Distinguishing lead and molecule states in graphene-based single-electron transistors". In: *ACS nano* 11.6 (2017), pp. 5325–5331.

[15] Richard J Warburton. "Single spins in self-assembled quantum dots". In: *Nature Materials* 12.6 (2013), pp. 483–493.

[16] Gregory D Scholes et al. "Using coherence to enhance function in chemical and biophysical systems". In: *Nature* 543.7647 (2017), pp. 647–656.

[17] Christine Maier et al. “Environment-assisted quantum transport in a 10-qubit network”. In: *Physical Review Letters* 122.5 (2019), p. 050501.

[18] Anton Potočnik et al. “Studying light-harvesting models with superconducting circuits”. In: *Nature Communications* 9.1 (2018), p. 904.

[19] Leo P Kouwenhoven et al. “Electron transport in quantum dots”. In: *Mesoscopic Electron Transport* (1997), pp. 105–214.

[20] Wilfred G Van der Wiel et al. “Electron transport through double quantum dots”. In: *Reviews of Modern Physics* 75.1 (2002), p. 1.

[21] Jason R Petta et al. “Coherent manipulation of coupled electron spins in semiconductor quantum dots”. In: *Science* 309.5744 (2005), pp. 2180–2184.

[22] Menno Veldhorst et al. “A two-qubit logic gate in silicon”. In: *Nature* 526.7573 (2015), pp. 410–414.

[23] M Ciorga et al. “Addition spectrum of a lateral dot from Coulomb and spin-blockade spectroscopy”. In: *Physical Review B* 61.24 (2000), R16315.

[24] R. Hanson et al. “Spins in few-electron quantum dots”. In: *Rev. Mod. Phys.* 79 (4 2007), pp. 1217–1265.

[25] Franck HL Koppens et al. “Control and detection of singlet-triplet mixing in a random nuclear field”. In: *Science* 309.5739 (2005), pp. 1346–1350.

[26] JM Elzerman et al. “Single-shot read-out of an individual electron spin in a quantum dot”. In: *Nature* 430.6998 (2004), pp. 431–435.

[27] Alexander Comstock Johnson et al. “Singlet-triplet spin blockade and charge sensing in a few-electron double quantum dot”. In: *Physical Review B* 72.16 (2005), p. 165308.

[28] JR Petta et al. “Pulsed-gate measurements of the singlet-triplet relaxation time in a two-electron double quantum dot”. In: *Physical Review B* 72.16 (2005), p. 161301.

[29] Alexei M Tyryshkin et al. “Electron spin coherence exceeding seconds in high-purity silicon”. In: *Nature Materials* 11.2 (2012), pp. 143–147.

[30] Fabio Ansaloni et al. “Single-electron operations in a foundry-fabricated array of quantum dots”. In: *Nature Communications* 11.1 (2020), p. 6399.

[31] Will Gilbert et al. “Single-electron operation of a silicon-CMOS 2× 2 quantum dot array with integrated charge sensing”. In: *Nano Letters* 20.11 (2020), pp. 7882–7888.

[32] Brett M Maune et al. “Coherent singlet-triplet oscillations in a silicon-based double quantum dot”. In: *Nature* 481.7381 (2012), pp. 344–347.

[33] R Maurand et al. “A CMOS silicon spin qubit”. In: *Nature Communications* 7.1 (2016), p. 13575.

[34] Ryan M Jock et al. “A silicon metal-oxide-semiconductor electron spin-orbit qubit”. In: *Nature Communications* 9.1 (2018), p. 1768.

[35] Jarryd J Pla et al. “A single-atom electron spin qubit in silicon”. In: *Nature* 489.7417 (2012), pp. 541–545.

[36] Jarryd J Pla et al. “High-fidelity readout and control of a nuclear spin qubit in silicon”. In: *Nature* 496.7445 (2013), pp. 334–338.

[37] Florian NM Froning et al. “Ultrafast hole spin qubit with gate-tunable spin–orbit switch functionality”. In: *Nature Nanotechnology* 16.3 (2021), pp. 308–312.

[38] Daniel Jirovec et al. “A singlet-triplet hole spin qubit in planar Ge”. In: *Nature Materials* 20.8 (2021), pp. 1106–1112.

[39] Nico W Hendrickx et al. “A four-qubit germanium quantum processor”. In: *Nature* 591.7851 (2021), pp. 580–585.

[40] Wei Lu et al. “One-dimensional hole gas in germanium/silicon nanowire heterostructures”. In: *Proceedings of the National Academy of Sciences* 102.29 (2005), pp. 10046–10051.

[41] Yongjie Hu et al. “Hole spin relaxation in Ge–Si core–shell nanowire qubits”. In: *Nature Nanotechnology* 7.1 (2012), pp. 47–50.

[42] JH Ungerer et al. “Charge-sensing of a Ge/Si core/shell nanowire double quantum dot using a high-impedance superconducting resonator”. In: *Materials for Quantum Technology* 3.3 (2023), p. 031001.

[43] Hannes Watzinger et al. “Heavy-hole states in germanium hut wires”. In: *Nano Letters* 16.11 (2016), pp. 6879–6885.

[44] Hannes Watzinger et al. “A germanium hole spin qubit”. In: *Nature Communications* 9.1 (2018), p. 3902.

[45] Carina Fasth et al. “Tunable double quantum dots in InAs nanowires defined by local gate electrodes”. In: *Nano Letters* 5.7 (2005), pp. 1487–1490.

[46] MJ Biercuk et al. “Gate-defined quantum dots on carbon nanotubes”. In: *Nano Letters* 5.7 (2005), pp. 1267–1271.

[47] MR Gräber et al. “Molecular states in carbon nanotube double quantum dots”. In: *Physical Review B* 74.7 (2006), p. 075427.

[48] Edward A Laird et al. “Quantum transport in carbon nanotubes”. In: *Reviews of Modern Physics* 87.3 (2015), p. 703.

[49] Augustinus (Stijn) M Goossens et al. “Gate-defined confinement in bilayer graphene-hexagonal boron nitride hybrid devices”. In: *Nano Letters* 12.9 (2012), pp. 4656–4660.

[50] Monica T Allen, Jens Martin, and Amir Yacoby. “Gate-defined quantum confinement in suspended bilayer graphene”. In: *Nature Communications* 3.1 (2012), p. 934.

[51] Marius Eich et al. “Coupled quantum dots in bilayer graphene”. In: *Nano Letters* 18.8 (2018), pp. 5042–5048.

[52] Carlo WJ Beenakker. “Theory of Coulomb-blockade oscillations in the conductance of a quantum dot”. In: *Physical Review B* 44.4 (1991), p. 1646.

[53] Theodore A Fulton and Gerald J Dolan. “Observation of single-electron charging effects in small tunnel junctions”. In: *Physical Review Letters* 59.1 (1987), p. 109.

[54] Bart Jan van Wees et al. “Quantum ballistic and adiabatic electron transport studied with quantum point contacts”. In: *Physical Review B* 43.15 (1991), p. 12431.

[55] Joseph Hickie et al. “Automated long-range compensation of an rf quantum dot sensor”. In: *arXiv preprint arXiv:2310.02135* (2023).

[56] M Field et al. “Measurements of Coulomb blockade with a noninvasive voltage probe”. In: *Physical Review Letters* 70.9 (1993), p. 1311.

[57] Florian Vigneau et al. “Probing quantum devices with radio-frequency reflectometry”. In: *Applied Physics Reviews* 10.2 (2023).

[58] Barnaby van Straaten et al. “All rf-based tuning algorithm for quantum devices using machine learning”. In: *arXiv preprint arXiv:2211.04504* (2022).

[59] Renato Durrer et al. “Automated tuning of double quantum dots into specific charge states using neural networks”. In: *Physical Review Applied* 13.5 (2020), p. 054019.

[60] Jana Darulová et al. “Autonomous tuning and charge-state detection of gate-defined quantum dots”. In: *Physical Review Applied* 13.5 (2020), p. 054005.

[61] Hyungil Moon et al. “Machine learning enables completely automatic tuning of a quantum device faster than human experts”. In: *Nature Communications* 11.1 (2020), pp. 1–10.

[62] Brandon Severin et al. “Cross-architecture tuning of silicon and SiGe-based quantum devices using machine learning”. In: *arXiv preprint arXiv:2107.12975* (2021).

[63] Nina M van Esbroeck et al. “Quantum device fine-tuning using unsupervised embedding learning”. In: *New Journal of Physics* 22.9 (2020), p. 095003.

[64] Joshua Ziegler et al. “Toward robust autotuning of noisy quantum dot devices”. In: *Physical Review Applied* 17.2 (2022), p. 024069.

[65] Joshua Ziegler et al. “Tuning arrays with rays: Physics-informed tuning of quantum dot charge states”. In: *Physical Review Applied* 20.3 (2023), p. 034067.

[66] KC Nowack et al. “Single-shot correlations and two-qubit gate of solid-state spins”. In: *Science* 333.6047 (2011), pp. 1269–1272.

[67] Toivo Hensgens et al. “Quantum simulation of a Fermi–Hubbard model using a semiconductor quantum dot array”. In: *Nature* 548.7665 (2017), pp. 70–73.

[68] Christian Volk et al. “Loading a quantum-dot based “Qubyte” register”. In: *npj Quantum Information* 5.1 (2019), p. 29.

[69] AR Mills et al. “Shuttling a single charge across a one-dimensional array of silicon quantum dots”. In: *Nature Communications* 10.1 (2019), p. 1063.

[70] Hans-Christian Ruiz Euler et al. “A deep-learning approach to realizing functionality in nanoelectronic devices”. In: *Nature Nanotechnology* 15.12 (2020), pp. 992–998.

[71] Sandesh S Kalantre et al. “Machine learning techniques for state recognition and auto-tuning in quantum dots”. In: *npj Quantum Information* 5.1 (2019), p. 6.

[72] Justyna P Zwolak et al. “Autotuning of double-dot devices in situ with machine learning”. In: *Physical Review Applied* 13.3 (2020), p. 034075.

[73] Emmanuel Flurin et al. “Using a recurrent neural network to reconstruct quantum dynamics of a superconducting qubit from physical observations”. In: *Physical Review X* 10.1 (2020), p. 011006.

[74] V Nguyen et al. “Deep reinforcement learning for efficient measurement of quantum devices”. In: *npj Quantum Information* 7.1 (2021), p. 100.

[75] Christian Szegedy et al. “Intriguing properties of neural networks”. In: *arXiv preprint arXiv:1312.6199* (2013).

[76] Jiawei Su, Danilo Vasconcellos Vargas, and Kouichi Sakurai. “One pixel attack for fooling deep neural networks”. In: *IEEE Transactions on Evolutionary Computation* 23.5 (2019), pp. 828–841.

[77] Sandy Huang et al. “Adversarial attacks on neural network policies”. In: *arXiv preprint arXiv:1702.02284* (2017).

[78] Stephen Brooks. “Markov chain Monte Carlo method and its application”. In: *Journal of the Royal Statistical Society: Series D (The Statistician)* 47.1 (1998), pp. 69–100.

[79] David M Blei, Alp Kucukelbir, and Jon D McAuliffe. “Variational inference: A review for statisticians”. In: *Journal of the American Statistical Association* 112.518 (2017), pp. 859–877.

[80] Fabrizio Berritta et al. “Real-time two-axis control of a spin qubit”. In: *arXiv preprint arXiv:2308.02012* (2023).

[81] Cristian Bonato et al. “Optimized quantum sensing with a single electron spin using real-time adaptive measurements”. In: *Nature Nanotechnology* 11.3 (2016), pp. 247–252.

[82] Muhammad Junaid Arshad et al. “Online adaptive estimation of decoherence timescales for a single qubit”. In: *arXiv preprint arXiv:2210.06103* (2022).

[83] Inbar Zohar et al. “Real-time frequency estimation of a qubit without single-shot-readout”. In: *Quantum Science and Technology* 8.3 (2023), p. 035017.

[84] TJ Evans et al. “Fast Bayesian tomography of a two-qubit gate set in silicon”. In: *Physical Review Applied* 17.2 (2022), p. 024068.

[85] Bobak Shahriari et al. “Taking the human out of the loop: A review of Bayesian optimization”. In: *Proceedings of the IEEE* 104.1 (2015), pp. 148–175.

[86] Stewart Greenhill et al. “Bayesian optimization for adaptive experimental design: A review”. In: *IEEE Access* 8 (2020), pp. 13937–13948.

[87] Anasua Chatterjee et al. “Semiconductor qubits in practice”. In: *Nature Reviews Physics* 3.3 (2021), pp. 157–177.

[88] Heinz-Peter Breuer and Francesco Petruccione. *The theory of open quantum systems*. Oxford University Press, USA, 2002.

[89] Dara PS McCutcheon et al. “A general approach to quantum dynamics using a variational master equation: Application to phonon-damped Rabi rotations in quantum dots”. In: *Physical Review B* 84.8 (2011), p. 081305.

[90] Aidan Strathearn et al. “Efficient non-Markovian quantum dynamics using time-evolving matrix product operators”. In: *Nature Communications* 9.1 (2018), p. 3322.

[91] Moritz Cygorek et al. “Simulation of open quantum systems by automated compression of arbitrary environments”. In: *Nature Physics* 18.6 (2022), pp. 662–668.

[92] Howard Carmichael. *Statistical methods in quantum optics 1: master equations and Fokker-Planck equations*. Vol. 1. Springer Science & Business Media, 1999.

[93] Fabio Covito et al. "Transient charge and energy flow in the wide-band limit". In: *Journal of Chemical Theory and Computation* 14.5 (2018), pp. 2495–2504.

[94] Ehoud Pazy. "Calculation of pure dephasing for excitons in quantum dots". In: *Semiconductor Science and Technology* 17.11 (2002), p. 1172.

[95] Gerald D Mahan. *Many-particle physics*. Springer Science & Business Media, 2000.

[96] TM Stace, AC Doherty, and SD Barrett. "Population inversion of a driven two-level system in a structureless bath". In: *Physical Review Letters* 95.10 (2005), p. 106801.

[97] Yuli V Nazarov and Yaroslav M Blanter. *Quantum Transport: Introduction to Nanoscience*. Cambridge University Press, 2009.

[98] Christoph W Groth et al. "Kwant: a software package for quantum transport". In: *New Journal of Physics* 16.6 (2014), p. 063065.

[99] Antti-Pekka Jauho, Ned S Wingreen, and Yigal Meir. "Time-dependent transport in interacting and noninteracting resonant-tunneling systems". In: *Physical Review B* 50.8 (1994), p. 5528.

[100] Karsten Flensberg. "Tunneling broadening of vibrational sidebands in molecular transistors". In: *Physical Review B* 68.20 (2003), p. 205323.

[101] Michael Galperin, Abraham Nitzan, and Mark A Ratner. "Inelastic effects in molecular junction transport: scattering and self-consistent calculations for the Seebeck coefficient". In: *Molecular Physics* 106.2-4 (2008), pp. 397–404.

[102] Jakub K Sowa et al. "Beyond Marcus theory and the Landauer-Büttiker approach in molecular junctions: A unified framework". In: *The Journal of Chemical Physics* 149.15 (2018).

[103] Jakub K Sowa et al. "Environment-assisted quantum transport through single-molecule junctions". In: *Physical Chemistry Chemical Physics* 19.43 (2017), pp. 29534–29539.

[104] MJ Gullans, JM Taylor, and Jason R Petta. "Probing electron-phonon interactions in the charge-photon dynamics of cavity-coupled double quantum dots". In: *Physical Review B* 97.3 (2018), p. 035305.

[105] Gloria Platero and Ramón Aguado. "Photon-assisted transport in semiconductor nanostructures". In: *Physics Reports* 395.1-2 (2004), pp. 1–157.

[106] Aquila Mavalankar et al. "Photon-assisted tunneling and charge dephasing in a carbon nanotube double quantum dot". In: *Physical Review B* 93.23 (2016), p. 235428.

[107] S Gustavsson et al. "Counting statistics of single electron transport in a quantum dot". In: *Physical Review Letters* 96.7 (2006), p. 076605.

[108] Andrea Hofmann et al. "Equilibrium free energy measurement of a confined electron driven out of equilibrium". In: *Physical Review B* 93.3 (2016), p. 035425.

[109] Takafumi Fujita et al. "Coherent shuttle of electron-spin states". In: *npj Quantum Information* 3.1 (2017), p. 22.

[110] Akito Noiri et al. “A shuttling-based two-qubit logic gate for linking distant silicon quantum processors”. In: *Nature Communications* 13.1 (2022), p. 5740.

[111] K Wang et al. “Charge relaxation in a single-electron Si/SiGe double quantum dot”. In: *Physical Review Letters* 111.4 (2013), p. 046801.

[112] Andrea Hofmann et al. “Phonon spectral density in a GaAs/AlGaAs double quantum dot”. In: *Physical Review Research* 2.3 (2020), p. 033230.

[113] John A Nixon and John H Davies. “Potential fluctuations in heterostructure devices”. In: *Physical Review B* 41.11 (1990), p. 7929.

[114] John H Davies, Ivan A Larkin, and EV Sukhorukov. “Modeling the patterned two-dimensional electron gas: Electrostatics”. In: *Journal of Applied Physics* 77.9 (1995), pp. 4504–4512.

[115] JH Davies. “Electronic states in narrow semiconducting wires near threshold”. In: *Semiconductor Science and Technology* 3.10 (1988), p. 995.

[116] Daniel Jirovec et al. “Dynamics of hole singlet-triplet qubits with large g-factor differences”. In: *Physical Review Letters* 128.12 (2022), p. 126803.

[117] Edsger W Dijkstra et al. “A note on two problems in connexion with graphs”. In: *Numerische Mathematik* 1.1 (1959), pp. 269–271.

[118] Thomas H Cormen et al. *Introduction to Algorithms*. MIT Press, 2009.

[119] Laith Alzubaidi et al. “Review of deep learning: Concepts, CNN architectures, challenges, applications, future directions”. In: *Journal of Big Data* 8 (2021), pp. 1–74.

[120] Kaiming He et al. “Deep residual learning for image recognition”. In: *Proceedings of the IEEE conference on computer vision and pattern recognition*. 2016, pp. 770–778.

[121] Xingjian Shi et al. “Convolutional LSTM network: A machine learning approach for precipitation nowcasting”. In: *Advances in Neural Information Processing Systems* 28 (2015).

[122] David Marr and Ellen Hildreth. “Theory of edge detection”. In: *Proceedings of the Royal Society of London. Series B. Biological Sciences* 207.1167 (1980), pp. 187–217.

[123] Stuart Lloyd. “Least squares quantization in PCM”. In: *IEEE Transactions on Information Theory* 28.2 (1982), pp. 129–137.

[124] Samuel Neyens et al. “Probing single electrons across 300 mm spin qubit wafers”. In: *arXiv preprint arXiv:2307.04812* (2023).

[125] Benjamin Venitucci et al. “Modeling silicon CMOS devices for quantum computing”. In: *2019 International Conference on Simulation of Semiconductor Processes and Devices (SISPAD)*. IEEE. 2019, pp. 1–4.

[126] M Koivisto and MJ Stott. “Kinetic energy functional for a two-dimensional electron system”. In: *Physical Review B* 76.19 (2007), p. 195103.

[127] Justyna P Zwolak et al. “QFlow lite dataset: A machine-learning approach to the charge states in quantum dot experiments”. In: *PLoS One* 13.10 (2018), e0205844.

[128] J Zamastil. "Multidimensional WKB approximation for particle tunneling". In: *Physical Review A* 72.2 (2005), p. 024101.

[129] Jan Klos et al. "Calculation of tunnel couplings in open gate-defined disordered quantum dot systems". In: *Physical Review B* 98.15 (2018), p. 155320.

[130] Kyle Mills, Michael Spanner, and Isaac Tamblyn. "Deep learning and the Schrödinger equation". In: *Physical Review A* 96.4 (2017), p. 042113.

[131] Matthew G Borselli et al. "Pauli spin blockade in undoped Si/SiGe two-electron double quantum dots". In: *Applied Physics Letters* 99.6 (2011), p. 063109.

[132] M Stopa. "Quantum dot self-consistent electronic structure and the Coulomb blockade". In: *Physical Review B* 54.19 (1996), p. 13767.

[133] John A Nixon, John H Davies, and Harold U Baranger. "Breakdown of quantized conductance in point contacts calculated using realistic potentials". In: *Physical Review B* 43.15 (1991), p. 12638.

[134] Thomas Palm. "Effects of remote impurity scattering including donor correlations in a branching electron waveguide". In: *Physical Review B* 52.15 (1995), p. 11284.

[135] Mikael Sunnåker et al. "Approximate Bayesian Computation". In: *PLOS Computational Biology* 9.1 (2013), pp. 1–10.

[136] Mark A. Beaumont. "Approximate Bayesian Computation". In: *Annual Review of Statistics and Its Application* 6.1 (2019), pp. 379–403.

[137] Stuart Barber, Jochen Voss, and Mark Webster. "The rate of convergence for approximate Bayesian computation". In: *Electronic Journal of Statistics* 9.1 (2015), pp. 80–105.

[138] Marko Järvenpää et al. "Efficient Acquisition Rules for Model-Based Approximate Bayesian Computation". In: *Bayesian Analysis* 14.2 (2019), pp. 595–622.

[139] Michalis Titsias. "Variational Learning of Inducing Variables in Sparse Gaussian Processes". In: ed. by David van Dyk and Max Welling. Vol. 5. PMLR, 2009, pp. 567–574.

[140] Thang D. Bui, Josiah Yan, and Richard E. Turner. "A Unifying Framework for Gaussian Process Pseudo-Point Approximations using Power Expectation Propagation". In: *J. Mach. Learn. Res.* 18 (2017), 104:1–104:72.

[141] Matthias Bauer, Mark van der Wilk, and Carl Edward Rasmussen. "Understanding Probabilistic Sparse Gaussian Process Approximations". In: *Advances in Neural Information Processing Systems*. Ed. by D. Lee et al. Vol. 29. Curran Associates, Inc., 2016.

[142] Zhu Li et al. "Towards a Unified Analysis of Random Fourier Features". In: *Proceedings of the 36th International Conference on Machine Learning*. Ed. by Kamalika Chaudhuri and Ruslan Salakhutdinov. Vol. 97. Proceedings of Machine Learning Research. Long Beach, California, USA: PMLR, 2019, pp. 3905–3914.

[143] Haim Avron et al. "Random Fourier Features for Kernel Ridge Regression: Approximation Bounds and Statistical Guarantees". In: *Proceedings of the 34th International Conference on Machine Learning*. Ed. by Doina Precup and Yee Whye Teh. Vol. 70. Proceedings of Machine Learning Research. PMLR, 2017, pp. 253–262.

[144] James Hensman, Nicolas Durrande, and Arno Solin. "Variational fourier features for Gaussian processes". In: *Journal of Machine Learning Research* 18 (2018), pp. 1–52.

[145] Bharath Sriperumbudur and Zoltan Szabo. "Optimal Rates for Random Fourier Features". In: *Advances in Neural Information Processing Systems 28*. Ed. by C Cortes et al. Curran Associates, Inc., 2015, pp. 1144–1152.

[146] Krzysztof Choromanski et al. "The Geometry of Random Features". In: *Proceedings of the Twenty-First International Conference on Artificial Intelligence and Statistics*. Ed. by Amos Storkey and Fernando Perez-Cruz. Vol. 84. Proceedings of Machine Learning Research. PMLR, 2018, pp. 1–9.

[147] Ali Rahimi Recht and Benjamin. "Random Features for Large-Scale Kernel Machines". In: *Neural Information Processing Systems*. 2007.

[148] Kevin Ryczko, David A Strubbe, and Isaac Tamblyn. "Deep learning and density-functional theory". In: *Physical Review A* 100.2 (2019), p. 022512.

[149] Kyle Mills, Michael Spanner, and Isaac Tamblyn. "Deep learning and the Schrödinger equation". In: *Phys. Rev. A* 96 (4 2017), p. 042113.

[150] Radford M Neal et al. "MCMC using Hamiltonian dynamics". In: *Handbook of Markov chain Monte Carlo* 2.11 (2011), p. 2.

[151] Joshua V Dillon et al. "Tensorflow distributions". In: *arXiv preprint arXiv:1711.10604* (2017).

[152] Federico Fedele et al. "Simultaneous operations in a two-dimensional array of singlet-triplet qubits". In: *PRX Quantum* 2.4 (2021), p. 040306.

[153] Francesco Borsoi et al. "Shared control of a 16 semiconductor quantum dot crossbar array". In: *arXiv preprint arXiv:2209.06609* (2022).

[154] Heorhii Bohuslavskyi et al. "Scalable on-chip multiplexing of low-noise silicon electron and hole quantum dots". In: *arXiv preprint arXiv:2208.12131* (2022).

[155] Frank Schäfer et al. "A differentiable programming method for quantum control". In: *Machine Learning: Science and Technology* 1.3 (2020), p. 035009.

[156] Luuk Coopmans et al. "Protocol discovery for the quantum control of majoranas by differentiable programming and natural evolution strategies". In: *PRX Quantum* 2.2 (2021), p. 020332.

[157] Luuk Coopmans et al. "Optimal control in disordered quantum systems". In: *Physical Review Research* 4.4 (2022), p. 043138.

[158] Ilia Khait, Juan Carrasquilla, and Dvira Segal. "Optimal control of quantum thermal machines using machine learning". In: *Physical Review Research* 4.1 (2022), p. L012029.

[159] Martín Abadi et al. "Tensorflow: Large-scale machine learning on heterogeneous distributed systems". In: *arXiv preprint arXiv:1603.04467* (2016).

[160] Diederik P Kingma and Jimmy Ba. "Adam: A method for stochastic optimization". In: *arXiv preprint arXiv:1412.6980* (2014).

[161] J Robert Johansson, Paul D Nation, and Franco Nori. "QuTiP: An open-source Python framework for the dynamics of open quantum systems". In: *Computer Physics Communications* 183.8 (2012), pp. 1760–1772.

[162] John A Nelder and Roger Mead. "A simplex method for function minimization". In: *The Computer Journal* 7.4 (1965), pp. 308–313.

[163] Toshimasa Fujisawa, Yasuhiro Tokura, and Yoshiro Hirayama. "Energy relaxation process in a quantum dot studied by DC current and pulse-excited current measurements". In: *Physica B: Condensed Matter* 298.1-4 (2001), pp. 573–579.

[164] J Gorman, DG Hasko, and DA Williams. "Charge-qubit operation of an isolated double quantum dot". In: *Physical Review Letters* 95.9 (2005), p. 090502.

[165] KD Petersson et al. "Quantum coherence in a one-electron semiconductor charge qubit". In: *Physical Review Letters* 105.24 (2010), p. 246804.

[166] John Charles Butcher. *Numerical methods for ordinary differential equations*. John Wiley & Sons, 2016.

[167] Alexander Croy and Ulf Saalmann. "Coherent manipulation of charge qubits in double quantum dots". In: *New Journal of Physics* 13.4 (2011), p. 043015.

[168] Anna N Pearson et al. "Measuring the thermodynamic cost of timekeeping". In: *Physical Review X* 11.2 (2021), p. 021029.

[169] PD Nation. "Steady-state solution methods for open quantum optical systems". In: *arXiv preprint arXiv:1504.06768* (2015).